Al/p-CuInSe$_2$ Tunnel MIS Schottky Diodes & Surface Properties of Crystalline p-CuInSe$_2$*

By

© Chi Lun, Chan

McGill University
Department of Electrical Engineering
3480 University Ave.,
Montreal, P.Q., Canada H3A 2A7
March 1989

* This thesis has been submitted to the Faculty of Graduate Studies & Research for partially satisfying the requirements of the M. Eng. (Electrical) degree.

Abstract

The dark current/voltage and capacitance/voltage characteristics of Al/p-$CuInSe_2$ Schottky junctions have been analysed, from which some surface (polished and etched) and bulk (Bridgman-grown) properties of the semiconductor have been determined. At 298°K, the ideality factors n (> 2) are the largest for samples with polished surfaces and for a given dopant concentration. This makes us believe that n(298°K) is mainly governed by interface effects. The temperature-dependent method inferred barrier heights of the order of 0.35 V which was considerably smaller than the theoretical minimum work function difference of 0.408 V between our p-$CuInSe_2$ and Al, suggesting the existence of interfacial insulator ($\Phi_{sm} = V_{do} + V_{io}$ and $\phi_{bo} = V_{do} + \xi$). Adopting Card and Rhoderick's MIS potential distribution theory, surface state density profiles of rising magnitude ($10^{12}cm^{-2}eV^{-1}$) towards the valence band edge were obtained from the log(I)/V plots assuming $\varepsilon_i = \varepsilon_o$ and $\delta = 30$ Å. Larger surface state densities were apparently associated with polished surfaces. The rise in n with a fall in temperature was likely due to the series thermionicfield emission at the Al edges. Minimum electron affinity of p-$CuInSe_2$ and insulator transmission factor were also estimated. The Goodman's model of series R effect on capacitance has been generalized to explain the occurence of unusual minima in our C'^{-2}/V plots at high frequency. The frenquency-dependence of the R-corrected curves is another evidence of interfacial insulator and surface states with occupation controlled by the bulk Fermi-level. The assumption of surface state dominance over deep traps in capacitance contribution was discussed. Using the thick δ limit of Cowley's high frequency MIS capacitance model, surface state densities of the order of $10^{12} cm^{-2} eV^{-1}$ were attained for the etched surfaces from the big discrepancies between the V-intercepts and the I/V diffusion potentials. These values are comparable with those from the n factor analysis. Up-shifts in the C'^{-2}_{min} were observed after air annealing at 230°C. Based on our extended Goodman's model, the rise in R was thought to be caused by the out-diffusion of Se acceptors from the surfaces. Apparent effective acceptor profiles were obtained with the aid of depletion approximation, the validity of which in the presence of interfacial layer, was considered. Bulk uniformity was better along the growth direction than on the transverse plane.

Abstrait

Les charactéristiques de courant/voltage et capacitance/voltage foncées des jonctions Schottky ont été analysées, duquel quelques surfaces (polies et gravées) et propriétés en gros (Bridgman-grown) du semi-conducteur ont été déterminées. A 298°K les facteurs d'idéalité $n(>2)$ sont les plus larges pour les échantillons à surfaces polies et pour une concentration donnée de dopage. Ceci nous fait croire que $n(298^{\circ}K)$ est surtout gouverné par des effets d'interface. La méthode temperature-dépendante a inféré des hauteurs de barrières dans l'ordre de 0.35 V ce qui fût considérablement inférieur à la différence de fonction de travail théorique minimum de 0.408V entre notre p-$CuInSe_2$ et Al, suggérant l'existence de l'isolateur ($\Phi_{sm} = V_{do} + V_{io}$ et $\phi_{bo} = V_{do} + \xi$). Adoptant la théorie de distribution de potentiel MIS de Card et Rhoderick, les profils de densités d'états de surfaces d'ampleur augmentant ($10^{12}cm^{-2}eV^{-1}$) vers le bord de la bande de valence ont été obtenus des courbes de log(I)/V assumant que $\varepsilon_i = \varepsilon_o$ et que $\delta = 30$ Å. De plus grandes densités d'états de surfaces furent apparemment associés avec des surfaces polies. L'augmentation en n accompagnée d'une chute en température fût probablement due à l'émission de champ-thermoionique de série aux bords du Al. Une affinité électron minimum de p-$CuInSe_2$ et le facteur de transmission isolateur ont aussi été évalués. L'effet du modèle série R de Goodman sur la capacitance a été généralisé pour expliquer l'occurence de minima inhabituel dans nos courbes C'^{-2}/V à haute fréquence. La dépendance-fréquence des courbes corrigées-R constitue une autre preuve de présence d'isolateur interfacial et d'états de surfaces avec occupation contrôlée par le gros du niveau-Fermi. On a discuté de la supposition de dominance de l'état de surface sur de profonds pièges dans la contribution à la capacitance. Employant la limite épaisse δ du modèle de capacitance MIS de haute fréquence de Cowley, des densités d'états de surface dans l'ordre de $10^{12}cm^{-2}eV^{-1}$ furent atteintes pour les surfaces gravées provenant de grandes divergences entre les intercepts-V et les potentiels de diffusion I/V. Ces valeurs sont comparables à celles obtenues de l'analyse du facteur n. Des déplacements à des niveaux plus élevés dans le C'^{-2}_{min} ont été observés après recuisson à l'air à 230°C. Se basant sur notre modèle étendu de Goodman, on a cru que l'augmentation en R fût causé par la diffusion dehors d'accepteurs Se venant des surfaces. Avec l'aide de l'approximation d'épuisement, des profiles d'accepteurs effectifs apparents ont été obtenus dont la validité fût considérée dans la présence de couche interfacial. L'uniformité en gros fût meilleurs dans la direction de croissance que dans la plaine transversale.

Acknowledgments

Never will the writer find the most appropriate words to appreciate Dr. I. Shih for his academic supervision, non-academic assistance, and above all his patience and tolerance, which have alleviated numerous critical situations of any nature since September 1985.

The writer owes his entire life to his parents who have always been sacrificing their owns for the very best tomorrow of their son. Infinite spiritual support has been inducted from his Holy brother and sister as well when he is down. Their love, the greatest of all, are memorable forever.

The writer has received significant help, advice and encouragement from his long time colleages W.L. Choi and C.X. Qiu, so wishing them a good life ahead in Canada.

The writer must acknowledge Miss S.M. D'Aoust for her full effort in text-processing and translating the English abstract into French.

Great thanks are attributed to the sponsoring of the present study by the National Science and Engineering Research Council of Canada.

C.L. Chan

Contents

1 Introduction

2 Classical Schottky Barrier Theory

3 Device Fabrication

4 Electrical Characterization Techniques

5 Results & Interpretation

5.1 Current Characteristics

5.3 Differential Capacitance Characteristics

Notation

A	geometrical area of Schottky contact
A^*	Richardson constant with $m^* = 4\pi m^* q k^2/h^3$
C	Schottky or MIS junction capacitance
C_d	depletion capacitance = dQ_d/dV_d
C'	capacitance measured by LCR bridge
D_{sb}	density of surface states in equilibrium with s.c.
E_c	conduction band edge of s.c.
E_{fi}	intrinsic fermi level of s.c.
E_{fm}	metal fermi level
E_{fs}	bulk fermi level of s.c.
E_g	energy gap of s.c.
E_v	valence band edge of s.c.
E_{oo}	quantum-mechanical tunneling parameter defined by (2.18)
f, ω	test signal frequency
G	Schottky or MIS junction conductance
G'	conductance measured by LCR bridge
h	Planck's constant = 4.14×10^{-15} eV-sec
I	d.c. current
I_o	reverse saturation d.c. current
k	Boltzmann's constant = 8.62×10^{-5} eV K^{-1}
m_o	mass of electron in free space = 9.1×10^{-31}kg
m^*	effective mass of majority carriers in s.c.
n	ideality factor
N_A	effective acceptor concentration
N_D	effective donor concentration

N_i	intrinsic carrier concentration
N_v	effective density of bulk states at E_v
q	elementary charge = 1.6×10^{-19} coulomb
R	series resistance (usually from quasi-neutral region)
T	absolute temperature
V	forward bias
V_d	s.c. surface potential or band bending
V_{do}	0-bias value of V_d or diffusion potential
V_i	electrostatic potential drop across interfacial insulator
V_{io}	0-bias value of V_i
V_i^o	flat-band value of V_i
V_I	voltage intercept of the linear C^{-2}/V plot
V_r	reverse bias = $-V$
W	depletion layer width
δ	interfacial insulator thickness
ε_i	interfacial insulator permittivity
ε_s	s.c. permittivity
μ_p	hole mobility in p-s.c.
ξ	E_c(bulk) - E_{fs} for n-s.c. or E_{fs} - E_v(bulk) for p-s.c.
ϕ_b	Schottky barrier height
ϕ_{bo}	0-bias value of ϕ_b
ϕ_b^o	flat-band ($V_d = 0$) value of ϕ_b
Φ_m	work function of metal
Φ_s	work function of s.c.
χ_i	mean insulator barrier = E_v(s.c.) - E_v(insulator) at $x = 0$
χ_s	electron affinity of s.c.

Chapter 1

Introduction

1.1 Historical

The development of high conversion efficiency single-crystal (12%) n-CdS/p-$CuInSe_2$ [1.1] and thin-film (14.1%) n-CdS/p-$CuInSe_2$ [1.2] hetero-junction solar cells have made the importance of the semiconductor $CuInSe_2$ recognized. It belongs to the I-III-VI_2 chalcopyrite crystal family [1.3] with a direct band gap of 1.01 eV [1.4] and a dielectric constant of 9.3 [1.5]. Crack-free ingots with large grains have been produced by Parkes et al. [1.6] using a 2-step growth technique of vacuum-fusion followed by horizontal zone-melting. Polycrystalline thin films have been vacuum-evaporated onto heated ceramic substrates by Mickelsen and Chen [1.7]. The conduction type of the as-prepared material is dependent on the growth or deposition conditions and has never been reported as intrinsic. The conduction type is also controllable by subsequent annealing and diffusion [1.6, 1.8]. Extensive electrical and optical properties of the single crystal material can be found from [1.5, 1.9, 1.10, 1.11]. The material has also been studied from the device point of view. For homo-junctions, the forward currents are usually dominated by recombination in the depletion layer [1.12, 1.13] and the capacitances are always affected by deep levels [1.14] at low f. For Schottky junctions, the electrical characteristics are more complicated since the junctions form right at the free surfaces [1.4, 1.8, 1.15, 1.16, 1.17, 1.18]. Various transport models over different bias regions have been proposed: MIS majority/minority (injection) tunneling with interface effects, recombination, space-charge- and series-resistance-limited currents. Such wide diversity in carrier flow behaviours is mainly due to the differences in surface properties and ohmic contact methods. The ohmic contacts obtained by locally diffusing deposited-indium into the p-$CuInSe_2$ substrate backs in Rao et al.'s diodes [1.18] is questionable. Shih et al. [1.12, 1.13] and Parkes et al. [1.8] have successfully fabricated rectifying n^+-p homo-junctions by this technique! Except for the Au/n-$CuInSe_2$ diodes of Parkes et al. [1.8], the reported barrier heights from the log(I) /V intercepts are substantially smaller than the C^{-2}/V intercepts at high frequency.

To-date, knowledge on the surface properties of the new material $CuInSe_2$ and its related interface device physics have been limited because 1) most of the existing energy band, transport and capacitance theories were initially established for Si, III-V and II-VI systems and 2) not enough work has been done. If these are well understood and controlled, its present limit of application performance will likely be exceeded.

1.2 The Present Work

So far only two papers [1.4, 1.18] have reported on metal/p-$CuInSe_2$ systems. Despite of the non-idealities in these results, the authors have based their analysis on the Schottky-Mott band structure which they had to abandon at the end. In this study, the dark I/V and C/V characteristics of the Al/p-$CuInSe_2$ Schottky junctions fabricated by vacuum-evaporation are presented and discussed, with an aim to obtain some surface properties of our p-$CuInSe_2$ single-crystals from the Bridgman growth. Three surface cleaning methods, one abrasive polishing AP and two AP + chemical etchings, were used since they have been adopted before for $CuInSe_2$ (section 3.2). Aluminium has been chosen as the Schottky contact since it is the best compromise between small work function (4.17 eV, [1.19]) and low chemical reactivity in the metal list to form a Schottky barrier at 0-bias in theory for our typical p-doping level as determined by Hall effect measurement. The T-dependence (218 to 298^{o}K) of the current and the f-dependence (1 kHz to 100 kHz) of the capacitance have also been studied in order to observe a wider spectrum of physical phenomena. These have rarely been done before for the $CuInSe_2$ Schottky diodes.

The thesis was arranged in this way: Chapter 2 is a brief review of the early Schottky barrier theory. Chapter 3 is devoted to device fabrication. Chapter 4 describes the I/V and C/V measurement systems and techniques. Chapter 5 displays and discusses the electrical characteristics. Chapter 6 concludes the thesis. Our processes to interpret the results are to 1) observe generally 2) to examine any possible explanation from the classical theory and 3) to use the advanced models with the proper assumptions and modifications if necessary.

Chapter 2

Classical Schottky Barrier Theory

2.1 Ideal Schottky Barrier

When a metal with work function Φ_m is brought into intimate contact with an extrinsic semiconductor with work function Φ_s, such that either one of the following conditions is satisfied,

$$\Phi_m > \Phi_s \qquad \text{for n-type semiconductor} \qquad (2.1)$$

$$\Phi_m < \Phi_s \qquad \text{for p-type semiconductor} \qquad (2.2)$$

then an electrostatic potential barrier (parabolic) is formed at the semiconductor surface (fig.2.1). The role of this barrier is to obstruct the flow of majority carriers from the semiconductor bands into the metal. The barrier height ϕ_b is commonly defined as the energy difference between the barrier top at the junction (x = 0) and the metal fermi level E_{fm}. From fig.2.1,

$$\phi_{bn} = \Phi_m - \chi_s \qquad \text{for n-type s.c.} \qquad (2.3)$$

$$\phi_{bp} = E_g /q + \chi_s - \Phi_m \qquad \text{for p-type s.c.} \qquad (2.4)$$

where E_g and χ_s are the forbidden gap and the electron affinity of the semiconductor respectively. Eqns. (2.3) and (2.4) together is the Schottky-Mott limit [2.1] for the simplest contacts (see section 2.3).

The surface potential or band bending V_{do} (diffusion potential) at thermal equilibrium (V = 0) is given by

$$V_{do} = \Phi_m - \Phi_s = \Phi_{ms} \qquad \text{for n-type s.c.} \qquad (2.5)$$

$$V_{do} = \Phi_s - \Phi_m = \Phi_{sm} \qquad \text{for p-type s.c.} \qquad (2.6)$$

A forward bias of this magnitude would flatten the semiconductor bands ($V_d = 0$, $\mathcal{E}_m = 0$ and $Q_d = 0$).

2.2 Image Force Lowering (Schottky Effect)

The electrostatic force experienced by a majority carrier at the semiconductor surface is, strictly speaking, a sum of the usual electric field associated with the depletion space charge and the Coulomb force associated with the induced opposite charge (mirror image) inside the metal [2.2]. Consequently the barrier top is lowered in energy by $\Delta\phi_{b1}$ and displaced from the junction towards the semiconductor by x_m (fig.2.2), derived as

$$\Delta\phi_{b1} = (q\mathcal{E}_m / 4\pi\varepsilon_s)^{1/2} \qquad (2.7)$$

$$x_m = (q/16\pi\mathcal{E}_m\varepsilon_s)^{\frac{1}{2}} \qquad (2.8)$$

where ε_s is the semiconductor permittivity and $\mathcal{E}_m$ is the maximum electric field at the surface. $\mathcal{E}_m$, a function of bias and doping, will be discussed in section 2.5. Since $\Delta\phi_{b1}$ increases with $\mathcal{E}_m$, the resultant ϕ_b decreases with $\mathcal{E}_m$. The image force lowering of ϕ_b is normally negligible at moderate doping.

2.3 Generalized Bardeen Model for Interface Effects

Bardeen [2.3] proposed that the existence of a sufficiently large surface state density D_s at the metal-semiconductor (MS) interface would lead to a ϕ_b independency on Φ_m and χ_s. Cowley and Sze [2.4] generalized the Bardeen's statement by considering an MIS (metal-insulator-semiconductor) band model in fig.2.3 for n-type semiconductor and assuming that

1) D_s is uniform across the band gap at the insulator-semiconductor (IS) interface
2) electron population in interface states is determined by E_{fm}, i.e., $E_{fs} = E_{fm}$ at the semiconductor surface
3) the interface is electrically neutral when states below an intra-gap energy level ϕ_0 above E_v are all filled

ϕ_b is now reduced from that in the Schottky-Mott limit by the voltage drop V_i across the interfacial layer. Applying Gauss's theorem on the IS interface, Cowley and Sze [2.4] obtained

$$\phi_b = \phi_b^o - \alpha \mathcal{E}_m \tag{2.9}$$

$$\phi_b^o = \gamma(\Phi_m - \chi_s) + (1 - \gamma)(E_g/q - \phi_o) \tag{2.10}$$

$$\alpha = \delta\varepsilon_s/(\varepsilon_i + qD_s\delta) \tag{2.11}$$

$$\gamma = \varepsilon_i/(\varepsilon_i + qD_s\delta) \tag{2.12}$$

where ϕ_b^o is the flat-band barrier height, α and γ are surface parameters, ε_i and ε_s are the permittivities of the insulator and the semiconductor respectively, and δ is the insulator thickness. Two special cases are of interest:-

1) no interfacial layer, $\delta = 0$

$\alpha = 0,\ \gamma = 1,\ \phi_b = \phi_b^o = \Phi_m - \chi_s$ Schottky-Mott limit

2) $\delta > 0$ and $D_s \to \infty$,

$\alpha = 0,\ \gamma = 0,\ \phi_b = \phi_b^o = E_g/q - \phi_o$ Bardeen limit

E_{fm} is pinned to the neutral level ϕ_o by the high D_s.

In general, ϕ_b lies between the two limits and depends partially on ϕ_m and partially on the interface properties, i.e., $0 < \gamma < 1$. It also decreases with $\mathcal{E}_m$. For a p-type semiconductor, the corresponding ϕ_b expressions are

$$\phi_{bp} = \phi_{bp}^o - \alpha|\mathcal{E}_m| \tag{2.13}$$

$$\phi_{bp}^o = \gamma(E_g/q + \chi_s - \Phi_m) + (1 - \gamma)\phi_o \tag{2.14}$$

where α and γ are given by eqns. (2.11) and (2.12) respectively. The sum of ϕ_{bn} in eqn. (2.10) and ϕ_{bp} in eqn. (2.14) is E_g. This holds whenever the p- and n-semiconductors have the same surface preparation and are contacted with the same metal.

2.4 Carrier Flow

The I-V characteristics of a Schottky diode are governed by the transport of the charged carriers across the surface barrier and the MS interface. There are three major mechanisms [2.2], as described below, of dominances depending on the semiconductor material, doping, T, V as well as ϕ_b. Recombination in the neutral bulk region (minority carrier injection) [2.5], being less important, will be omitted here.

1) thermionic emission (TE)

In TE, majority carriers with longitudinal kinetic energy $mV_x^2/2$ in excess of the barrier potential $V_d = V_{do} - V$, would be emitted into the metal. Collision of any nature within the depletion layer is neglected. Using the Maxwell-Boltzmann statistics, Bethe [2.6] obtained the current density J as

$$J = A^*T^2 \exp(-q\phi_b/kT)[\exp(qV/kT)-1] \qquad (2.15)$$

$$A^* = 4\pi q m^* k^2 / h^3 \qquad (2.16)$$

A* is the Richardson constant, k is the Boltzmann's constant. h is the Planck's constant, and m* is the effective mass of the majority carrier. Later, Crowell and Sze [2.7] modified A* into A**, the effective Richardson constant, accounting for optical phonon scattering, MS interface quantum mechanical reflection and tunneling. Higher T would increase the thermal energy of the carriers. Larger forward bias would decrease the barrier potential. Both effects would allow more carriers to surmount over the barrier and hence increase the current.

2) thermionic-field emission (TFE) & field emission (FE)

As the dopant concentration increases, the barrier width W decreases. Quantum mechanical tunneling of majority carriers through the barrier can occur. The tunneling probability P [2.2] through a triangular barrier at E above E_c(bulk) has been derived for n-type semiconductor as

$$P = \exp[-2(qV_d - E)^{3/2}/3E_{oo}(qV_d)^{1/2}] \qquad (2.17)$$

$$E_{oo} = (hq/4\pi)(N_D/m^*\epsilon_s)^{\frac{1}{2}}\ \text{eV} \tag{2.18}$$

Padovani and Stratton [2.8] integrated eqn. (2.15) from E_c(bulk) to the barrier top and obtained the following forward tunneling flux expressions under three different T and doping conditions:

a) $E_{oo} >> kT$

At low T and heavy doping, the barrier is thin enough to permit carrier emission directly from occupied states at E_{fs} into the metal near the bottom (fig.2.4(a)). This is called FE and

$$J = J_{oF}\exp(qV/E_{oo}) \qquad V > 3kT/q \tag{2.19}$$

where J_{oF}, the reverse FE saturation current density, varies with T weakly.

b) $E_{oo} \sim kT$

At moderate T and doping, the barrier is wider and only carriers with sufficient thermal energy can tunnel at E_m near the thinner upper barrier (fig.2.4(b)). This is called TFE and

$$J = J_{oTF}\exp(qV/E_o) \qquad V > 3kT/q \tag{2.20}$$

$$E_o = E_{oo}\coth(E_{oo}/kT) \tag{2.21}$$

where J_{oTF}, the reverse TFE saturation current density, changes with T significantly.

c) $E_{oo} << kT$

At high T and low doping, the barrier is too wide and the carriers must be thermally emitted over the barrier (fig.2.4(c)). This is just TE and

$$J = J_{oT}\exp(qV/kT) \qquad V > 3kT/q \tag{2.22}$$

$$J_{oT} = A^{**}T^2\exp(-q\phi_b/kT) \tag{2.23}$$

J_{oT}, the reverse TE saturation current density, is strongly dependent on T.

3) recombination in the depletion region (RD)

Electrons and holes usually recombine (generated under reverse bias) indirectly via localized deep (E_t >> kT from band edges) bulk traps, due to defects or impurities, in the depletion layer. Similar to that in p-n homo-junction [2.9], the current density is given by

$$J = J_{or}[\exp(qV/2kT)-1] \tag{2.24}$$

$$J_{or} = qN_iW/2\tau_r \tag{2.25}$$

$$N_i = (N_cN_v)^{\frac{1}{2}}\exp(-E_g/2kT) \tag{2.26}$$

N_i is the intrinsic carrier concentration, W is the depletion layer width and τ_r is the recombination life-time of the minority carriers within the depletion region. N_c and N_v are the effective energy state densities per unit volume at E_c and E_v respectively. They are proportional to $T^{3/2}$.

It is useful to examine the relative importances of the various flow mechanisms controlling practical devices by fitting the experimental (V,I) points into the empirical I-V relation

$$I = I_o \exp[q(V-IR)/nkT] \qquad V > 3kT/q \qquad (2.27)$$

R is any possible series resistance due to semiconductor bulk or diode connection. n, the ideality factor is greater than 1 in practice. If n is close to 1, TE is dominant. If n is close to 2, RD is dominant. If TFE or FE is important, n ranges widely, depending on T and doping, as $(E_{oo}/kT)\coth(E_{oo}/kT)$.

2.5 Ideal Differential Capacitance

The maximum electric field $\mathcal{E}_m$ at the semiconductor surface for an intimate contact under a reverse bias V_r, neglecting the surface charge due to the minority carriers, has been solved from the Poisson's equation as [2.2]

$$\mathcal{E}_m = [(2qN/\varepsilon_s)(V_{do} + V_r - kT/q)]^{\frac{1}{2}} \qquad (2.28)$$

N is the uniform shallow dopant density. The kT/q term, a correction to the abrupt depletion approximation, allows for smooth charge transition near x = W. By Gauss' law, the space charge Q_d per unit area due to the uncompensated shallow impurity ions in the depletion layer is

$$Q_d = \varepsilon_s \mathcal{E}_m \qquad (2.29)$$

The ideal differential capacitance C per unit area is

$$C = dQ_d/dV_r = (q\varepsilon_s N/2)^{\frac{1}{2}}(V_{do} + V_r - kT/q)^{-\frac{1}{2}} \qquad (2.30)$$

2.6 Barrier Height Measurement

1) photoelectric effect

The experimental set-up for this technique is shown in fig.2.5-(a). Electrons are excited from E_{fm} into the conduction band by monochromatic illumination when $h\nu > q\phi_b$, process "a" in fig. 2.5(b). When $h\nu > E_g$, band-to-band generation of electron-hole pairs occurs, process "b" in fig.2.5(b). According to Fowler's theory [2.10], the short-circuit current I_p per photon (photo-response) by process "a" is given by

$$I_p^{\frac{1}{2}} \propto h\nu - q\phi_b \qquad q\phi_b + 3kT < h\nu < E_g \qquad (2.31)$$

A plot of $I_p^{\frac{1}{2}}$ vs. $h\nu$ would give ϕ_b from the linearly extrapolated intercept.

2) current-voltage plot

a) at a fixed T

This method can determine ϕ_b accurately only if n is not far from 1. The linear portion (before R effect becomes important) of the log(I) vs. V plot can be extrapolated to the log(I) axis to yield I_{ot}. ϕ_b is then obtained directly from eqn. (2.23) if A** is known.

b) T-dependence (Richardson plot)

The current I is measured as a function of T at a fixed forward bias V. A plot of $\log(I/T^2)$ vs. 1/T would yield the activation energy $q(\phi_b - V)$ from the slope and A** from the intercept. Alternatively, I_o may be used instead of I in which case the activation energy is simply

$q\phi_b$.

When TE is not dominant, I_o would be a complicated function of V, T, ϕ_b, as well as other bulk/surface properties. Then it is hard to obtain ϕ_b from the experimental I-V data. It may even happen that the transport mechanism cannot be modelled by the simple exponential form of eqn. (2.27).

3) capacitance-voltage plot

Eqn. (2.30) can be rewritten as

$$C^{-2} = (2/q\varepsilon_s N)(V_{do} + V_r - kT/q) \qquad (2.32)$$

The experimental (V_r, C^{-2}) points can be fitted into the linear eqn. (2.32) to obtain V_{do} from the intercept $V_I = V_{do} - kT/q$, N from the slope and ϕ_b from

$$dC^{-2}/dV_r = 2/q\varepsilon_s N \qquad (2.33)$$

$$\phi_b = V_{do} + \xi \qquad (2.34)$$

where ξ, the position of E_{fs} relative to the band edge in the bulk, can be determined by N_i and N using the Boltzmann's relations [2.11]

$$N_D = N_i \exp[(E_{fs} - E_{fi})/kT] \quad \text{for n-type s.c.} \qquad (2.35)$$

$$N_A = N_i \exp[(E_{fi} - E_{fs})/kT] \quad \text{for p-type s.c.} \qquad (2.36)$$

where E_{fi} is the intrinsic fermi level.

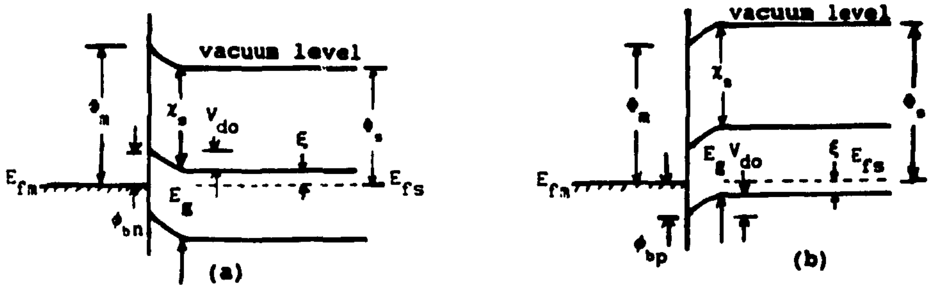

fig.2.1 Ideal Schottky barrier at thermal equilibrium
(a) n-type s.c. (b) p-type s.c.

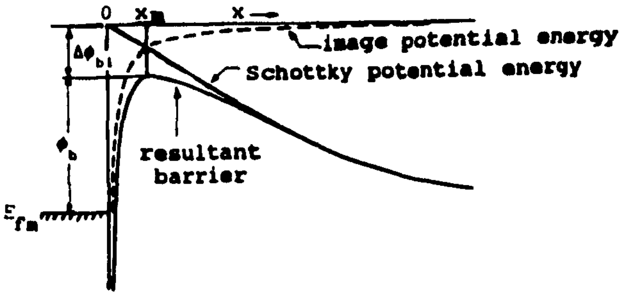

fig.2.2 Schottky barrier lowered by image force, n-type s.c.

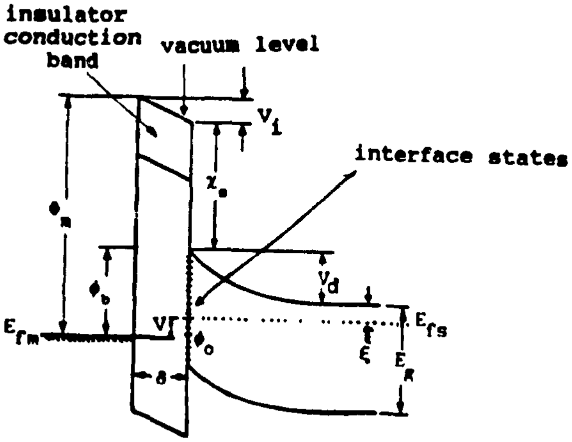

fig.2.3 MIS Schottky barrier for n-type s.c. at forward bias V

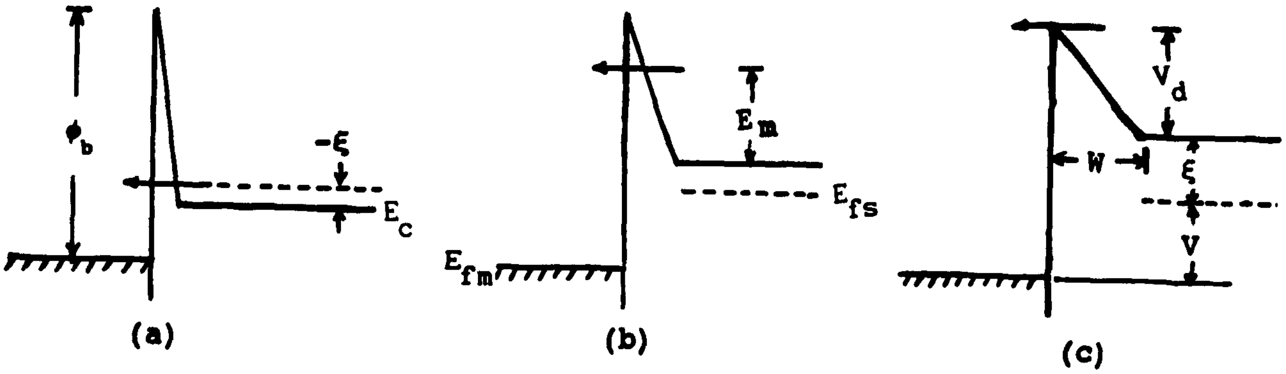

fig.2.4 Tunneling through and emission over a triangular Schottky barrier (a) FE (b) TFE (c) TE

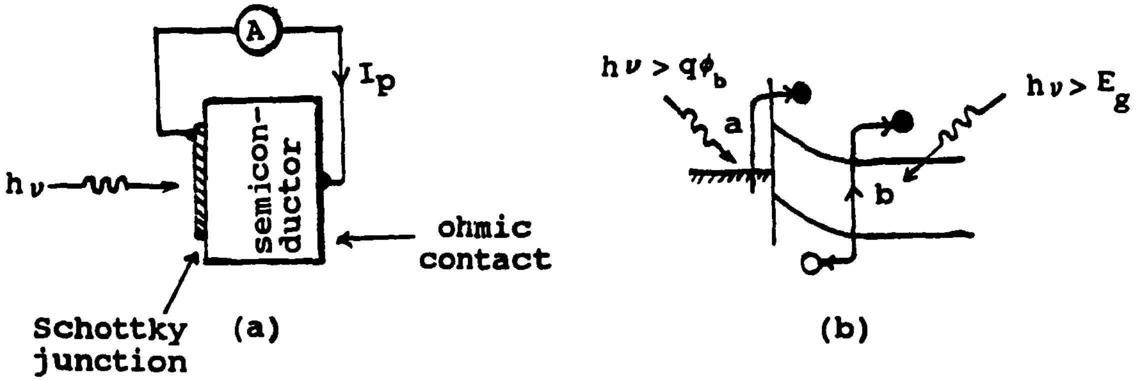

fig.2.5 Photoexcitation in MS systems (a) experiment for barrier height measurement (b) photoelectric "a" & photovoltaic "b" emissions

Chapter 3

Device Fabrication

3.1 Introduction

The physical properties of a semiconductor substrate and the electrical characteristics of its related devices are strongly dependent on the preparation techniques and conditions. This chapter describes the preparations of substrate materials, surfaces, rectifying junctions as well as ohmic contacts.

3.2 Substrate Preparation

The substrates used for Schottky diode fabrication are p-type $CuInSe_2$ single-crystals (fig.3.1, typical dimensions 8x5x4 mm^3) cut from Bridgman-grown ingots [3.1] perpendicularly to the growth axis. Fig. 3.2 is a schematic diagram of the Bridgman system for the growth of $CuInSe_2$ ingots. The ampoule was prepared from a clean quartz tube with an I.D. of 1.0 cm, an O.D. of 1.3 cm and a length of 12 cm. Another 6 mm diameter quartz tube was thermally joined to one end of the ampoule for pulling purpose. In each growth run, 12 grams of stoichiometrically weighed elements Cu, In and Se (nominal purity 69's, 69's and 59's respectively) were used for the initial compound synthesis. Typical electrical resistivity, Hall mobility and hole concentration for the as-grown material are respectively 3 ohm-cm, 60 $cm^2V^{-1}sec^{-1}$ and $4x10^{16}cm^{-3}$ at 298^oK. The flatter surface of each sample was abrasively polished with 0.3 micron alumina powder until it looked shinny. No attempt was made to identify the orientation of these crystal faces. Chemical etching was then taken at room temperature for some samples in 1:1 HCl/HNO_3 [1.12] for 5 min., and for some samples in 1:8 aqueous $K_2Cr_2O_7$(saturated)/H_2SO_4 [1.15, 3.2] for 30 min. The rest were not chemically etched at all. All samples were rinsed in trichloroethylene and acetone solvents , and then stored in 2-propanol prior to the evaporation of the rectifying Al contacts.

3.3 Evaporation of Al Schottky Contacts

Thin Al films (about 1 micron thick) were vacuum-deposited on the prepared semiconductor surfaces from a multiple-loop-resistance-heated tungsten filament on which tiny U-shaped Al wires were hung. An Edwards coating system, model E306A (fig.3.3), with a liquid nitrogen-trapped oil-diffusion-pump was operated at a pressure of about 10^{-6} Torr. The geometry of the Al contacts was confined by 7.85×10^{-3} and $9.62 \times 10^{-2} cm^2$ circular holes in 0.05 inch thick rigid Al masks. The remaining parts of the crystals were wrapped with Al foil. The shutter was initially closed for 30 seconds once the Al hangers started evaporating. This could avoid the exposed parts of Al (usually Al_2O_3) from depositing on the substrates and hence a dirty Schottky contact. The substrate temperature was 298°K.

3.4 Ohmic Contacts

After a sand-paper blasting, the bottom face of each sample was stuck on an aluminum holder via heat-treated (at 100°C for 30 min.) silver epoxy (EPO-TEK H20E, Epoxy Technology Inc.). This became the back ohmic contact (the epoxy has been experimentally proven to form a good ohmic junction with our p-$CuInSe_2$ crystals [3.3]). Initially a stainless steel needle touch contact was used for the top. But it seemed that the electrical characteristics were quite unstable, when the position of the pressure supplying magnet was perturbed. So smaller indium contacts were then evaporated on the Al regions for top soldering and wiring instead. A cross-section of a finished Al/p-$CuInSe_2$ Schottky diode with ohmic contacts was drawn in fig.3.4. Fig.3.5 is a photograph of three finished devices. Table 3.1 summaries the preparation features for some representative samples, the results of which are to be presented in Chapter 5. Once fabricated, most devices were subjected to a short heat treatment in air at 230°C before characterization. This generally helped reducing the reverse leakage.

Table 3.1 List of Al/p-$CuInSe_2$ diodes being studied

Device No.	Surface preparation	No. of Al contacts	Al contact area (cm^2)	Annealing (air, 230°C) time(min.)
AP1	AP[1]	1	9.62×10^{-2}	20
AP2	AP	1	9.62×10^{-2}	15
AP3	AP	6	7.85×10^{-3}	0[2]
KC01	CE1[3]	1	9.62×10^{-2}	0
KC01R[4]	CE1	1	9.62×10^{-2}	15
KC02	CE1	1	7.85×10^{-3}	10
HH1	CE2[5]	1	9.62×10^{-2}	15
HH2	CE2	2	7.85×10^{-3}	10

[1] AP = abrasive polishing.

[2] As-fabricated.

[3] CE1 = AP + 1:8 $K_2Cr_2O_7/H_2SO_4$ chemical etching.

[4] KC01R was obtained by repolishing KC01 and re-evaporating Al 3 days later, KC01 has been annealed successively for a total of 50 min. (the 15 min. for KC01R not included) during this period.

[5] CE2 = AP + 1:1 HCl/HNO_3 chemical etching.

fig.3.1 p-$CuInSe_2$ materials from Bridgman crystal growth

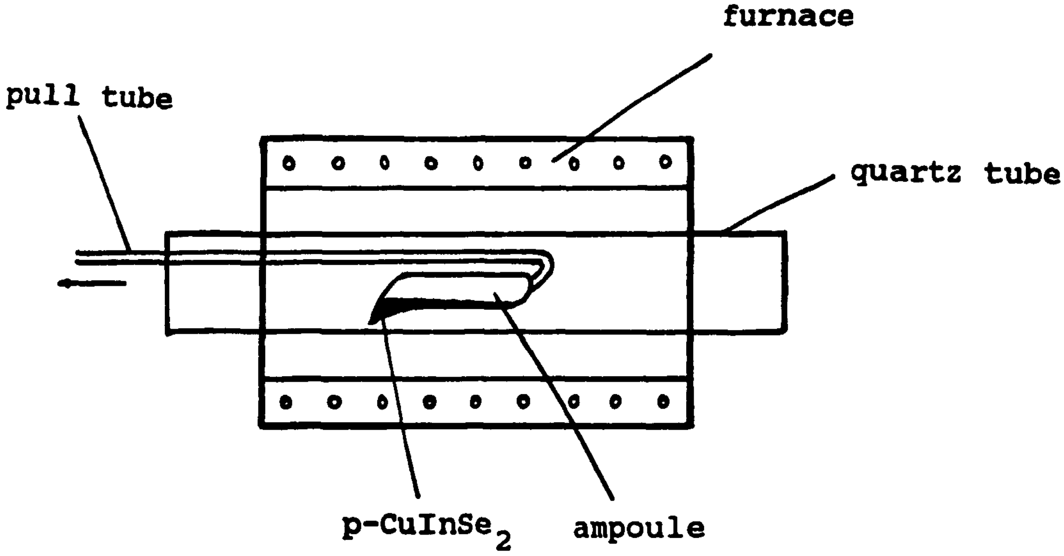

fig.3.2 Bridgman crystal growth system in the horizontal configuration

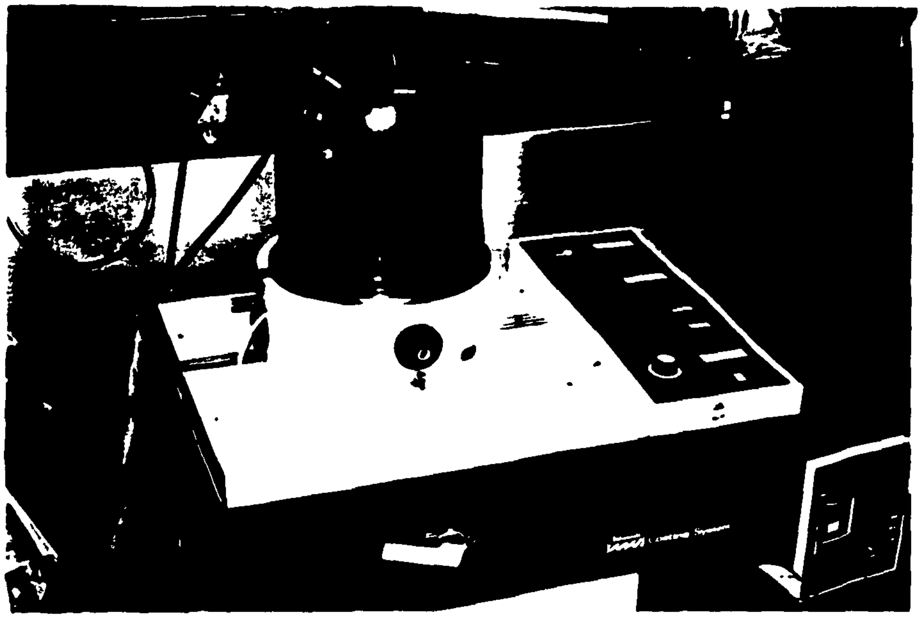

fig.3.3 Edwards coating system, model E306A

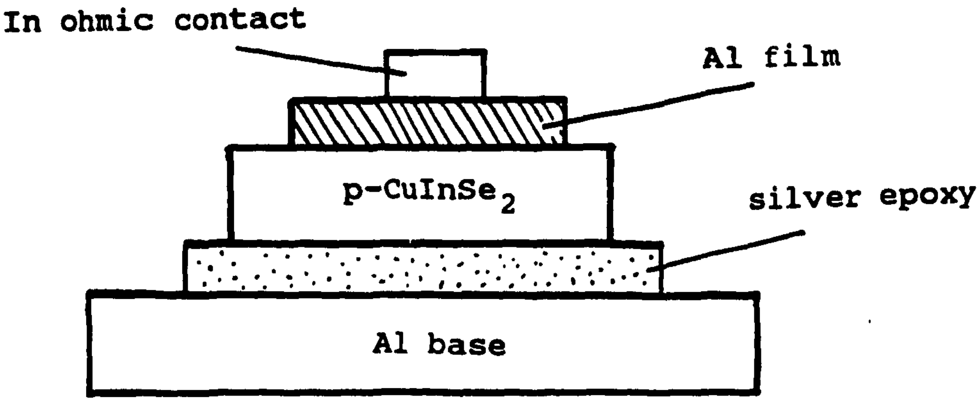

fig.3.4 Cross-section of Al/p-CuInSe$_2$ Schottky diode

fig.3.5 Real Al/p-$CuInSe_2$ Schottky diodes

Chapter 4

Electrical Characterization Techniques

4.1 Introduction

The current-voltage characteristics of a Schottky diode reflect the carrier transport mechanisms and probably its barrier height. The measurements of the voltage dependence of the differential capacitance can be used to determine the barrier height and are also useful to understand the nature of the semiconductor surface in regard to shallow impurties, deep traps and interface effects. This chapter describes the measurement techniques adopted in our lab for obtaining such external characteristics of the Al/p-CuInSe$_2$ diodes.

4.2 Current/Voltage Measurement Techniques

The dark d.c. current was measured by an HP-4145A semiconductor parameter analyzer (fig.4.1). HP-4145A is a 16-bit multi-microprocessor-based test instrument for measuring, analyzing and graphically displaying the d.c. characteristics of common semiconductor devices and ICs. The box beside it (fig.4.1) is an HP-16058A test fixture, the SMU channels (Stimulus/Measurement Units, 4 available) of which are to be electrically connected to the terminals of the device under test. Each SMU is programmable to monitor current when operating as a variable/constant d.c. voltage source, or to monitor voltage when operating as a variable/constant d.c. current source. The simplified circuit of a SMU is shown in fig.4.2. The fixture cover can be closed to carry out measurements under a dark condition. A few specifications of HP-4145A with HP-16058A are listed in Table 4.1. For diode testing, HP-4145A functions in this way:-

1) Two SMU channels, assigned as 'SMU1' and 'SMU3' are electrically connected to the diode accordingly.

2) A variable d.c. voltage source is assigned to the SMU1 while a constant d.c. voltage is maintained at the SMU3. The current is monitored by the SMU1. The source output is set up in terms of three parameters: start, stop and step. It can be applied to the device linearly or logarithmically (base 10, 25 or 50) in time to complete a single bias sweep.

3) The voltage integration time t_i must be sufficiently longer than the transient delay time t_d in order that the current would reach d.c. steady state once the source starts to change. This is illustrated in figs.4.3 and 4.4 for a linear forward bias sweep. Measurement should occur at the instance t_m. The point (V_m, I_m) would then appear on the CRT display as a bright spot.

For the present diode study, the bias typically ranges from -1 to +1 V with a step of 0.01 V. The integration time used is 0.02 sec. For temperature dependent characteristics, a cryostat (fig.4.5, courtesy of I. Shih), inside which each device was mounted, was first cooled down to 218°K by liquid N_2. An I-V measurement sweep was taken at every 15°K increment during the steady warm-up cycle ended at 298°K. The temperature, which essentially remained constant over the bias sweep, was monitored by a type-J thermocouple and a digital voltmeter. All numerical data were recorded graphically by an HP-7475A plotter. The whole measurement set-up is shown in fig.4.6. The PC was instructed by the "Current" subroutine in a BASIC software named "Total".

4.3 Capacitance/Voltage Measurement Techniques

The dark and room temperature differential capacitance was measured by an HP-4274A multi-frequency LCR meter (fig.4.7). HP-4274A is a 16-bit microprocessor-based test instrument for measuring the various a.c. parameters of an admittance/impedance element at relatively low frequencies. Some specifications of HP-4274A are listed in Table 4.2. The operating principle of an LCR meter is like this: For admittance ($Y = G + j\omega C$) measurement, the circuit mode is set to equivalent parallel circuit. A sinusoidal small test voltage $v = |v|\exp(j\omega t)$ is applied across the device, where $|v|$ and ω are the adjustable amplitude and frequency respectively. At steady state, a small current $i = |i|\exp[j(\omega t + \theta)]$ will flow through the device, where $|i|$ and θ are the monitorable amplitude and phase difference respectively. The admittance Y is then calculated as $Y = i/v = |i/v|\exp(j\theta)$ so that $G = |i/v|\cos(\theta)$ and $C = |i/v|\sin(\theta)/\omega$. A practical limitation on capacitance measurement for HP-4274A is the parallel conductance of the device. If G is too large that the dissipation factor $D = G/\omega C > 10$, measurement will be disabled. In such case, either the test frequency has to be raised or the maximum reverse bias has to be decreased (reduce the leakage G) in order to decrease D below 10. The internal d.c. bias source can be remotely controlled by manually setting the 3-digit switch on the HP-16023B d.c. bias controller. It may also be automatically controlled by computer through the HP-82169A bias interface. The internal/external d.c. bias is monitorable by a digital voltmeter connected to the d.c. bias monitor output on the rear panel. For the present study, the bias (internal supply) typically ranges from -1 to +0.2 V with a step size of 0.025 V. It was incremented at a time rate slow compared with the test signal (10 mV rms) frequency. The test frequency range is from 1 kHz to the instrument limit of 100 kHz. Measurements below 1 kHz are usually difficult at larger reverse bias. All numerical data were automatically stored in diskettes and recorded graphically by an HP-7475A plotter. The whole measurement set-up is shown in fig.4.8. The PC was commanded by the "Capacitance" subroutine in "Total".

Table 4.1 Some specifications of HP-4145A semiconductor parameter analyzer & HP-16058A test fixture

---

Source resolution: voltage = 1 mV, current = 1 pA

Measurement resolution: voltage = 1 mV, current = 50 fA

Compliance: voltage = 0 to 100 V, current = 50 pA to 100 mA

SMU input resistance (voltage monitor/current source): > 10^{12} ohm

SMU residual resistance (current monitor/voltage source): 0.4 ohm

Display buffer capacity: 8 sweeps x 512 measurement points/sweep

---

Table 4.2 Some specifications of HP-4274A multi-frequency LCR meter

---

Measurement circuit mode: series (L-R) and parallel (C-G)

Parameter range: C = 0.01 fF to 1999.0 mF
L = 0.001 nH to 1999.9 H
G = 0.01 nS to 199.99 S
R = 0.001 mohm to 19.999 Mohm

Frequency range: 100 Hz to 100 kHz

Test signal level: 1 mV to 5 V rms

d.c. bias: internal = ±35 V and ±99.9 V max
external = ±35 V and ±200 V max

d.c. bias monitor output resistance: 30 kohm

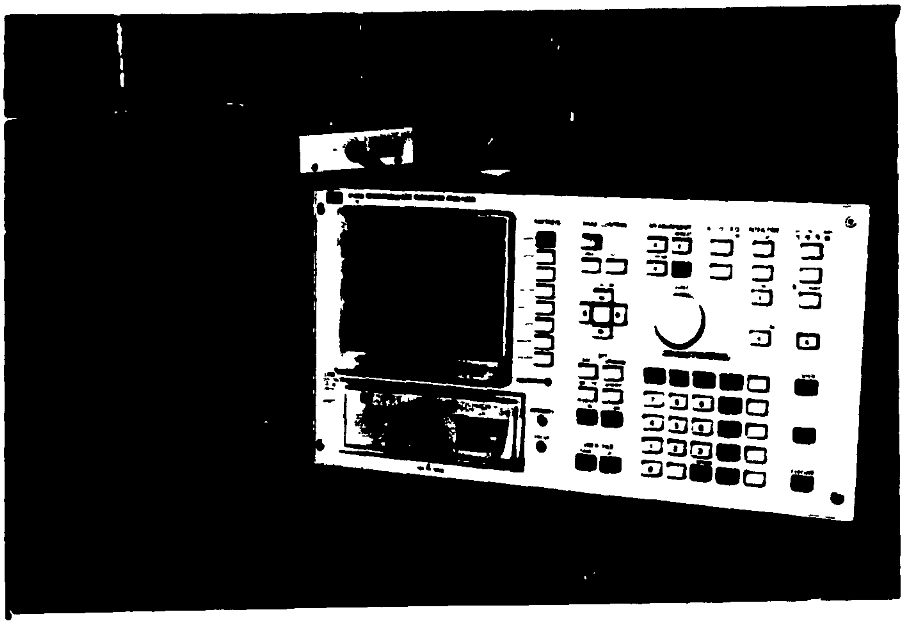

fig.4.1 HP-4145A semiconductor parameter analyzer

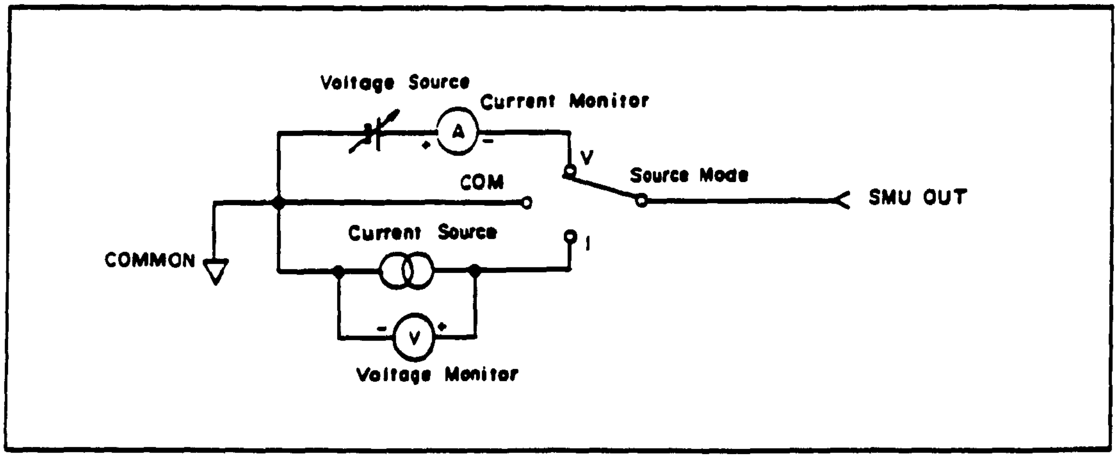

fig.4.2 Simplified circuit of a SMU on HP-16058A

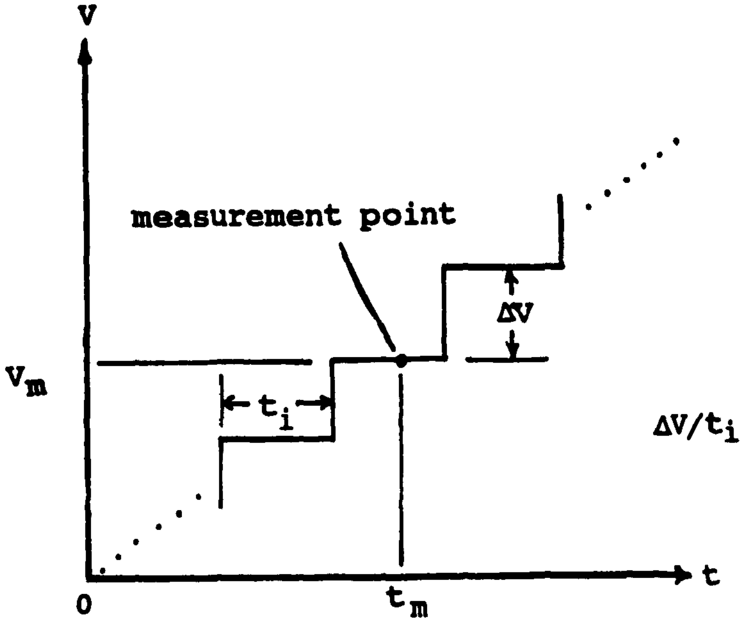

$\Delta V / t_i$ = constant sweep rate

fig.4.3 Linear bias sweep for a diode

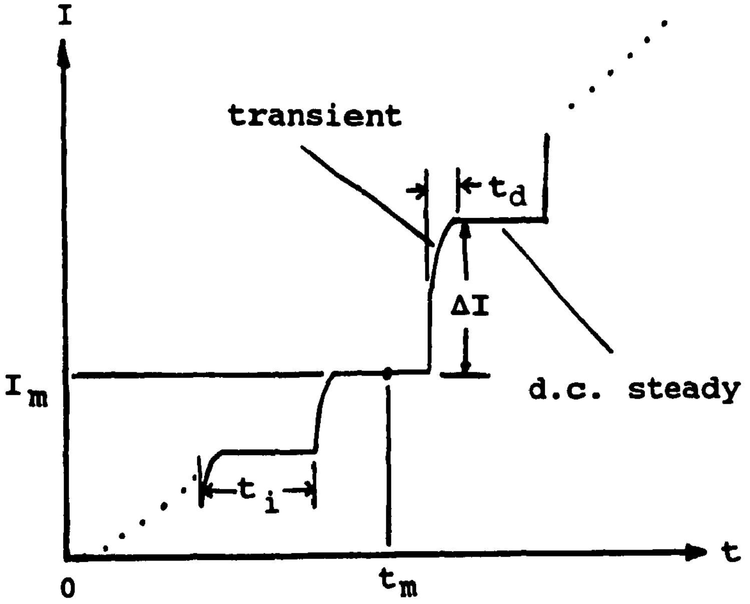

$t_i >> t_d$

fig.4.4 Current response in time for a diode

fig.4.5 Cryostat for low T-dependent I-V measurement

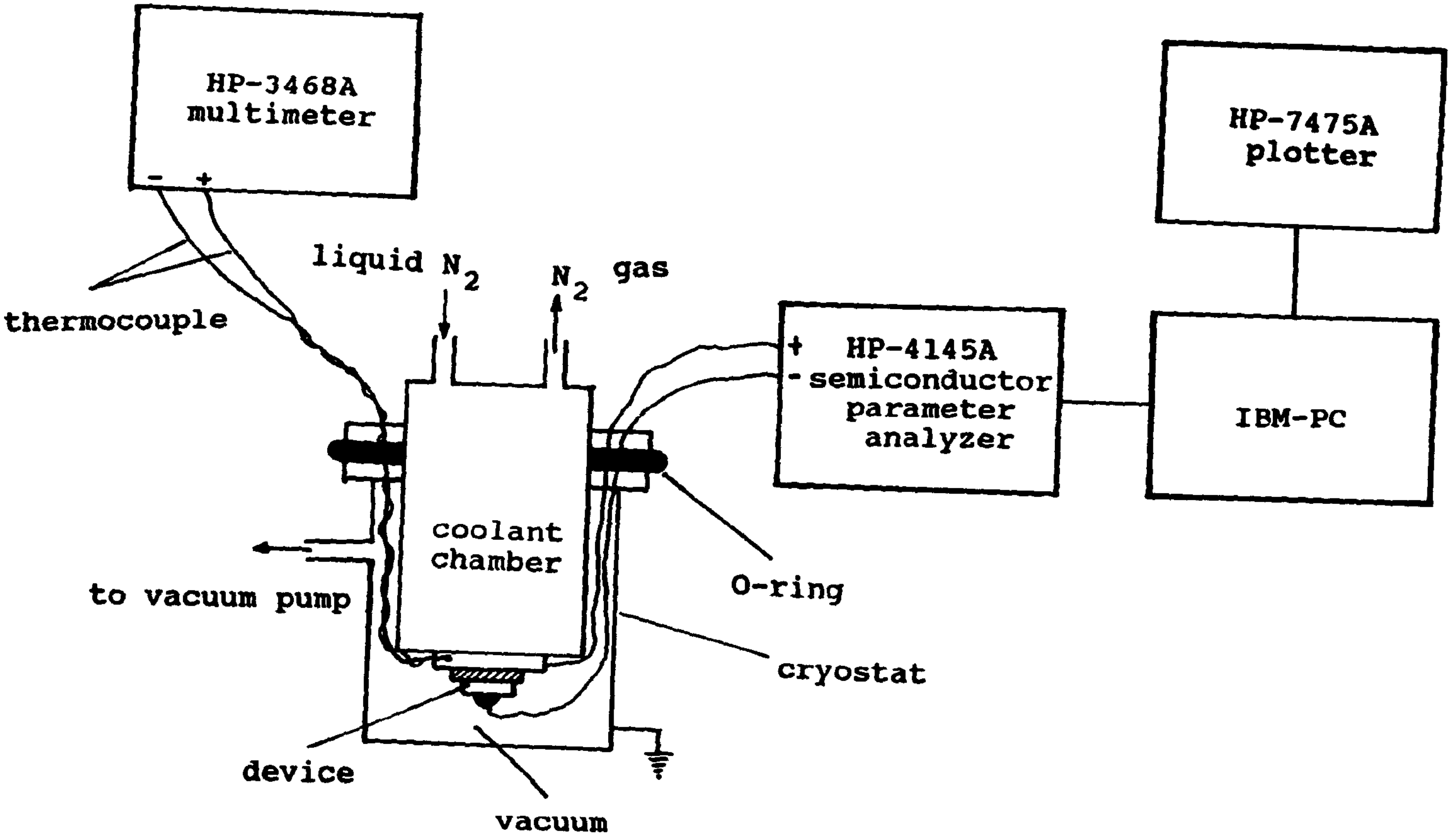

fig.4.6 Low T-dependent I-V measurement system

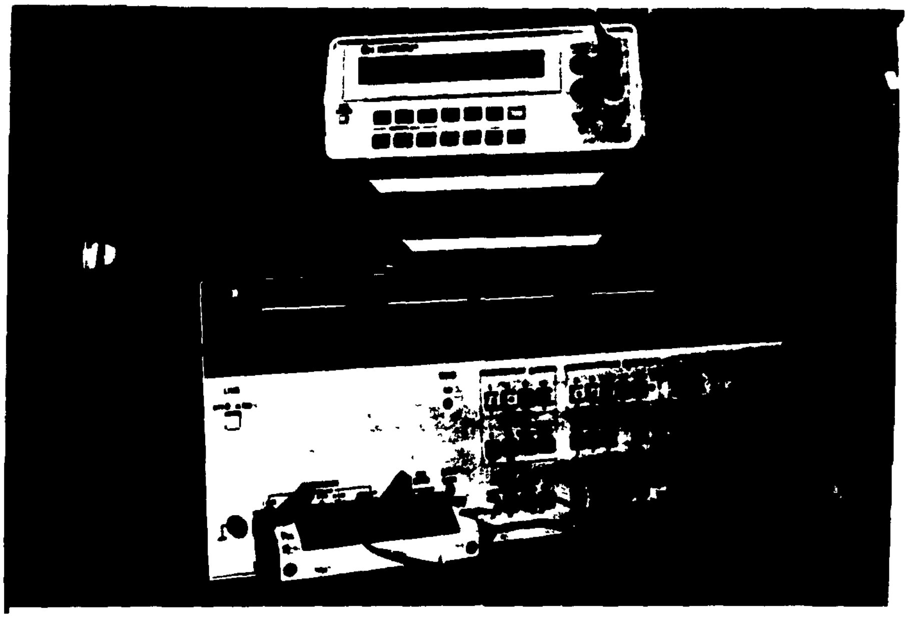

fig.4.7 HP-4274A multi-frequency LCR meter

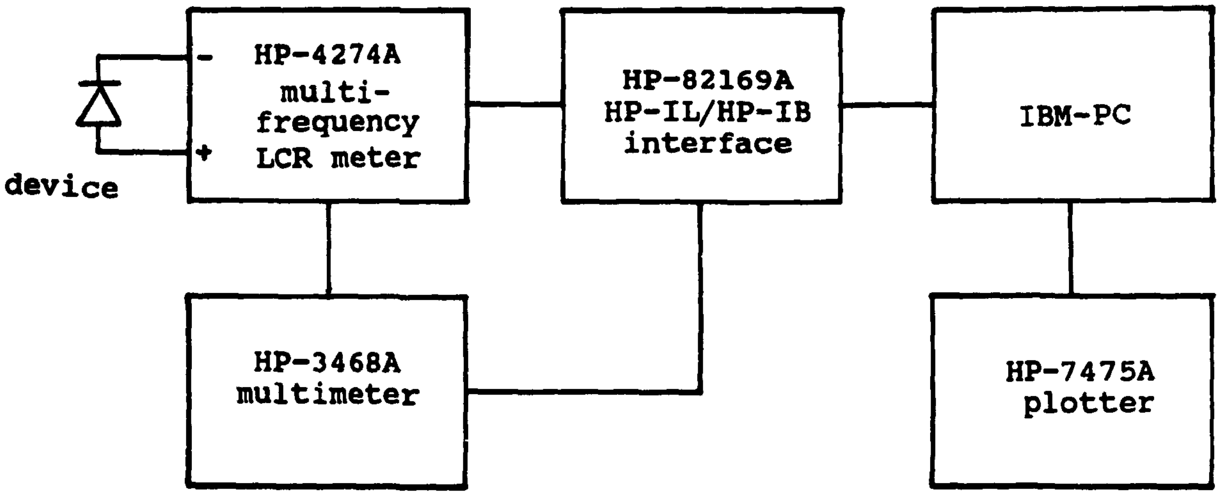

fig.4.8 Frequency-dependent C-V measurement system

Chapter 5

Results & Interpretations

5.1 Current Characteristics

5.1.1 General Observations

Figs. 5.1 to 5.7 show the I/V characteristics of several devices whose surfaces were prepared by the abrasive polishing (AP1 to AP3), $K_2Cr_2O_7$ + H_2SO_4 etching (KCO1, KCO1R & KCO2) and HCl + HNO_3 etching (HH1 & HH2) methods. The Al areas are either $9.62\mathrm{x}10^{-2}\mathrm{cm}^2$ or $7.85\mathrm{x}10^{-3}\mathrm{cm}^2$ as stated in Table 3.1. All current/voltage curves are asymmetric, with the easy conduction corresponding to a more positive applied potential at the p-$CuInSe_2$ side. The best rectification at +1 V exceeds 3 decades (sample HH1 in fig.5.6). The reverse currents do not saturate and breakdown voltages as small as -2 V have been noticed for some as-fabricated diodes. They typically increase by a decade from -3kT/q to -1 V. For forward V > 3kT/q, the currents increase exponentially with an n value (ideality factor) rate ranging from 2 to 4 at 298° K. Shorter linear regions and larger n values were consistently observed for the abrasively polished samples as compared with the chemically etched ones. The forward log(I)/V plot of diode AP1 (fig.5.1(a)) is entirely non-linear. The linear I/V plot in fig.5.1(b) indicates that I rises linearly with V for V > 0.7 V. The 1/slope of the asymptote gives a series resistance R of 2140 ohm for this sample. Thus the non-linearity in the log(I)/V plot for V << 0.7 V is rather due to an increasing n with V which characterizes the actual carrier flow across the junction than to the limitation of R.

Diode AP3 (fig.5.3) has 6 evaporated Al areas on the same substrate. However n, I_o and R ($\Delta V/I$) appear to be surface dependent. The scatter of I_o is about 1 order of magnitude. The ratio of R_{max} to R_{min} is about 2. If R is due to the p-$CuInSe_2$ bulk region, this implies a non-uniform transverse doping, assuming constant mobility and longitudinal doping. Diode KC01R (fig.5.4) is the reproduced version of KC01 using the same substrate which has been annealed in air at 230°C for 65 min. (Table 3.1). The I_o value of KC01 is about 5 times that of KC01R. The current of KC01 is always greater than the KC01R's at any bias, but it is the opposite for rectification. Their n values are almost identical. The apparent R ratio of KC01R to KC01 is about 7, despite that the same surface region has been used each time for Al evaporation. This seems to contradict that the semiconductor is the source of R. This will be discussed later in section 5.2.5. In general, the reverse saturation current density I_o/A covers a set of values within a factor of 10 among the samples under each surface method. The correlation between these three I_o/A ranges and the respective methods is not strong. From figs.5.1(c), 5.5 and 5.7, one sees that I_o increases whereas n and R decrease with T. The temperature-dependence of R likely arises from a series scattering mechanism in the quasi-neutral region of p-$CuInSe_2$. The currents are very unstable at low temperature and small bias (longer voltage integration time should be used). But the mean values seem to increase with V continuously. Two linear regions can be distinguished at low temperatures with the lower bias one having a smaller slope. Fig.5.8 plots n vs. 1/T (upper bias n values used for low T). The nT products for diodes KC02 and HH2 are apparently constant w.r.t. temperature, suggesting that field emission (E_{oo} = nkT) may be effective. If this is true, our p-$CuInSe_2$ must be degenerate, i.e., the hole concentration $p = N_A > N_v$. We are going to check this.

5.1.2 Estimates of N_v, m* & A* for p-$CuInSe_2$

N_v, m* and A* for p-$CuInSe_2$ have not been reported in the literature. Assuming $N_v = N_c$, $N_i = 9.11 \times 10^9$ cm^{-3}[1.4], E_g = 1.01 eV, then just at hole degeneracy, $E_{fs} = E_v$ so that

$$p = N_v = N_i \exp(E_g/2kT) \qquad (5.1)$$

From eqn. (5.1), N_v at 298°K is 3.11×10^{18} cm^{-3}. m* (for holes) can now be obtained from [2.11]

$$N_v = 2(2\pi m^*kT/h^2)^{3/2} \qquad (5.2)$$

and its value is $0.25m_o = 2.7 \times 10^{-31}$kg. Since A* is proportional to m* and A* = 120 A-cm^{-2}-°K^{-2} for $m^* = m_o$, A* for p-$CuInSe_2$ is 30 A-cm^{-2}-°K^{-2} (c.f. A** = 32 A-cm^{-2}-°K^{-2} for p-Si [1.4]).

5.1.3 Interface Effects on Ideality Factor n

The n value reflects the transport process if it is the only dominant one among others. The ideal thermionic emission is obviously absent in our diodes. Recombination is not dominant since n is always greater than 2 at 298°K and increases as T decreases. Field emission is unlikely because the E_{oo} values (> 53 meV) from the constant log(I)/V slopes lead to N_A values of the order $10^{19}cm^{-3}$ by (eqn. (2.18)), which is much larger than those from the C^{-2}/V slopes and Hall effect measurements. Card and Rhoderick [5.1] have studied the effects of thermally-grown interfacial SiO_2 and surface states on the d.c. characteristics of Au/n-Si diodes. They concluded that a large surface state density D_{sb} in equilibrium with Si was responsible for some observed large n values. Fig.5.9 shows the band structure of an MIS contact (p-s.c. for our case) under a forward bias V, which is split between the electrostatic potential drops of the insulator and the semiconductor such that

$$V = (V_{do} - V_d) + (V_{io} - V_i) \tag{5.3}$$

where 'o' represents zero bias. The barrier height is evidently

$$\phi_b = V_d + \xi + V \tag{5.4}$$

Differentiating eqns.(5.3) and (5.4) w.r.t. V, one obtains

$$\beta + 1/n = 1 \tag{5.5}$$

$$d\phi_b/dV = \beta \tag{5.6}$$

where $1/n = -dV_d/dV$ (5.7)

$\beta = -dV_i/dV$ (5.8)

and $0 < \beta \, , \, 1/n < 1$ (5.9)

In integral form, eqns. (5.6), (5.7) and (5.8) are respectively equivalent to

$$\phi_b(V) = \phi_{bo} + \int_0^V \beta(V^*)dV^* \tag{5.10}$$

$$V_d(V) = V_{do} - \int_0^V dV^*/n(V^*) \tag{5.11}$$

$$V_i(V) = V_{io} - \int_0^V \beta(V^*)dV^* \tag{5.12}$$

We shall see in section 5.1.4 that the n defined by eqn. (5.7) is just the usual one in the I/V relation. However eqn. (5.7) is also valid for reverse bias. Surface states can be classified into 2 groups: one of density D_{sa} equilibrates with the metal, the other of density D_{sb} with the semiconductor. D_{sa} and D_{sb} are functions of energy E in the band gap and δ. At a fixed E, $D_{sa} + D_{sb}$ is constant w.r.t. δ. Using Gauss' law, charge neutrality and the above potential distribution relations, Card and Rhoderick [5.1] derived the dependence of n on the interface parameters as

$$n = 1 + \frac{(\delta/\varepsilon_i)(\varepsilon_s/W + qD_{sb})}{1 + (\delta/\varepsilon_i)\, qD_{sa}} \tag{5.13}$$

One limiting case, best applicable to our devices with large n values, is $D_{sb} >> D_{sa}$. This means the interface states communicate with the semiconductor more readily than with the metal due to the presence of a thick interfacial layer. Then eqn. (5.13) becomes

$$n = 1 + (\delta/\varepsilon_i)(\varepsilon_s/W + qD_{sb}) \qquad (5.14)$$

The role of the insulator is to reduce the dependence of V_d on V, i.e., n > 1. Another effect is the bias dependence of ϕ_b. Both V_i and V_d decrease while ϕ_b increases with V (fig.5.10). The fact that n is large for our diodes is equivalent to a weak dependence of V_d or strong dependences of V_i and ϕ_b on V.

5.1.4 Forward Hole Tunnel Current I_p

There are 2 modifications to the hot emission of holes from the semiconductor to the metal described by eqn. (2.15). First, the insulator attenuates the tunneling transparency by a factor of $\exp(-\chi_i^{1/2}\delta)$, where χ_i is the difference between the E_v's of the insulator and the semiconductor at the interface. The dimension of the exponent is $eV^{1/2}$-Å. Second, ϕ_b is now V-dependent. Using eqns. (5.5) and (5.10), the hole tunnel current, for V > 3kT/q, is

$$I_p = AA^*T^2 \exp(-\chi_i^{1/2}\delta)\exp(\frac{-q\phi_{bo}}{kT})\exp(\frac{q}{kT}\int_0^V \frac{dV^*}{n(V^*)}) \qquad (5.15)$$

This component is shown in fig.5.9. I_{ss} is the net electron tunnel current into the interface states, in series with the recombination (between states and conduction/valence bands) currents U_n and U_p, i.e., $I_{ss} = U_p - U_n$. Charge transfers among the states (Q_{ss}), metal (Q_m) and semiconductor (Q_d) are carried by I_{ss}, U_p and U_n. If I_p dominates over all others, the deviation of n from 1 results mainly from interface effects and we shall assume this. Actually Schottky effect would also lead to a bias dependent ϕ_b, but it practically cannot depart n from 1 as much as here. The n(V) value can be determined from the slope(V) of the $\ln(I_p)/V$ plot (not necessarily linear) as

$$n(V) = \frac{q}{kT}\frac{dV}{d\ln(I_p)} \qquad V > 3kT/q \qquad (5.16)$$

A** is not used in eqn. (5.15) because reflection above and tunneling below the Schottky barrier are not included. If the transmission coefficient is ignored, then the usual 298°K log (I)/V intercept would overestimate ϕ_{bo} significantly for thick δ or large χ_1. The attainment of ϕ_{bo} requires that the uncertainty in $\chi_1^{1/2}\delta$ be removed. The temperature-dependence method can achieve that.

5.1.5 ϕ_{bo}, χ_s & Insulator Transmission Coefficient

Fig.5.11 plots $\log(I_o/T^2)$ vs. 1/T. The log(I)/V plots of diode AP1 (fig.5.1(c)) are too non-linear to obtain I_o and n unless below 243°K. It can be seen that $I_o \propto T^2 \exp(-E_a/kT)$, descriptive of eqn. (5.15), at high temperature. The ϕ_{bo} (E_a/q) values from the slopes are rather small. This indicates a thick δ and consequently a large potential drop V_{io} across the insulator at zero bias since (fig.5.9)

$$\phi_b(V) = (E_g/q + \chi_s - \Phi_m) - V_i(V) \tag{5.17}$$

From eqn. (5.17), the estimated lower bounds (neglecting V_{io})of χ_s are 3.31, 3.42 and 3.51 eV for diodes AP1, KCO2 and HH2 respectively where Φ_m of Al is 4.17 eV. The $\chi_i^{1/2}\delta$ values from the I_o/T^2 intercept ($A^* = 30$ A-cm^2-^{o}K^{-2}), are large compared with the maximum of 10 eV$^{1/2}$Å for the thickest (26 Å) SiO_2 diode reported by Card and Rhoderick [5.1]. So a thick δ again or a large insulator barrier χ_i is seemingly possible. All these implications are consistent with the fact that n is large upon examining eqn. (5.14).

So far we have assumed $I = I_p$, due to interface effects. But neither eqn. (5.13) nor (5.14) can explain the temperature-dependence of n here. The plots in fig.5.11 are not quite linear at low temperature. This has to be related to the excess current ΔI at small forward voltages and low temperature (figs. 5.1(c), 5.5 and 5.7). Thermionic-field emission is believed to be the cause since 1) our substrates are moderately doped, 2) at smaller forward voltages and lower temperature, the upper part of the Schottky barrier is thinner for the colder holes to tunnel through, 3) this process can explain the fast rise in n at lower temperature. The fact that our Schottky junctions near the sharp Al perimeters are not guarded is in favour of the process since the crowding of field lines there enhances the tunnel probability. This edge effect, together with the interface effects which cause a reduction in ϕ_b with reverse bias, are sufficient to account for the soft reverse behaviour of our diodes. The limitation of I_{ss} on I_p at low temperature is also worth considering. Nevertheless, it is still convinced that emission over the Schottky barrier modified by interface effects is dominant at 298°K. Otherwise any attempt to obtain ϕ_b for any Schottky diode from the I/V method is meaningless.

5.2 Suface State Energy Distribution

Walker [5.2] has determined the surface state densities in tunnel MOSi diodes using eqns. (5.14) and (5.16). He assumed all the interface states were in equilibrium with S_1 so that the Fermi level at the surface, which determined their population, was pinned to the bulk Fermi level. A similar method has been tried here to obtain the $D_{sb}(E)$ profiles for our p-$CuInSe_2$ surfaces. However there are two changes. First, the ε_s/W term in eqn. (5.14) has been neglected, i.e.,

$$D_{sb}(V) = [n(V)-1]\varepsilon_1/q\delta \ \mathrm{cm}^{-2}\mathrm{V}^{-1} \qquad (5.18)$$

since W ($\propto V_d^{1/2}$) changes slowly with V (large n) and it would not deviate much from the minimum value obtained by the C^{-2}/V method, assuming depletion approximation ($W = A\varepsilon_s/C$). This will be justified later because the calculated qD_{sb} values exceed the maximum ε_s/W values by 1 to 2 orders of magnitude. The second change is that n has been defined for $V > 3kT/q$ according to eqn. (5.16), instead of from zero bias as Walker did. eqn. (5.18) is voltage-dependent, meaning that D_{sb}, being evaluated at E_{fs}, will vary (unless uniform) when E_{fs} moves down w.r.t. the surface state levels as V increases. This is why n may or may not be constant over certain V intervals. If we define $E = E_{fs} - E_v$ (x = 0) (fig.5.9), then

$$E(V) = V_d(V) + \xi \qquad (5.19)$$

and $$dE = dV_d = -dV/n(V) \qquad \text{from (5.7)} \qquad (5.20)$$

So by piecewise-linearly integrating eqn. (5.20), $D_{sb}(E)$ can be obtained using eqn. (5.18). The starting limit E(3kT/q) is unknown because n is unattainable for $0 < V < 3kT/q$. It is reasonable to assume that $E(3kT/q) \cong E(0) = \phi_{bo}$ since $\Delta V_d << \phi_{bo}$ for thick δ. There are still two unknowns, ε_i and δ. Since our substrates were not cleaved in ultra-high-vacuum, an interfacial insulating layer should be inevitable during the surface processing which always involved chemical reactions and so contaminations. The causes and natures of the insulators under our three surface preparation methods are not clear. Since linear and non-linear C^{-2}/V curves have been observed under each method, we can merely argue that δ do not differ significantly. A δ value of 30 Å (just thick enough for all surface states to equilibrate with Si) was used in each case in view of the work on thermal equilibrium statistics by Card and Rhoderick later [5.3]. The insulator permittivities, ε_i were assumed to be ε_o, leading to a lower bound estimate for D_{sb}. Before obtaining n(V) from the log(I)/V plots, one should correct for series R. The best estimate of R is the $\lim_{I \to \infty} \frac{dV}{dI}$ from the linear I/V plot. Unfortunately the

+1 V range we have used so far is not sufficient to produce any well defined linear region in most cases. The $\Delta V/I$ value from the log(I)/V plot is sometimes an overestimate because non-linearity may also be a result of non-uniform $D_{sb}(E)$. Anyway all we could do was recursively fitting the (V,I) points into eqn. (2.27) under the constraint that V - IR should always increase with I. Fig. 5.12 shows the curves at 298°K before and after correcting R. One sees that n increases with V in the post-linear region. The corrected curve for diode AP1 is essentially the same as that in fig.5.1(a) for $V < 0.3$ V where R is 2140 ohm from fig.5.1(b).

Table 5.1 tabulates the integration steps for the curve in fig.5.1(a) until 0.3 V and the R-corrected curves in fig.5.12. Fig.5.13 plots D_{sb} vs. E in a portion of the lower half gap. It can be seen that for all surface preparation methods, D_{sb} has a tendency to increase towards E_v while remains flat towards the mid gap. The results of Walker on n-Si surfaces have similar behaviour in the upper half gap, though the magnitude of D_{sb} is an order larger there. The fact that constancy in D_{sb} is not seen for diode AP1 is only a limitation of the log(I)/V method to deduce n for $V < 3kT/q$, corresponding to larger V_d or E. Diodes AP2 and AP3, all with abrasively polished surfaces, have a constant n for small bias, suggesting that D_{sb} should indeed be uniform for E greater than a specific value. However that appearance may shift along the E-axis from sample to sample, and from one surface preparation method to the other. The n values for the same substrate AP3 are scattered from 2.8 to 4.04 over the surface. This suggests that the surface states by abrasive polishing do not vary in energy only, but in space also. Fig.5.13 shows that diode AP1 has the largest D_{sb} compared with those of KCO2 and HH2. This is consistent with the observation that all other AP samples have relatively larger n values at 298°K than the etched samples. Thus it is concluded that the abrasive polishing method has produced more surface defects per unit area than the other two chemical etching ones, under the basis of eqn. (5.18).

5.3 Differential Capacitance Characteristics

5.3.1 General Observations

The C'^{-2}/V curves of a few Al/p-$CuInSe_2$ diodes are shown in figs. 5.14 to 5.20. The devices were prepared by the abrasive polishing (AP1 to AP3), $K_2Cr_2O_7$ + H_2SO_4 etching (KCO1R & KCO2) and HCl + HNO_3 etching (HH1 & HH2) surface methods respectively. C' denotes the apparent capacitance as seen by the LCR meter. Several remarks emerge from those figs.: 1) they are all frequency-dependent, 2) some are linear while others are not, 3) C'^{-2} increases with frequency at any fixed V, 4) C'^{-2} generally decreases with V at a fixed frequency either linearly or concavely, 5) minima in C'^{-2} occur for some diodes (AP1, AP2, KCO1R & HH1) in the reverse region at high frequency. The last is rather odd since even if interface effects or deep traps exist, the junction capacitance C ought to increase monotonically with V at any frequency when the semiconductor surface is depleted. For those curves varying concavely with V, one may think of an increasing acceptor density towards the surface. This is not true since the substrate faces for Al deposition were randomly chosen. So statistically we might have deposited Al on the opposite faces for some samples such that the acceptor density would have decreased towards the junction and the C'^{-2}/V curves now would have gone down convexly instead. But this has never been seen. Non-uniform doping along the x-direction (perpendicular to the surface) is therefore unlikely. However small fluctuations may be present but it cannot account for such a rapid fall in slope with V. As seen from figs.5.16 and 5.20, the C'^{-2}/V curves are linear with the slopes and the V-intercepts different at the same frequency for different Al contacts on the same substrate. This is believed to be due to the transverse variations of some bulk or surface properties resulted from the material or surface preparations. The changes of the V-intercepts with frequency in KCO2 (fig.5.18) and HH2 are less than those in AP3 for a given Al contact. Referring to the C'^{-2} minima, this is certainly not an inherent a.c. behaviour of the junction, but rather due to the series effect of an electrical element or circuit outside the Schottky barrier.

5.3.2 Series R Effect on Capacitance Measurement

Goodman [5.4] was the first one ever who studied theoretically the capacitance of a Schottky barrier with series resistance. He modelled the diode under a.c. conditions by the circuit shown in fig.5.21(a), where C_d and G , the depletion capacitance and differential conductance respectively, are given by

$C_d^{-2} = 2(V_{do} - V)/A^2Nq\varepsilon_s$ (-kT/q omitted) (5.21)

$G = dI/dV = q(I + I_o)/kT$ ideal emission (5.22)

The equivalent capacitance C' (fig.5.21(c)) as measured by the a.c. bridge is related to C_d by

$$C' = C_d/(1 + \omega^2R^2C_d^{\,2}) \quad (5.23)$$

if RG << 1 (before reverse breakdown). Goodman further assumed that $\omega^2R^2C_d^{\,2} << 1$ so that to a first order approximation, eqn. (5.23) simplifies to

$$C'^{-2} = C_d^{-2} + 2\omega^2 R^2 \quad (5.24)$$

From (5.24), the C'^{-2} /V curve is still linear with a slope corresponding to the dopant density N, but the V-intercept exceeds V_{do} somewhat. Actually, C' is defined at V while C_d is defined at V' = V - IR (fig.5.21(d), but for small bias values, IR can be ignored. In other words, RG << 1 <=> RdI << dV. The effect of R on capacitance has rarely been reported after Goodman, especially at high frequency where $\omega^2R^2C_d^{\,2} << 1$ is not satisfied. Yet most discrete semiconductor diodes are composed of single crystals so bulky that a moderate doping would yield an appreciable R.

In the present study, Goodman's model was extended to 1) discard the limitation of $\omega^2R^2C_d^{\,2} << 1$ and 2) replace the ideal $C_d(V)$ by the more realistic C(f,V) (fig.5.21(b)) if interface and trap effects are present, in hope of an explanation for the C'^{-2} minima in our results. Under our changes, eqn. (5.23) is still valid as long as RG << 1. It can be rewritten, with C instead of C_d, as

$$C'^{-2} = C^{-2} + 2\omega^2R^2 + \omega^4R^4C^2 \tag{5.25}$$

Differentiating eqn. (5.25) w.r.t. V and bearing in mind that $dC/dV > 0$ (depletion), the C'^{-2} minima occur when $dC'^{-2}/dV = 0$ or

$$C^{-2} = \omega^2R^2 \tag{5.26}$$

and

$$C'^{-2}_{min} = 4\omega^2R^2 \tag{5.27}$$

Fig.5.22 is a graphical interpretation. C'^{-2} is comprised of the three terms on the RHS of eqn. (5.25). Note that C^{-2} need not be a linear function of V and it is generally frequency-dependent, so the figure refers to a particular frequency only. The minimum occurs when the C^{-2}/V curve intersects with the $\omega^4R^4C^2/V$ one and the voltage V_{min} where they meet is a function of frequency and R. For very small fR product, V_{min} lies deep in the forward region while for large fR product, it lies in the reverse region. C'^{-2}_{min} is useful to infer R and to extract the buried C(f,V). Eqn. (5.25) can be rewritten as

$$(C^{-2})^2 + (2\omega^2R^2 - C'^{-2})C^{-2} + \omega^4R^4 = 0 \tag{5.28}$$

Solving the quadratic eqn. (5.28) for C^{-2}, we have

$$C^{-2} = \frac{(C'^{-2} - 2\,\omega^2 R^2) \pm \sqrt{C'^{-2}(C'^{-2} - 4\,\omega^2 R^2)}}{2} \qquad (5.29)$$

The choice of ± signs in eqn. (5.29) requires some thought. From fig.5.22, one sees that for each $C'^{-2} > C'^{-2}_{min}$, there corresponds two C^{-2} roots, the larger one on the left side and the smaller one on the right side of the valley. So for $V < V_{min}$, + sign is applicable, while for $V > V_{min}$, - sign shoud be used. By doing so, C^{-2} would decrease with V which should be the case for a depleted semiconductor surface. If it happens that no minimum exists on the lower frequency curves (forward bias is not large enough), + sign should always be used. In order to verify our model, a Motorola 1N74 Si Zener diode (p-n homo-junction with Zener breakdown) with various discrete resistors added seriesly were tested. Fig.5.23 shows the I-V characteristics of the diode without R added. The internal R of the diode has almost no effect on the current over that bias range. Fig.5.24(a) shows the C^{-2}/V curve with $R = 0$. It may not be very linear (not one-sided or not uniformly doped), but is frequency-independent for $f \leq 100$ kHz, so trap effect must be absent at least for $V > -1$ V. Figs. 5.24(b) to (e) are the plots with R = 6.9, 8.3, 10 as well as 22 kohm respectively. For low frequency and small R, the simpler Goodman's model applies and the small vertical shift is $2\,\omega^2R^2$. However when $\omega^4R^4C^2$ is comparable with C^{-2}, a C'^{-2} valley is formed. Table 5.2 depicts the minima data, from which two expected facts are evident: 1) $C'^{-2}_{min} = 4C^{-2}(V_{min}) = 4\omega^2R^2$ and 2) V_{min} displaces towards the reverse region as frequency or R increases. The remaining task is to see if the R effect is correctable by eqn. (5.29). Fig.5.25 is the corrected curve of that in fig.5.24(c) which has been masked by R = 8.3 kohm. We see that this is an exact duplicate of the original C^{-2} without R in fig.5.24(a). So our extended Goodman's model is justifiable.

Table 5.3 shows the calculated R, the resistivity and the effective acceptor density N_A from the observed C'^{-2}_{min} using eqn. (5.27), supposing complete contribution of R from the p-$CuInSe_2$ quasi-neutral region whose length(V) >> W(V), is essentially equal to the crystal's L. The apparent N_A values are smaller than the average concentration of $4x10^{16}cm^{-3}$ for the as-grown samples from Hall effect measurements. But it must be remembered that most diodes have undergone an air annealing at 230°C after fabrication that might lead to elemental interdiffusion between the p-$CuInSe_2$ and Al. We shall come to this in section 5.2.5. A typical R-corrected C^{-2}/V curve using eqn. (5.29) is shown in fig.5.26 for diode AP1 where R(100 kHz) = 2080 ohm. Comparing with fig.5.14, we see that for $f \lesssim 20$ kHz, $C' \cong C$. This is the case where $\omega^2R^2C^2 << 1$. The correction is not very effective for $V > V_{min}$(100 kHz) regarding the behaviour of C^{-2} and for this reason some lower frequency curves have to be chopped after that point. For that sample, C'^{-2}_{min} is not absolutely proportional to f^2 for a fixed R. There can be only 2 causes for this in general: 1) $RG \not\ll 1$ for $V > V_{min}$ so that eqn. (5.23) is not valid in the first place or 2) the circuit model in fig. 5.21(b) is over-simplified, i.e., the series effect may also be capacitive due to ohmic contacts with poor a.c. performance. Since our biases are small in magnitude, 2) is more probable. Nevertheless the 2080 ohm from the C'^{-2}_{min} (100 kHz) is still comparable to the 2140 ohm from the I/V plot (fig.5.1(b)). These R values are surprisingly large in view of our as-grown resistivities and substrate dimensions. In any case, the corrected curve is a good approximate of the actual C^{-2}/V characteristics deep on the left side of the C'^{-2} valley. Fig. 5.26 indicates that C^{-2} is still frequency-dependent and non-linear in V. This is also true for the other corrected curves. For diodes AP3, KCO2 and HH2, the C'^{-2}/V plots are rather linear and no minimum exists over those bias ranges. Hence C and C' are simply related by the Goodman's model and their difference is negligible in practice. The apparent N_A values from the slopes using eqn. (2.33) for diode AP3 are 4.6, 2.2, $2.1\times10^{16}cm^{-3}$ for the equi-area contacts B, C, E respectively. The R values from the log(I)/V plot are 94, 180, 190 ohm in that order. The ratio of the RN_A products is 1.1 : 1 : 1. The feeling that R is due to the p-$CuInSe_2$ bulk is growing. Diode AP3, being non-heat treated, has the closest N_A values compared to the typical as-grown hole concentration from the Hall effect measurement.

A question has yet to be answered is why the C^{-2}/V plots are frequency-dependent after the removal of R or if R is insignificant. Only interface and deep trapping effects can be responsible. These two effects contribute in parallel to the total C of the Schottky barrier when their finite time constant reciprocals are significant compared with ω. Qiu and Shih [1.14] have previously reported the existence of deep levels in our p-$CuInSe_2$ material by studying the transient and thermally-stimulated capacitances of n^+-p homo-junctions. We have already proposed the presence of interfacial layer and surface states from the non-ideal I/V results for the Schottky diodes here. The addition of deep levels now would generally make capacitance analysis very difficult. Fig.5.27 shows two MIS contacts with a simple deep level at E_t from E_v, under a reverse bias V_r. Assume $E_t < E_g/2$ and the traps are acceptor-like, then their occupation is governed by the hole imref which essentially coincides with the bulk level E_{fs}. Case (a) corresponds to a thin insulator where V_d is large and depends strongly on V_r such that $V_d + \xi > E_t$. So E_{fs} crosses the deep level somewhere near the surface and the charge of the filled traps Q_t varies as V_d is altered, yielding a trap capacitance $C_t = dQ_t/dV_d$ in parallel with the depletion one C_d. The surface states are populated according to E_{fm} so that $dQ_{ss} = AqD_{sa}dV_i$. In getting the total C, we consider the charge $Q_t + Q_d$ in the semiconductor, so the deep level has a more profound impact on C than the interface states do. Case (b) corresponds to a thick insulator where V_d is small and increases weakly with V_r such that $V_d + \xi < E_t$. Hence E_{fs} will ordinarily not cut the deep level (unless V_r is extremely large) and the traps remain empty as V_d varies, giving zero Q_t and C_t. The surface states are now populated according to E_{fs} so that $dQ_{ss} = -AqD_{sb}dV_d$. In getting the resultant C , one has to consider $Q_{ss} + Q_d$, so surface states are completely dominant. Generally, the relative roles of deep level and surface states lie between the above two limits for an intermediate δ and C is very complicated. Our devices are believed to be of the type (b) from the I/V results and for the small V_r used for C measurement. Hence deep levels will be omitted hereafter for the sake of analysis.

5.3.3 Evidence of Interface Effects

Without interfacial layer, $V_i = 0$ and $V_d = V_{do} + V_r$, then eventhough surface states are present, C is simply the depletion capacitance $C_d(V_r)$, i.e.,

$$C = dQ_d/dV_r = dQ_d/dV_d = C_d \qquad (5.30)$$

which is of the same form as the ideal eqn. (2.32). Suppose now there is an interfacial layer, let us consider two cases:-

I) thin insulator

The interface states equilibrate with the metal. Change in Q_{ss} is mainly due to charge transfer between the states and the metal via tunneling (I_{ss}). The system under a.c. conditions can be modelled by the circuit in fig.5.28(a), where $C_i = A\varepsilon_i/\delta$ is the insulator geometrical capacitance, $C_s = dQ_{ss}/dV_i = AqD_{sa}$ is the surface state capacitance and $G_T = dI/dV$ is the tunneling conductance. The total C is obviously given by

$$1/C = 1/(C_i + C_s) + 1/C_d \qquad (5.31)$$

C depends on bias but not on frequency. Cowley [5.5] has obtained $C = dQ_d/dV_r$, where $dV_r = dV_d + dV_i$, as

$$C^{-2} = 2(V_I + V_r)/A^2Nq\varepsilon_s \qquad (5.32)$$

$$V_I = V_{do} + \frac{V_1^{1/2}(V_{do} - kT/q)^{1/2}}{1 + \alpha} + \frac{V_1}{4(1 + \alpha)^2} - kT/q \qquad (5.33)$$

$$V_1 = 2q\varepsilon_s N\delta^2/\varepsilon_i^2 \qquad (5.34)$$

$$\alpha = qD_{sa}\delta/\varepsilon_i \qquad (5.35)$$

So the C^{-2}/V plot is linear (only if D_{sa} is uniform as the surface state levels move down w.r.t. E_{fm} during the increment of V) with a slope corresponding to N, but the V-intercept ($V = -V_r$) V_I exceeds V_{do} somewhat. If $kT/q + \xi$ is added to V_I, one would approximately get the flat-band barrier height ϕ_b^o [2.2], in contrast with the I/V method by eqn. (5.15) which gives the smaller ϕ_{bo}.

II) thick insulator

The interface states now equilibrate with the semiconductor. Change in Q_{ss} is due to charge transfer between the states and the semiconductor bands via generation (U_n and U_p). The system would then function like the circuit in fig.5.28(b), where $C_s = dQ_{ss}/dV_d = AqD_{sb}$ and R_s are related to the finite charging/discharging time constant $\tau = R_sC_s$ of the states. C_s, R_s and τ are all dependent of the surface potential $V_d(E)$. C is now frequency-dependent. It can be shown from fig.5.28(b) easily that at:-

1) low frequency, $\omega\tau << 1$

$$1/C = 1/C_{lf} = 1/C_i + 1/(C_s + C_d) \qquad (5.36)$$

2) high frequency, $\omega\tau >> 1$

$$1/C = 1/C_{hf} = 1/C_i + 1/C_d \tag{5.37}$$

3) intermediate frequency, $\omega\tau \sim 1$

$$C_{hf} < C(f,V) < C_{lf} \tag{5.38}$$

Both C_{lf} and C_{hf} are V_r-dependent only. Case 2) corresponds to the one where the surface states cannot respond to the test signal, so C_{hf} is free of C_s. If D_{sb} is uniform over the measuring V_r range, then C_{hf} as obtained by Cowley [5.5] is

$$C_{hf}^{-2} = 2(1+\alpha)(V_I + V_r)/A^2Nq\varepsilon_s \tag{5.39}$$

$$V_I = (1+\alpha)(V_{do} - kT/q) + V_1^{1/2}(V_{do} - kT/q)^{1/2} + V_1/4(1+\alpha) \tag{5.40}$$

$$\alpha = qD_{sb}\delta/\varepsilon_i \tag{5.41}$$

The C_{hf}^{-2}/V plot is still linear, but the slope gives an underestimate of N as $N/(1+\alpha)$. The difference between V_I and V_{do} is much greater than that predicted by eqn. (5.33) for thin insulator. Fig.5.29 shows the standard MIS C/V curves of case II.

From figs. 5.18 and 5.20(a), the V_I values of diodes KCO2 and HH2 at 100 kHz are substantially larger than the ϕ_{bo} values from the I/V method. This is a first sign of the existence of an interfacial insulator between the p-$CuInSe_2$ and Al. Fig.5.30 plots C vs. V at different frequency for our diodes. The fact that C (actually G too) is frequency-dependent also tells immediately that there is indeed an interfacial layer and that most surface states communicate more easily with the p-$CuInSe_2$ than with Al (case II). This is consistent with the large n values observed from the log(I)/V curves. At any bias, less surface states can respond to the test signal as the frequency rises, so C falls. The slow increase of the C(100 kHz) with V suggests that the p-$CuInSe_2$ surfaces remain depleted over our bias ranges and that the surface potential and the depletion layer width decrease weakly with V. But at lower frequency, C increases faster with V. The values of C_i are unobtainable due to our small forward biases. At any V_r, the factors by which the C/A values fall from 10 kHz to 100 kHz are in the decreasing order: HH2, KCO2, AP3, AP1, indicating the relative attenuations of the surface state effects. This is in agreement with the observation that the relative degrees of linearity of the C^{-2}/V(100 kHz) plots are in that decreasing sequence. For our frequency ranges, it seems that $C_{hf} < C < C_{lf}$. Unfortunately, lower frequency measurements have been difficult for our diodes near the largest V_r values (dissipation factor $D > 10$) and 100 kHz was the instrument limit. The lower limits of τ for the intervals of surface state energies involved with our bias ranges are accordingly shorter than 1.6 µsec. If C_{lf} and C_{hf} are accessible, their difference will determine the functions $V_d(V)$ and $D_{sb}(V_d)$.

In the δ transition between the ends I and II, the surface states are in partial equilibrium with the metal and with the semiconductor so that $dQ_{ss} = Aq(D_{sa}dV_i - D_{sb}dV_d)$. This region is dependent of the insulator/semiconductor combination and the associated C is much more complicated.

5.4 Estimation of D_{sb} from the V-Intercept

Robinson and Wilson [1.4] have calcualted the surface state density for their metal/I-III-Se_2 diodes using eqn. (5.33) with V_I = 1.38 V and V_{do} = 0.365 V. Since V_1 is basically a small quantity for moderate N, it seems that eqn. (5.33) could not have afforded to explain the big difference between V_I and V_{do}. Their devices, like ours, should rather be of the type II instead of type I as they assumed. The apparent N_A values for diode KCO2 and HH2 contact A (figs.5.18 & 5.20(a)) using eqn. (2.33) at 100 kHz are 1.7×10^{16} and $6.9\times10^{15}cm^{-3}$ respectively. From eqn. (2.36), (E_{f_1} - E_{fs}, ξ) = (0.37 eV,0.135 V) and (0.355 eV,0.15 V), therefore $V_{do} = \phi_{bo} - \xi$ = 0.125 and 0.2 V respectively, where the ϕ_{bo} values have been obtained from fig.5.11. The corresponding V_I are 0.35 and 0.65 V. Assuming $\varepsilon_i = \varepsilon_o$ and δ = 30 Å in anology with the I/V analysis, the D_{sb} values are 3.4×10^{12} and $4.2\times10^{12}cm^{-2}eV^{-1}$ respectively using eqns.(5.34), (5.40) and (5.41). Three points must be clarified in getting D_{sb}: 1) N_A and V_I have been obtained using the highest available 100 kHz and thus we are not sure if, though hope, C^{-2} will in fact saturate at C^{-2} (100 kHz) for f > 100 kHz. Anyway it appears that V_I is fairly insensitive to frequency. The linearity of the curves at 100 kHz implies that the surface state contribution to C has been greatly reduced, if not thoroughly. 2) In eqn. (5.40), the $V_1/4(1 + \alpha)$ term has been rejected since the major difference between V_{do} and V_I is sustained in $(1 + \alpha)(V_{do} - kT/q)$. 3) It is impossible to obtain N_A and so V_1 from the slope without knowing α first, but α is just the key to attaining D_{sb}. Since we have two unknowns, namely N_A and D_{sb}, the underestimate $N_A/(1 + \alpha)$ was used for N_A instead. This could only affect $E_{fi} - E_{fs}$ and so V_{do} a little due to the weak $\ln(N_A/N_i)$ dependence on N_A. Also the effect on $V_1^{1/2}(V_{do} - kT/q)^{1/2}$ would not alter the α outcome much. The D_{sb} values obtained here are very comparable with those from the I/V method. The fact that the C-2 /V plots are linear means D_{sb} are uniform over those V_r ranges. This has already been predicted by fig.5.13 if the flat portions of the D_{sb}/E profiles for the two chemically prepared samples can be extended by increasing V_r. The C^{-2}/V(100 kHz) curve (fig.5.26) for AP1 is non-linear even in the reverse region where R correction is more reliable, avoiding the determination of D_{sb}. This may be due to short $\tau < 1.6$ µsec for the majority of surface states or non-uniform $D_{sb}(E)$ over that V_r range, thus violating the assumptions of eqn. (5.39).

5.5 Heat Treatment & Se Out-Diffusion

Figs.5.31(a) and (b) show the measured C'^{-2}/V plots after an additional air heat treatment at 230°C on diode AP1 for 15 min. and on KC01R for 45 min. respectively. Comparing with the corresponding curves before that annealing in figs. 5.14 and 5.17, one sees that although the C'^{-2} values are different, the valley-shape of the curves is maintained. An interesting change is the movement of the minimum coordinates at any frequency. Table 5.4 shows the minimum data and R estimated by eqn. (5.27). For both AP1 and KC01R, V_{min} decreases (shifts in the reverse direction) with frequency before and after the extra annealing. V_{min} decreases (since R increases) after that annealing at any frequency (except at 100 kHz for AP1). For

KC01R, $C'^{-2}_{min} \propto f^2$ before and after that annealing. Although AP1 does not satisfy eqn. (5.27) absolutely, C'^{-2}_{min} still increases with frequency. For both AP1 and KC01R, R as deduced by eqn. (5.27) increases (C'^{-2}_{min} increases) after that annealing at any frequency. AP1 does not fit eqn. (5.27) as perfectly as KC01R does because as mentioned before, the parallel capacitance of its ohmic junctions is significantly finite and our extended Goodman's model includes R only. A question raised before is concerned with the increase of R (from log(I)/V plot) by a factor of 7 from the as-fabricated KC01 (185 ohm) to the repolished KC01R (1300 ohm). It is not a surprise anymore for such a large increase in R after that air annealing at 230°C for 65 min. in view of the next 45 min. annealing, causing R to increase from 800 to 1320 ohm. Actually the 1300 ohm from the log(I)/V method over-estimates the more accurate 800 ohm from the C'^{-2}_{min} for KC01R before the extra heat treatment. It is also apparent that longer annealing times yield larger factors of increase in R. Integrating all the above with the facts that the non-heat treated AP3 has the closest N_A values and the other heat treated samples in Table 5.3 have considerably smaller N_A values compared with those of the as-grown materials, it should not be doubtful now that R indeed comes from the p-$CuInSe_2$ quasi-neutral region and that annealing has reduced the effective bulk N_A (acceptor loss) and led to a rise in R (the hole mobility might increase due to less acceptor scattering, but overall the resistivity increased). This reminds us of a similar phenomenon observed by Shahidi earlier [3.2] when he annealed the as-grown materials in vacuum at various temperature and for various times. He found that some samples converted from p- to intrinsic to n-type finally within only 10 min. at 600°C and that a low temperature of 160°C was sufficient to raise the p-resistivity by a factor of 10 after 40 min. in some occasions. He said this was due to Se (acceptor) out-diffusion. So it is not unsound at all for some of our large R > 2000 ohm values (AP1) and the drastic rises in R seen after heat treatments in air at 230°C since an air ambient is essentially Se-deficient. However no n-type transformation has occurred here because the rectification polarity preserved after all heat treatments. Shih et al. [1.12] have found that the background concentrations in the p-sides of their $CuInSe_2$ n^+ -p homo-junctions as profiled by C/V_r measurement at 100 kHz were smaller than that from Hall effect measurement by an order. They also proposed that Se has diffused out of all surfaces from the bulk during the local in-diffusion of the deposited In (donor) at 200°C in a N_2 atmosphere. Perhaps Se out-diffusion is also able to explain why heat treatment could improve the reverse characteristics of some of our as-fabricated diodes since larger N_A is usually associated with thinner W, larger leakage and earlier quantum-mechanical tunneling breakdown.

5.2.6 Apparent Doping Profiles

Figs.5.32(a) and (b) show the apparent acceptor profiles of samples AP3 and HH2 respectively near the p-$CuInSe_2$ surfaces, as obtained from the C^{-2}/V slopes at 100 kHz (figs. 5.16 and 5.20) using eqn. (2.33) and by $W = A\epsilon_s/C$ of the depletion approximation. The method is, strictly speaking, not valid when there is an interfacial layer since even though the effects of surface states can be eliminated at high enough frequency, the functions $V_d(V)$ and $W(V)$ are modified from those of a perfect MS contact. Also the N_A from eqn. (2.33) is smaller than the more accurate but undetermined one (α is unknown) from the slope of eqn. (5.39). But if these changes are delivered evenly throughout the substrates, then the profiles will still be informative in a relative and qualitative sense. This seems to be the case here since the profiles with the larger $N_A(W)$ are associated with the smaller W, characteristic of the depletion approximation. The maximum depths of the profiles were limited by tne effect of the reverse leakage on C measurement. It is seen that the transverse non-uniformities in N_A are larger than its fluctuations along the x-direction. This fact is independent of the surface preparation method but rather a bulk product of the Bridgman ingot growth.

Table 5.1 D_{sb} from forward logI/V plots at 298°K, using (5.18)

V range (V to V)	n	ΔV (mV)		$-\Delta E$ ($=\Delta V/n$) (mV)	D_{sb} ($10^{12}cm^{-2}eV^{-1}$)
3kT/q,0.1	2.52	23	diode AP1	9	2.8
0.1,0.15	3.09	50		16	3.9
0.15,0.2	3.89	50		13	5.3
0.2,0.25	5.07	50		10	7.5
0.25,0.3	6.19	50		8	9.6
3kT/q,0.15	2.3	73	diode KCO2	32	2.4*
0.15,0.2	2.36	50		21	2.5
0.2,0.25	2.63	50		19	3
0.25,0.3	2.95	50		17	3.6
0.3,0.35	3.41	50		15	4.4
0.35,0.4	3.5	50		14	4.6
0.4,0.45	3.63	50		14	4.9
3kT/q,0.2	2.15	123	diode HH2 contact A	57	2.1*
0.2,0.25	2.31	50		22	2.4
0.25,0.3	2.45	50		20	2.7
0.3,0.35	2.76	50		18	3.3
0.35,0.4	3.03	50		17	3.8
0.4,0.45	3.24	50		16	4.1
0.45,0.5	3.51	50		14	4.6

*D_{sb} is uniform for this range since n is constant

Table 5.2 C'^{-2} minimum for Zener diode with added series R

R (kohm)	f (kHz)	$\omega^2 R^2$ (nF^{-2})	V_{min} (V)	$C^{-2}(V_{min})$ (nF^{-2})	C'^{-2}_{min} (nF^{-2})
6.9	100	18.8	0	18.9	75.5
8.3	100	27.2	-0.38	27.1	108.9
10	40	6.3	> +0.2	-*	-
10	100	39.5	< -1	-	-
22	40	30.6	-0.56	30.5	122.2
22	100	191	< -1	-	-

*The minimum is outside the plotting range.

Table 5.3 Estimates of R, ρ & N_A from C'^{-2}_{min} for our p-$CuInSe_2$*

Device No.	f (kHz)	C'^{-2}_{min} (nF^{-2})	R (ohm)	ρ (ohm-cm)	N_A (cm^{-3})	Annealing time (min.)
AP1	100	6.85	2080	667	1.6×10^{14}	20
AP2	100	0.25	400	127	8.2×10^{14}	15
KCO1R	40	0.162	800	256	4.1×10^{14}	65
HH1	100	0.078	220	71	1.5×10^{15}	15

*Effective area $A = 9.62\times10^{-2} cm^2$, length $L = 0.3$ cm and hole mobility $\mu_p = 60\ cm^2V^{-1}sec^{-1}$

Table 5.4 Heat treatment effects on V_{min}, C'^{-2}_{min} & R

	f (kHz)	V_{min} (V)		C'^{-2}_{min} (nF^{-2})		R (ohm)	
diode AP1	100	-0.239[1]	-0.22[2]	6.85[1]	8.72[2]	2080[1]	2350[2]
	40	-0.143[1]	-0.15[2]	1.59[1]	2.02[2]	2500[1]	2820[2]
	20	-0.048[1]	-0.05[2]	0.54[1]	0.61[2]	2920[1]	3100[2]
	10	+0.095[1]	+0.05[2]	0.19[1]	0.21[2]	3460[1]	3640[2]
diode KCO1R	40	-0.26[3]	-0.52[4]	0.162[3]	0.44[4]	800[3]	1320[4]
	20	0[3]	-0.3[4]	0.042[3]	0.11[4]	810[3]	1320[4]
	10	> +0.2[3]	0[4]	< 0.016[3]	0.027[4]	-[5]	1310[4]
	4	> +0.2[3]	> 0.2[4]	< 0.006[3]	< 0.01[4]	-	-

[1] After 20 min. air heat treatment at 230° C (fig.5.14).

[2] After 15 min. more air heat treatment at 230° C (fig.5.31(a)).

[3] After 65 min. air heat treatment at 230° C since the fabrication of KCO1 3 days ago (fig.5.17).

[4] After 45 min. more air heat treatment at 230° C (fig.5.31(b)).

[5] The minimum is outside the plotting range.

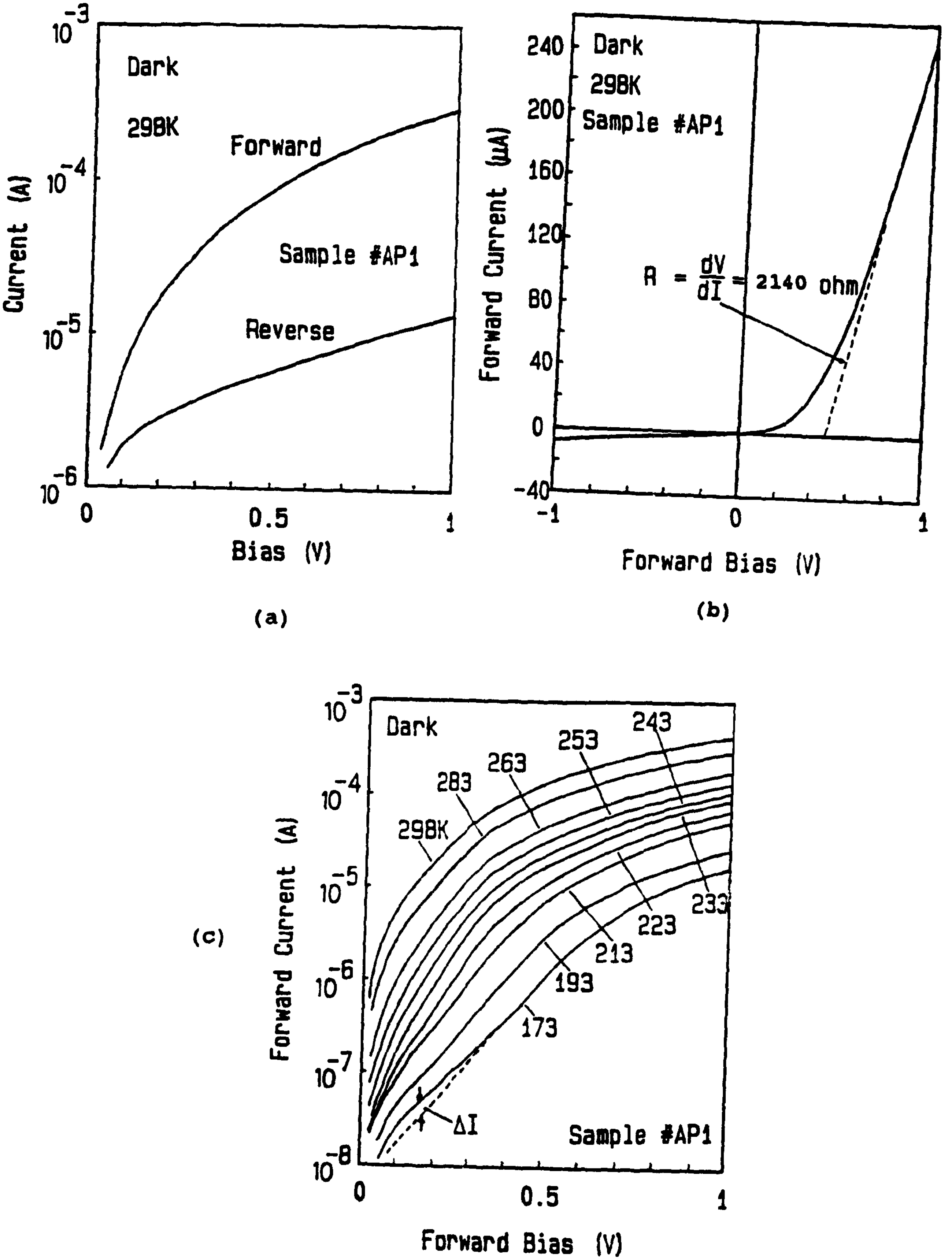

(a)

(b)

(c)

fig.5.1 I/V characteristics of diode AP1 (a) logI/V plot (b) linear I/V plot (c) forward T-dependence

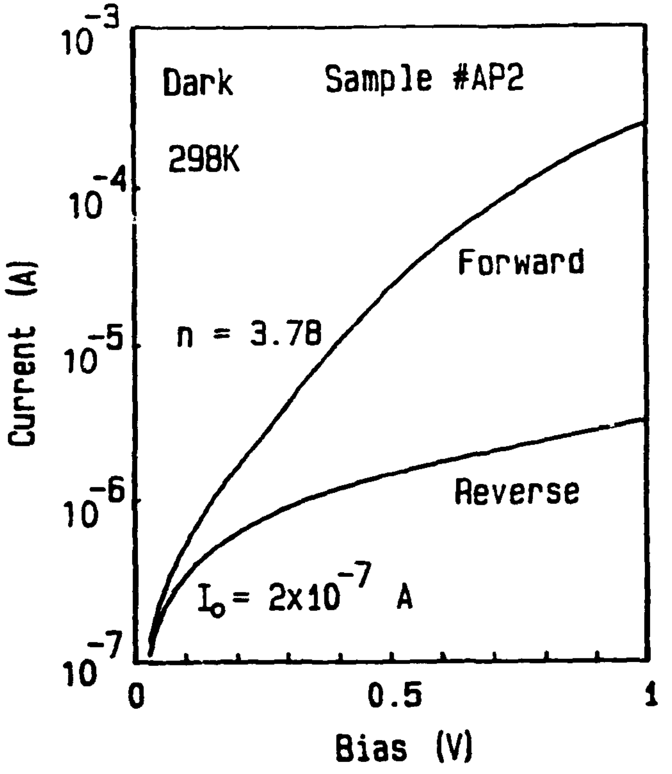

fig.5.2 LogI/V plot for diode AP2

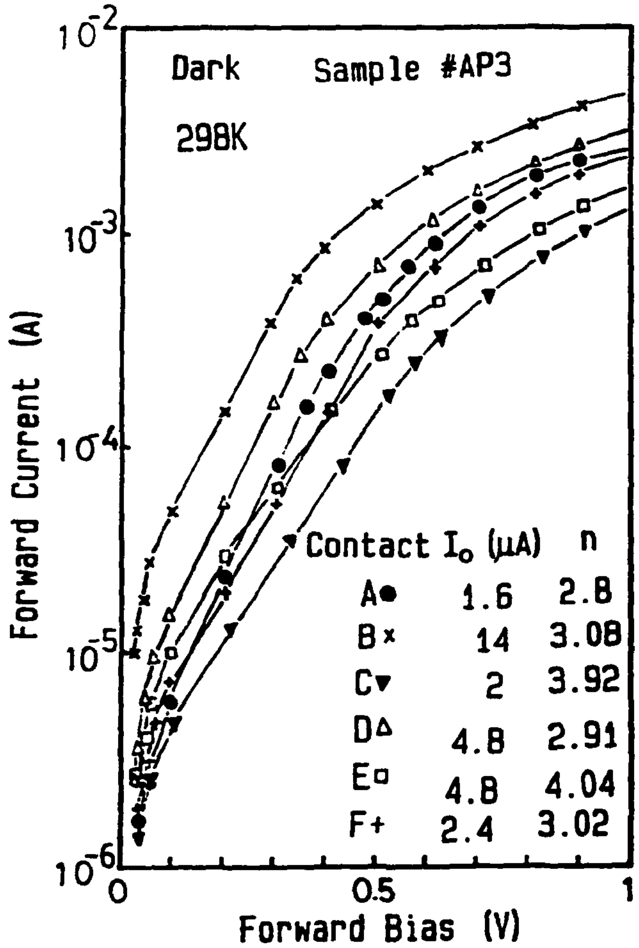

fig.5.3 Forward logI/V plot for diode AP3 with 6 Al contacts. Apparent series R: contact A, B, C, D, E, F = 150, 94, 180, 125, 190, 120 ohm.

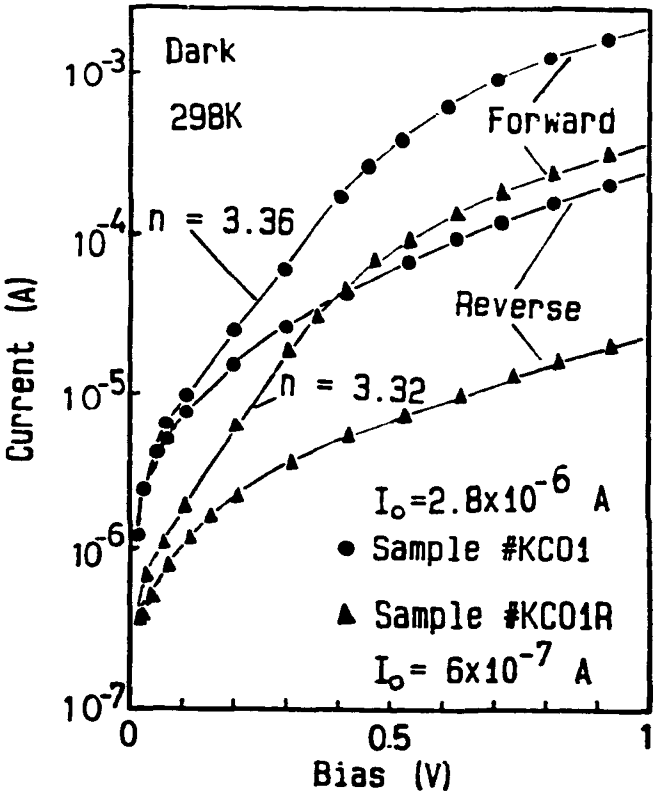

fig.5.4 LogI/V plots for diodes KC01 and KC01R (Table 3.1). Apparent series R: KC01 = 185 ohm, KC01R = 1300 ohm.

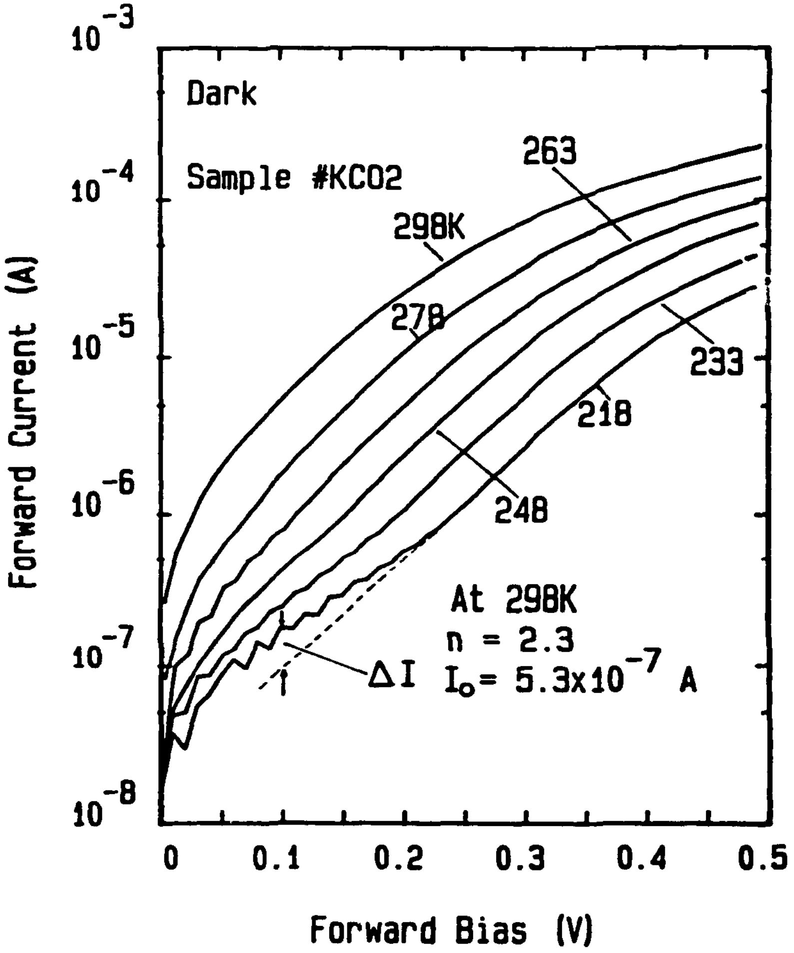

fig.5.5 Forward T-dependent logI/V plots for diode KC02

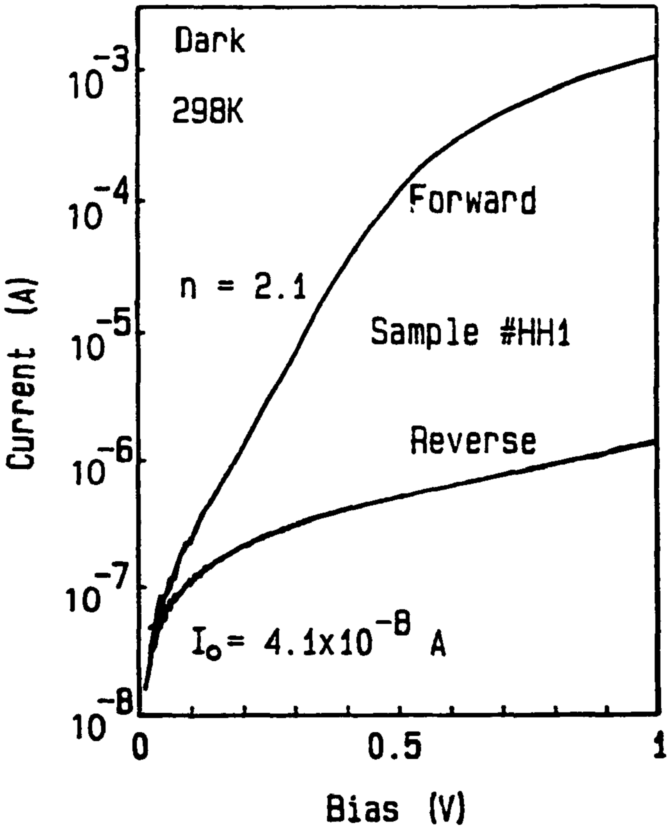

fig.5.6 LogI/V plot for diode HH1

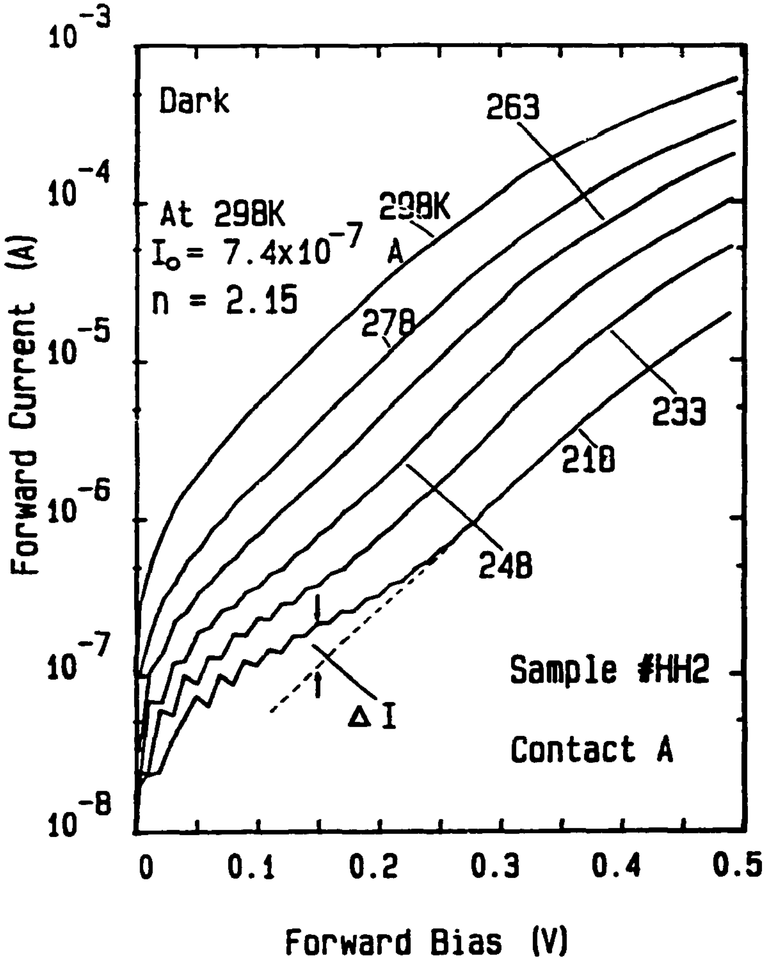

fig.5.7 Forward T-dependent logI/V plots for diode HH2, Al contact A

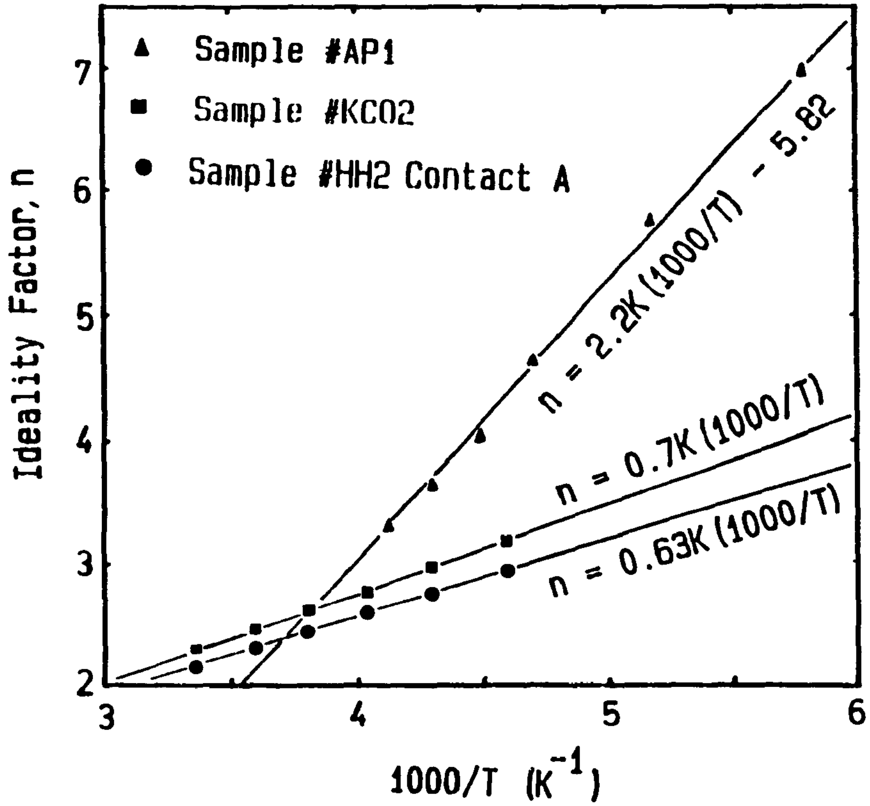

fig.5.8 Forward ideality factor n vs. 1/T

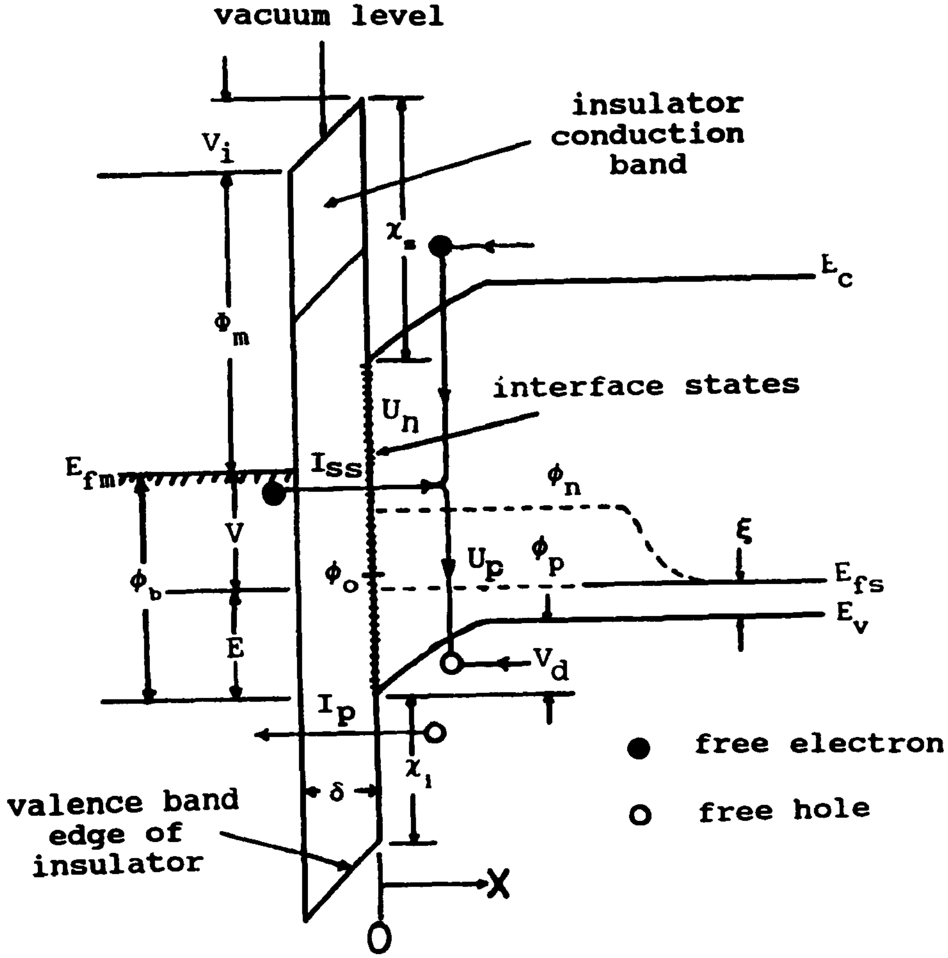

fig.5.9 Energy band diagram of a MIS(p-type) contact under a forward bias V. ϕ_p and ϕ_n are the hole and electron imrefs respectively. I_p is the emission of holes over the Schottky barrier and tunneling through the insulator into the metal. χ_i , the mean insulator barrier, is the E_v difference at x = 0. I_{ss} is the net electron tunnel flow from the metal into the interface states before recombining with the s.c. bands as the components U_p and U_n.

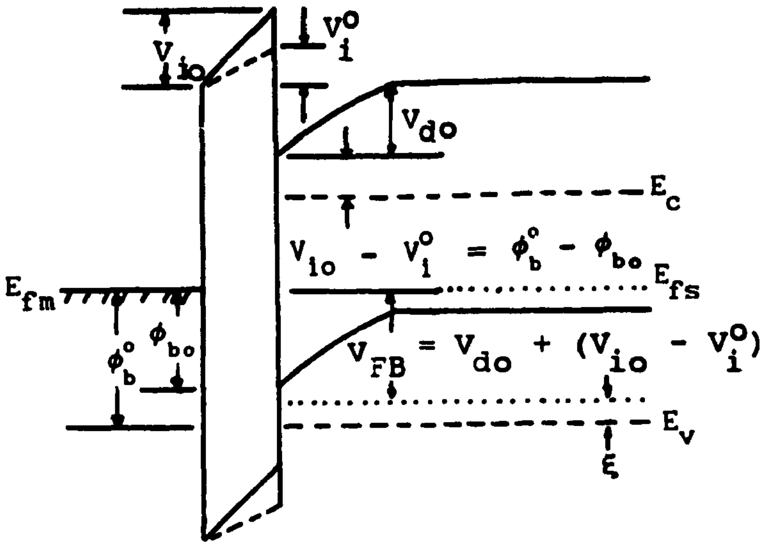

fig.5.10 MIS band bendings at
——— 0-bias & ------flat band
(FB)

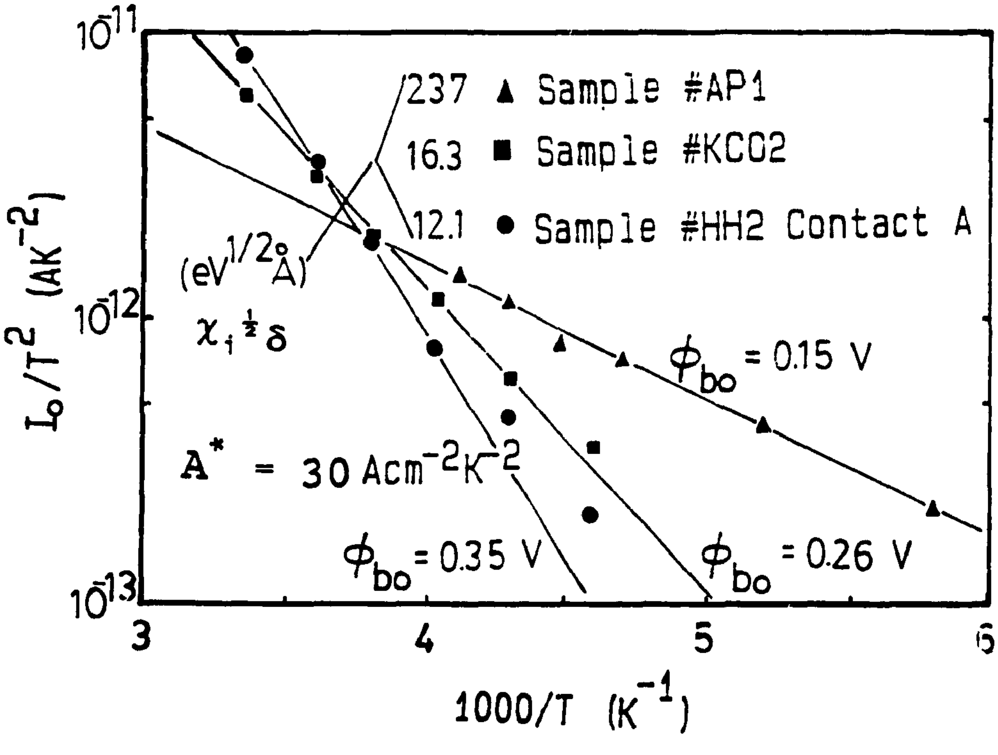

fig.5.11 LogI_o/T^2 vs. 1/T. 0-bias barrier height ϕ_{bo} from the slope and insulator transmission factor $\chi_i^{\frac{1}{2}}\delta$ from the I_o/T^2-intercept ($A^* = 30\ Acm^{-2}K^{-2}$).

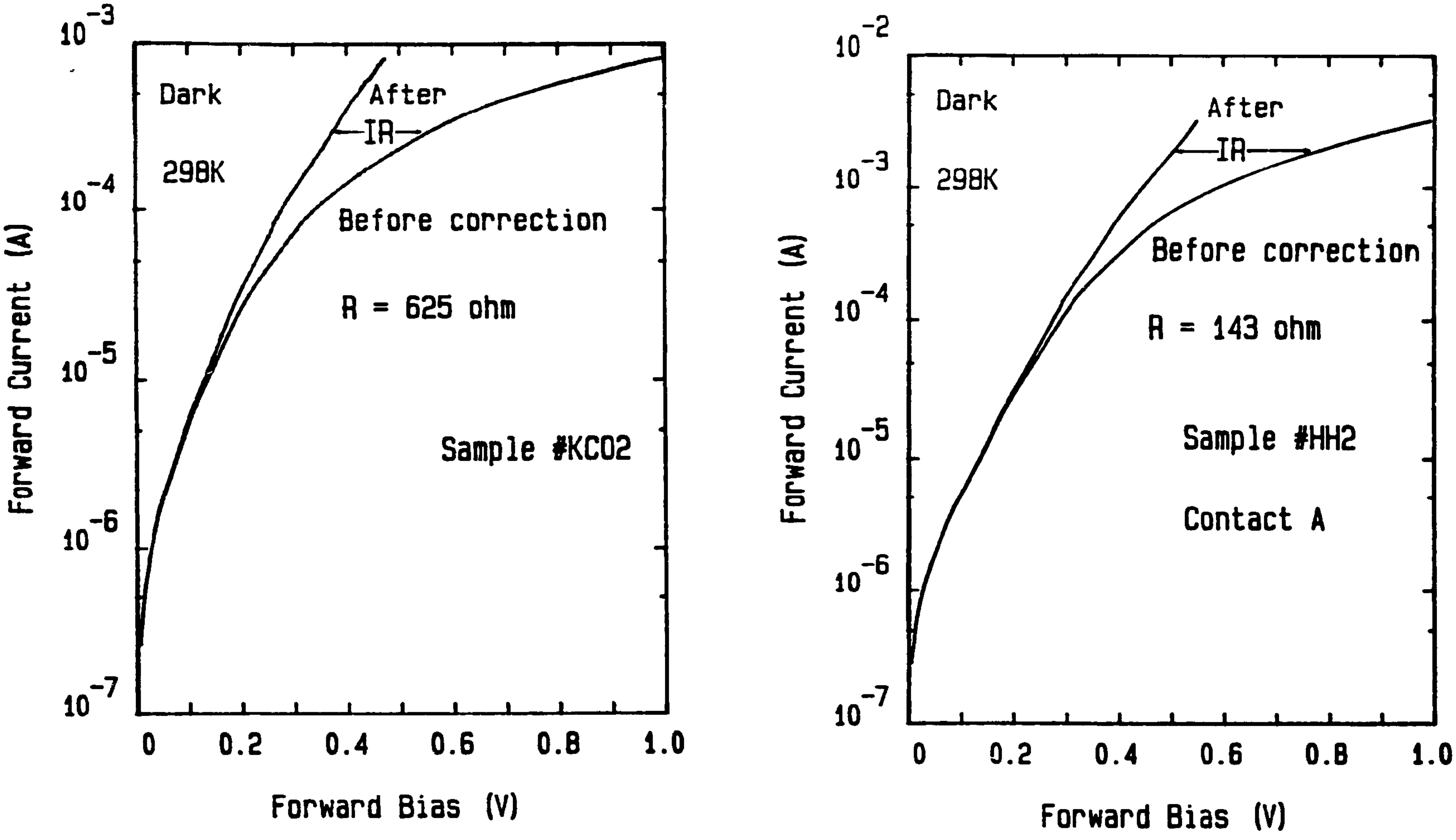

(a)

(b)

fig.5.12 Forward logI/V plots before and after R correction for diodes (a) KC02 (b) HH2, contact A

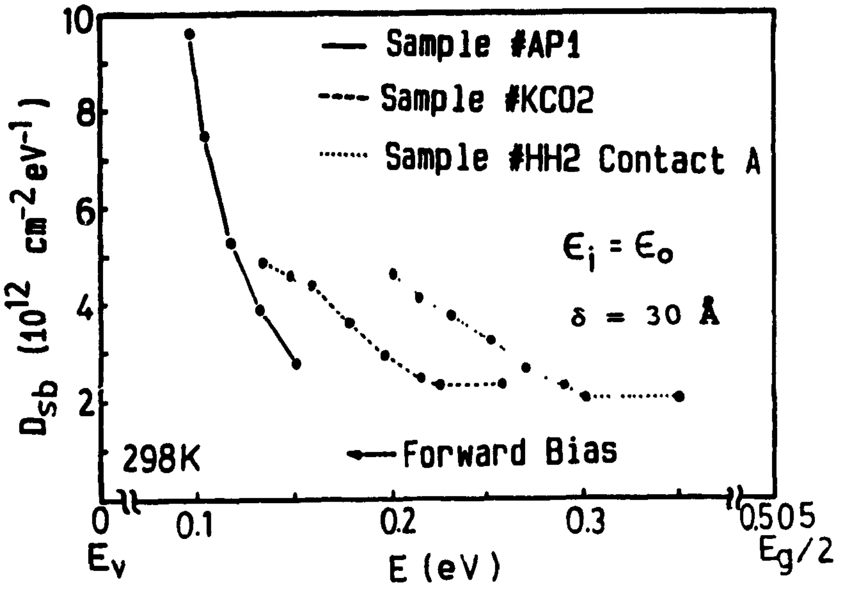

fig.5.13 Surface state (in equilibrium with p-$CuInSe_2$) energy profiles in the lower half gap from the R-corrected forward logI/V plots. Assume $\epsilon_i = \epsilon_o$ and δ = 30Å.

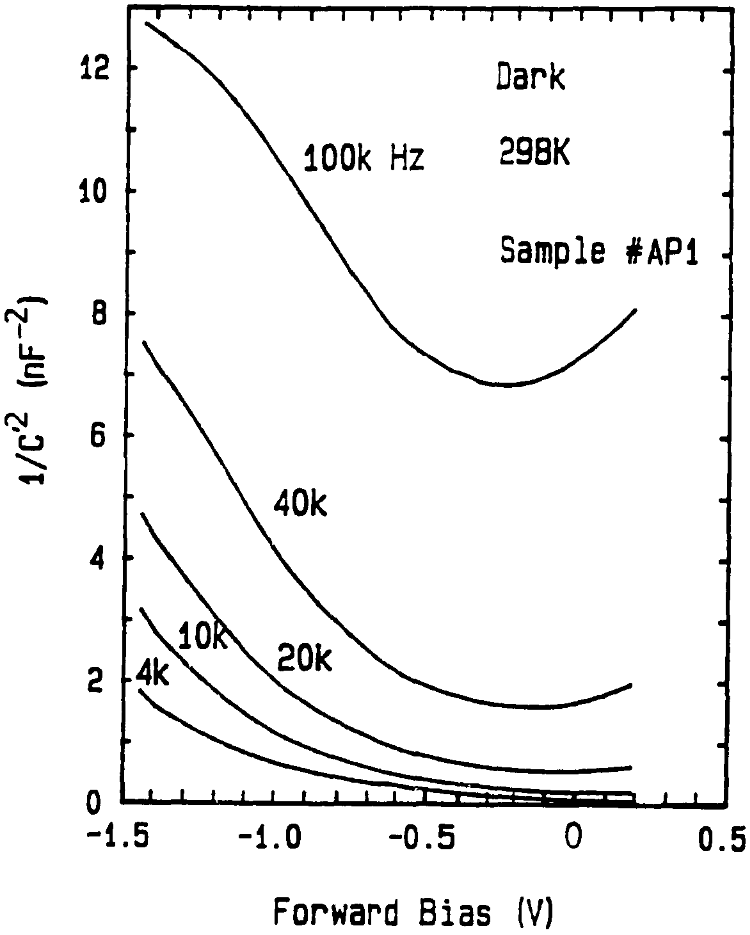

fig.5.14 C'^{-2}/V plots for diode AP1

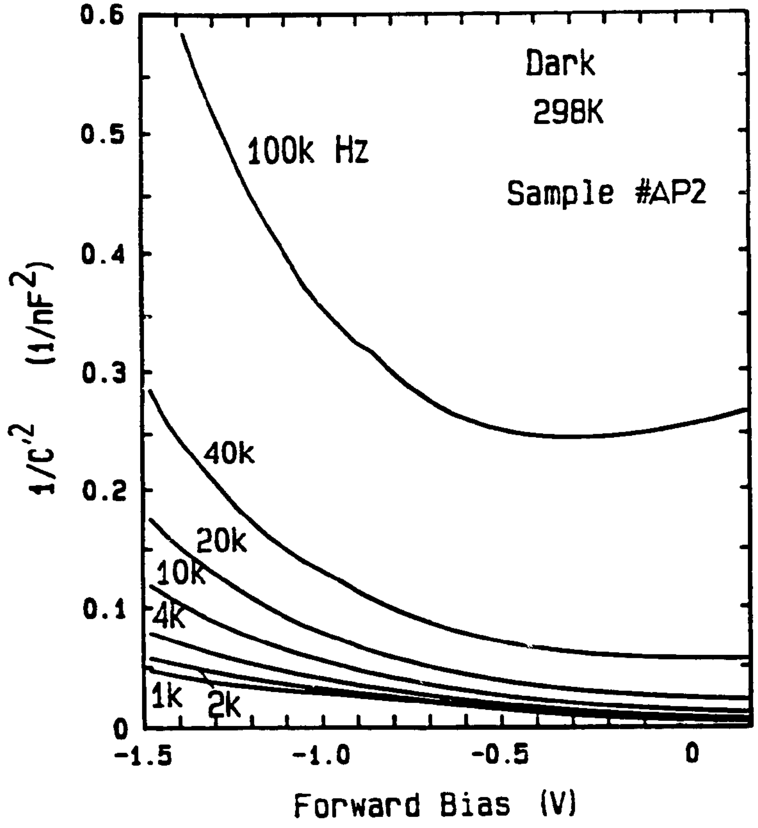

fig.5.15 C'^{-2}/V plots for diode AP2

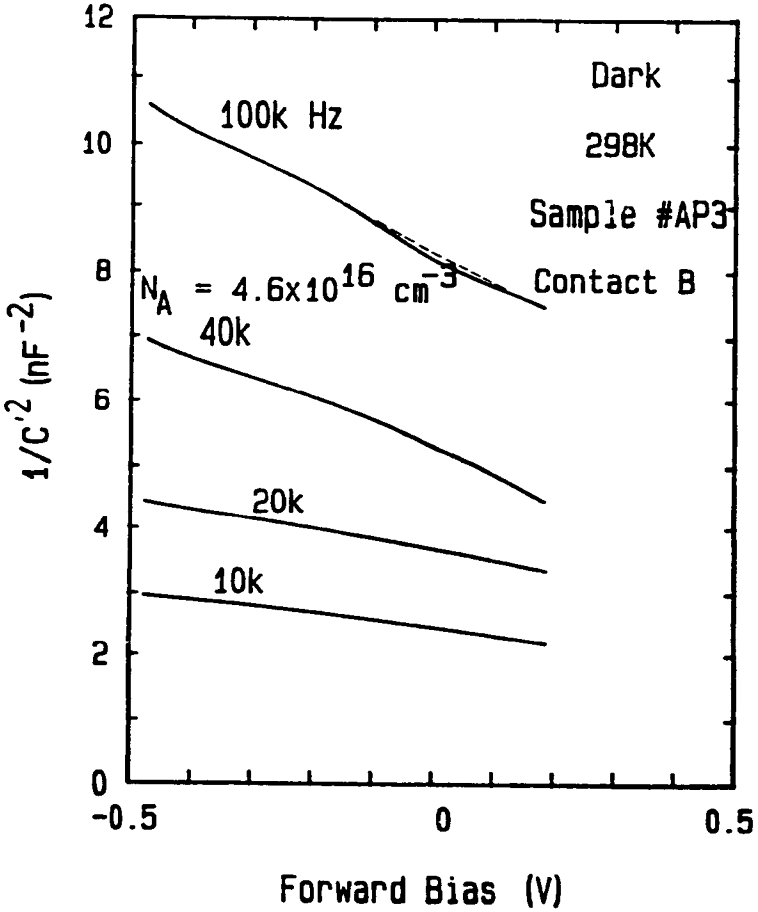

(a)

fig.5.16 **Continued next page**

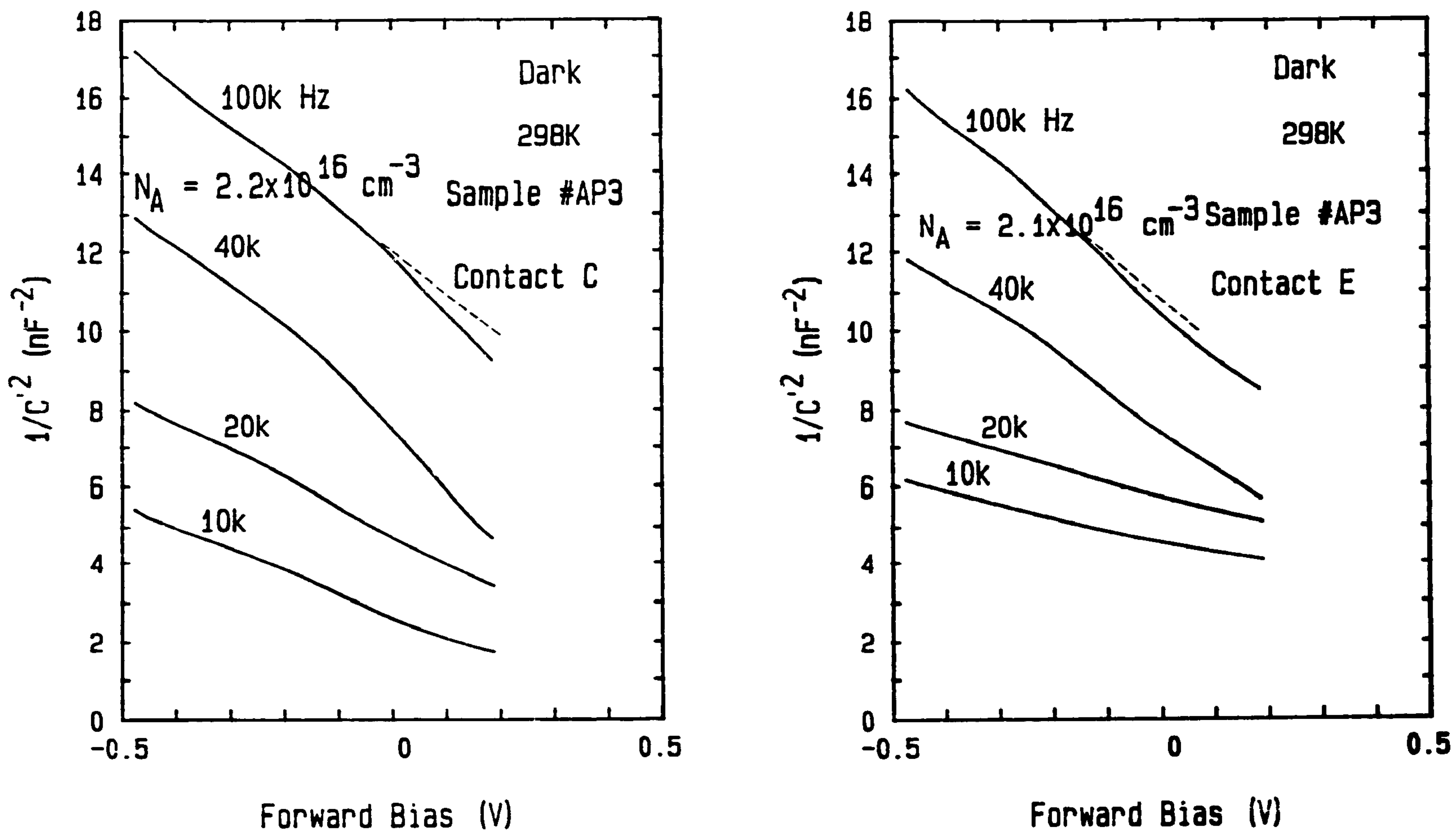

(b)

(c)

fig.5.16 C'^{-2}/V plots for diode AP3 (a) contact B (b) C (c) E

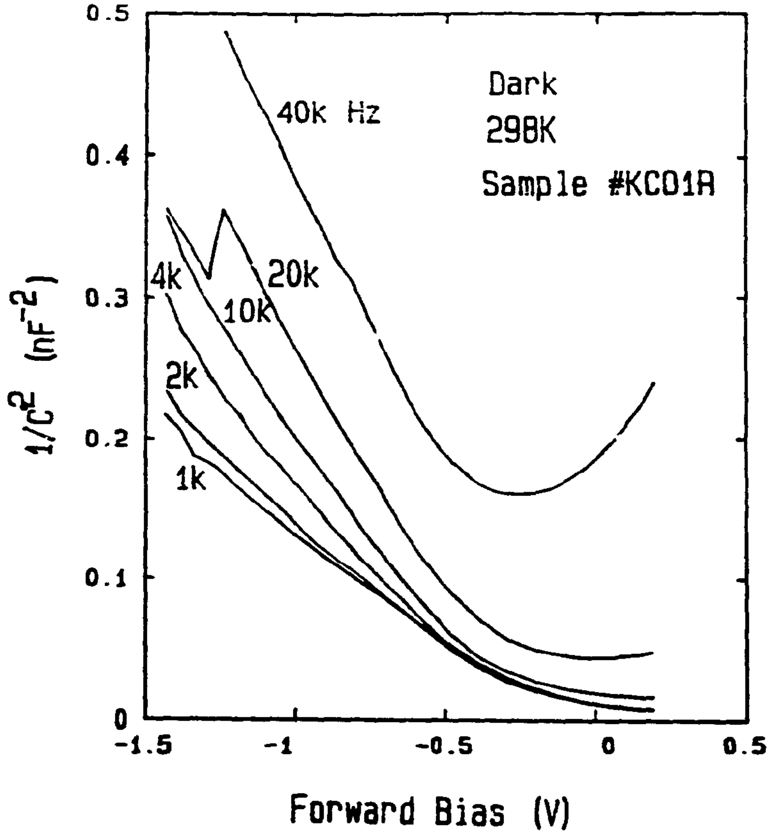

fig.5.17 C'^{-2}/V plots for diode KC01R

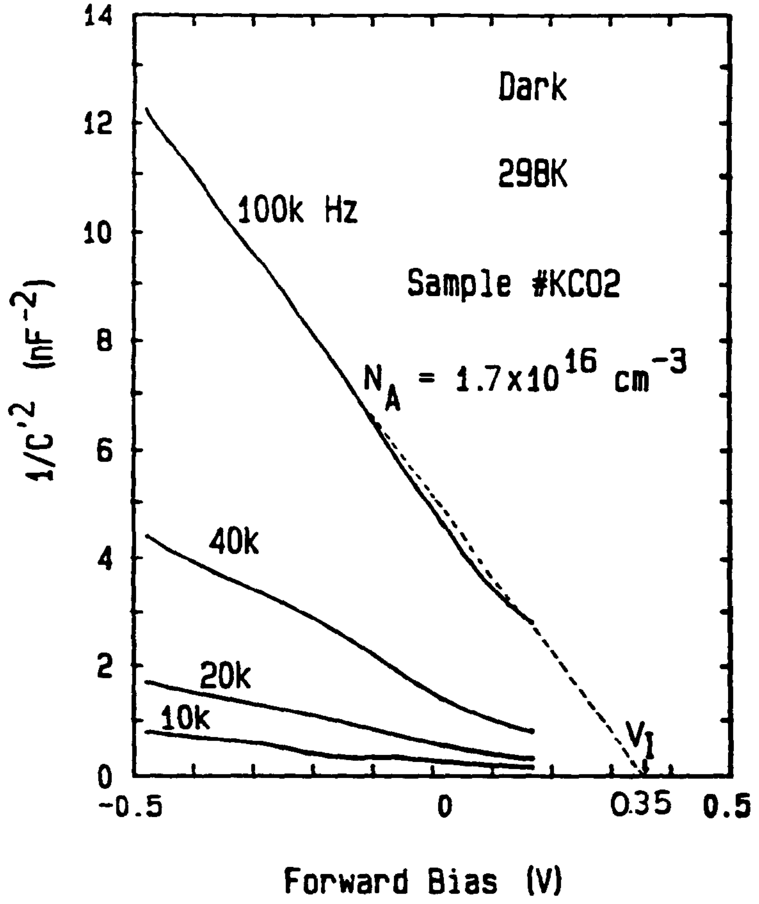

fig.5.18 C'^{-2}/V plots for diode KC02

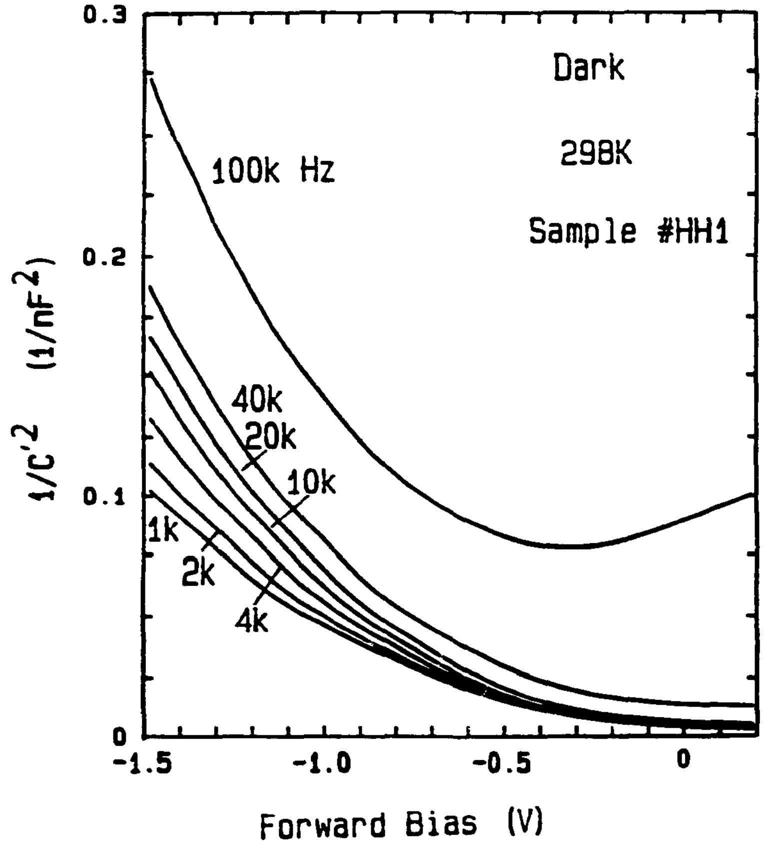

fig.5.19 C'^{-2}/V plots for diode HH1

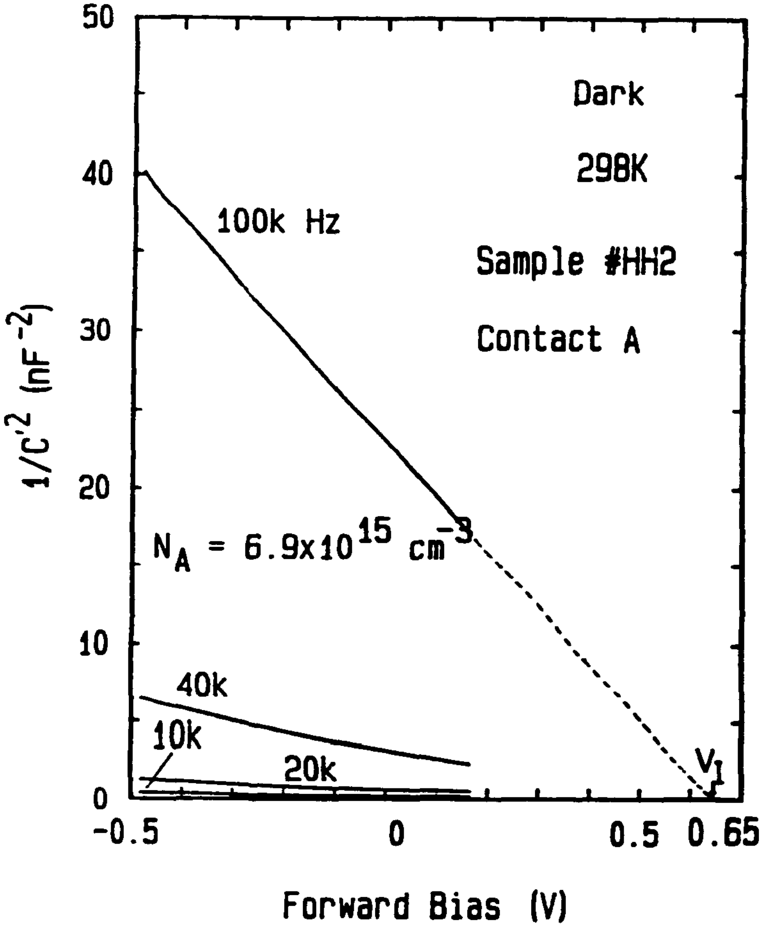

(a)

fig.5.20 Continued next page

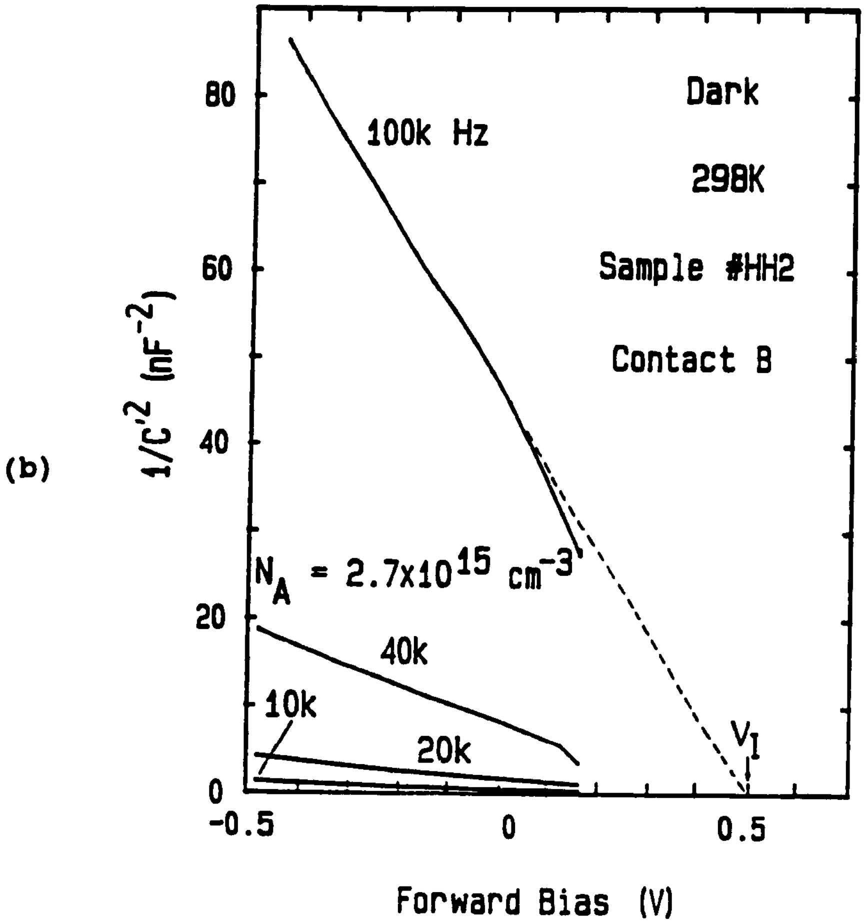

fig.5.20 C'^{-2}/V plots for diode HH2 (a) contact A (b) B

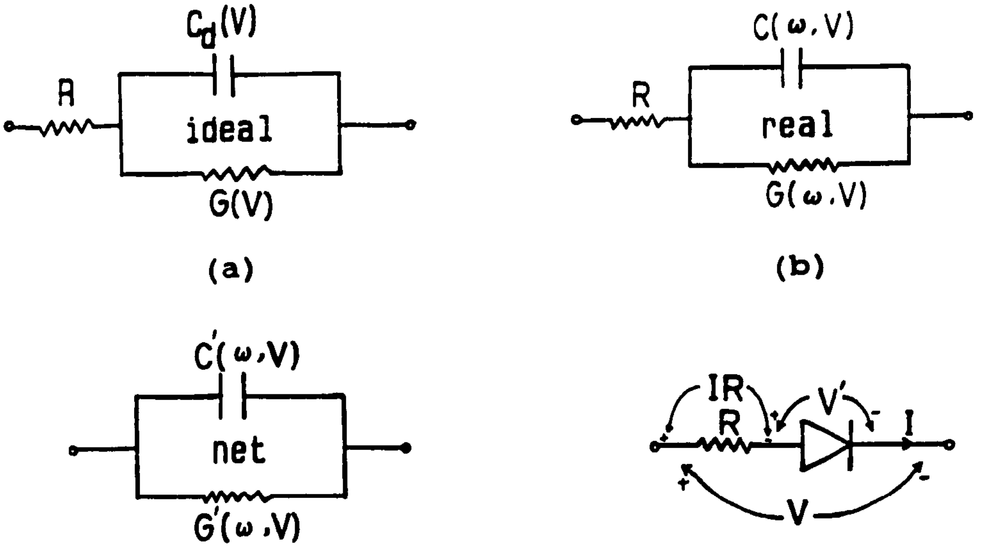

(a) (b)

(c) (d)

fig.5.21 (a) a.c. circuit of an ideal Schottky barrier with series R (b) a general case where C and G due to the junction are f-dependent (c) equivalent a.c. circuit seen by LCR bridge (d) d.c. circuit

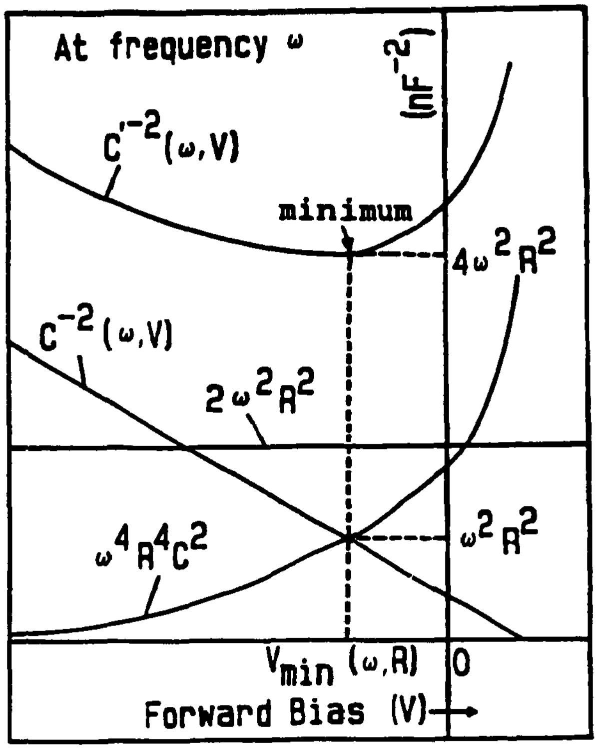

fig.5.22 Graphical formation of C'^{-2}_{min} due to R

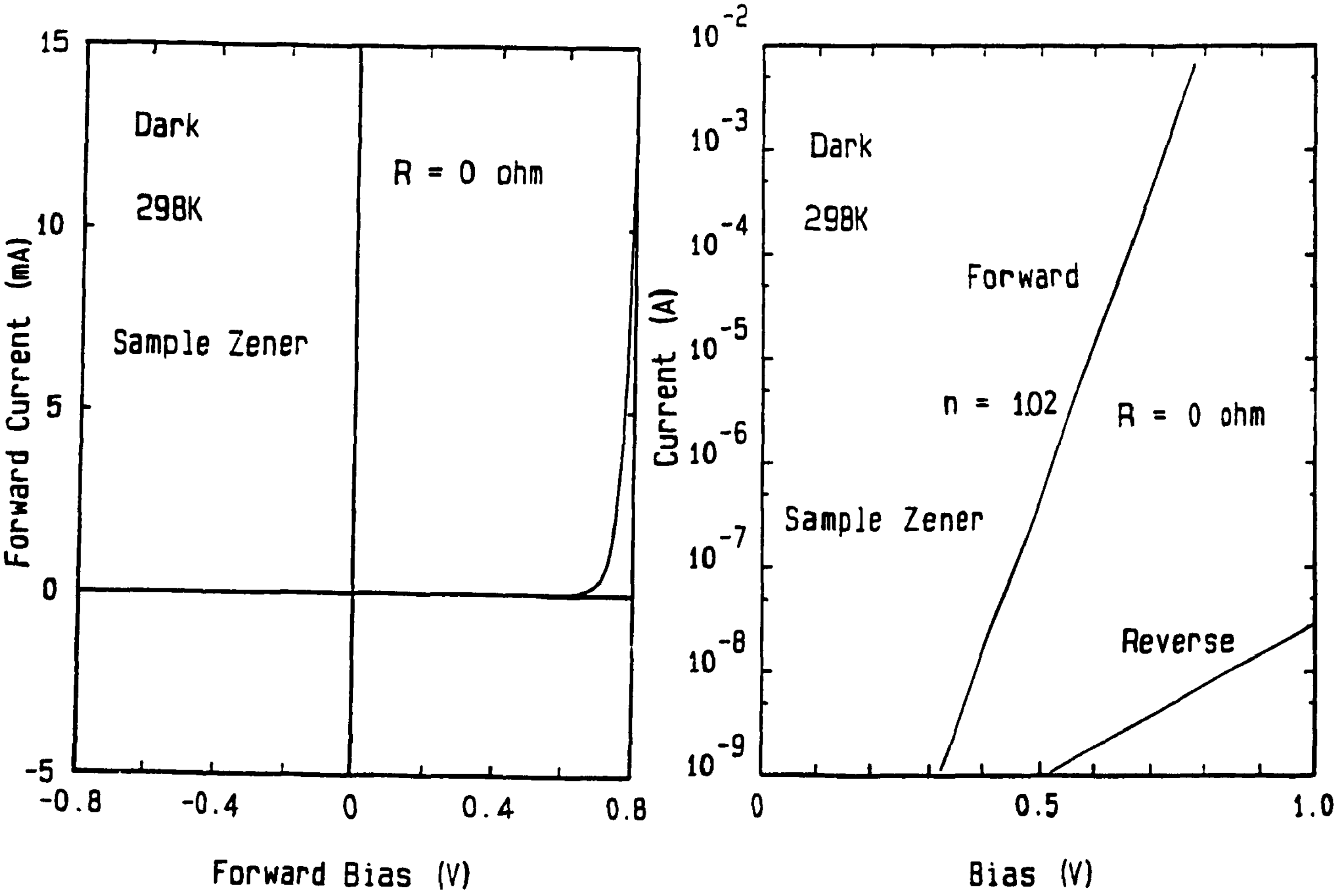

(a)

(b)

fig.5.23 I/V characteristics of a Motorola 1N74 Zener diode (a) linear I/V plot (b) logI/V plot

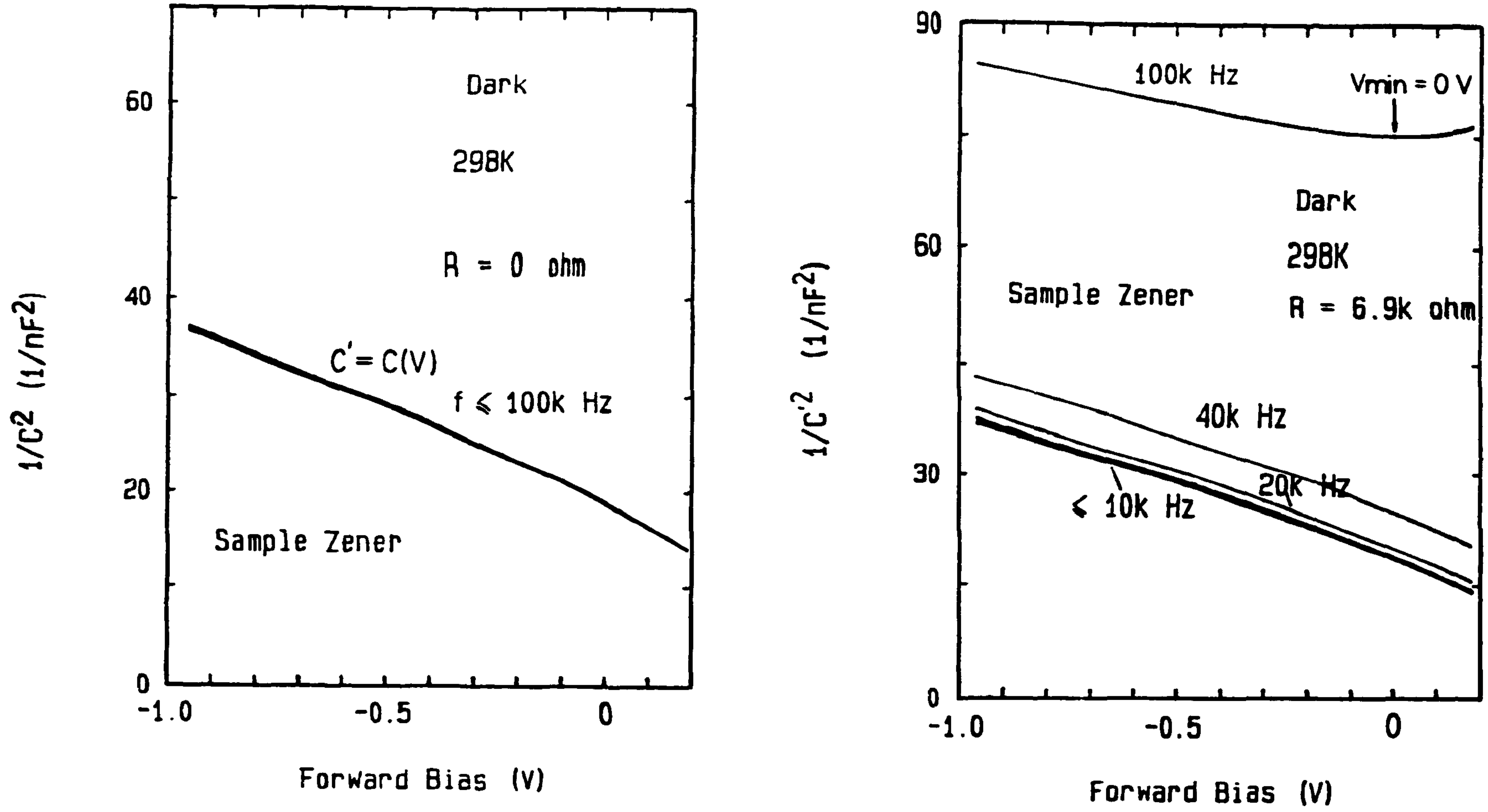

(a)

(b)

fig.5.24 Continued next page

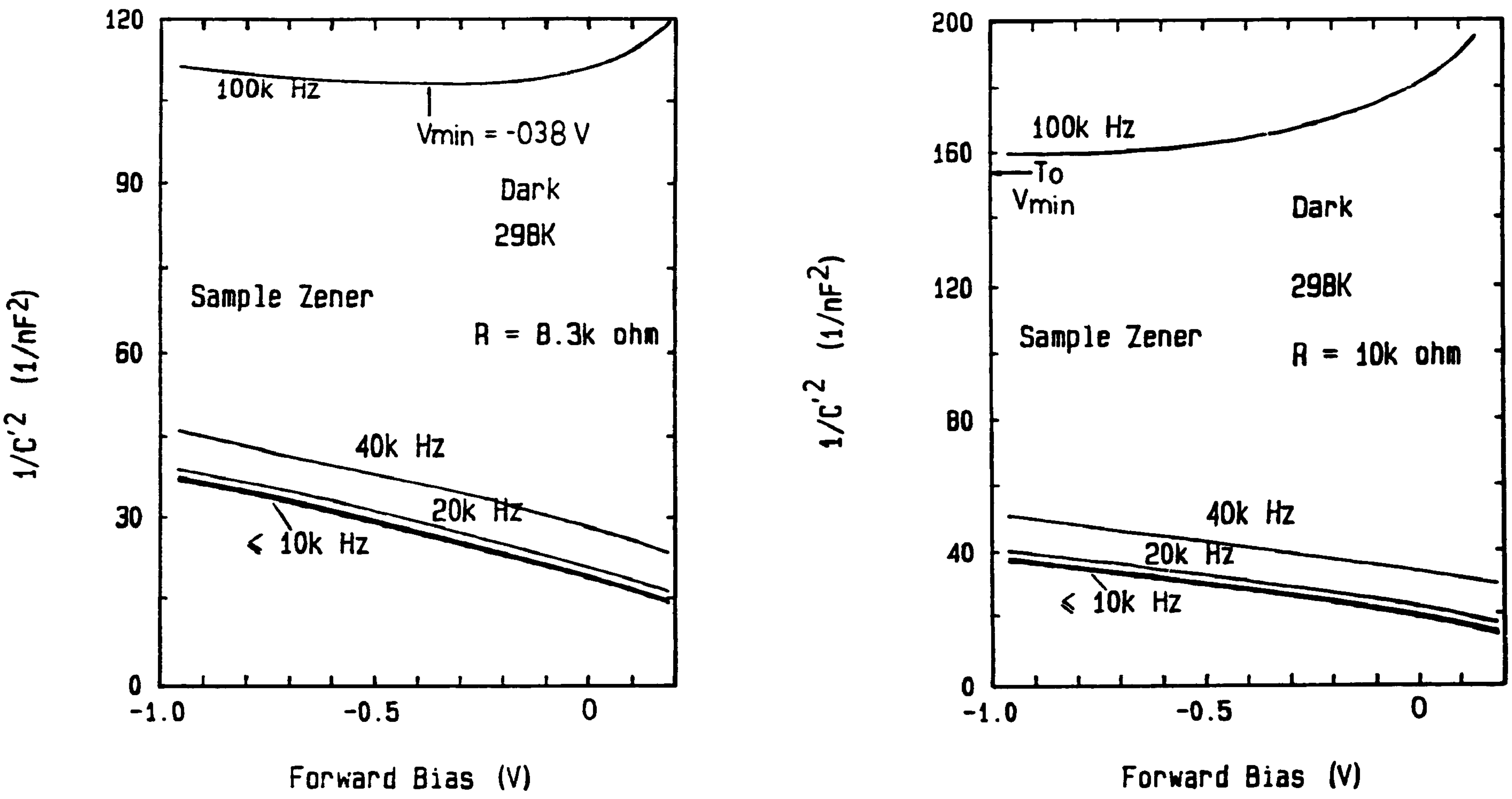

(c)

(d)

fig.5.24 Continued next page

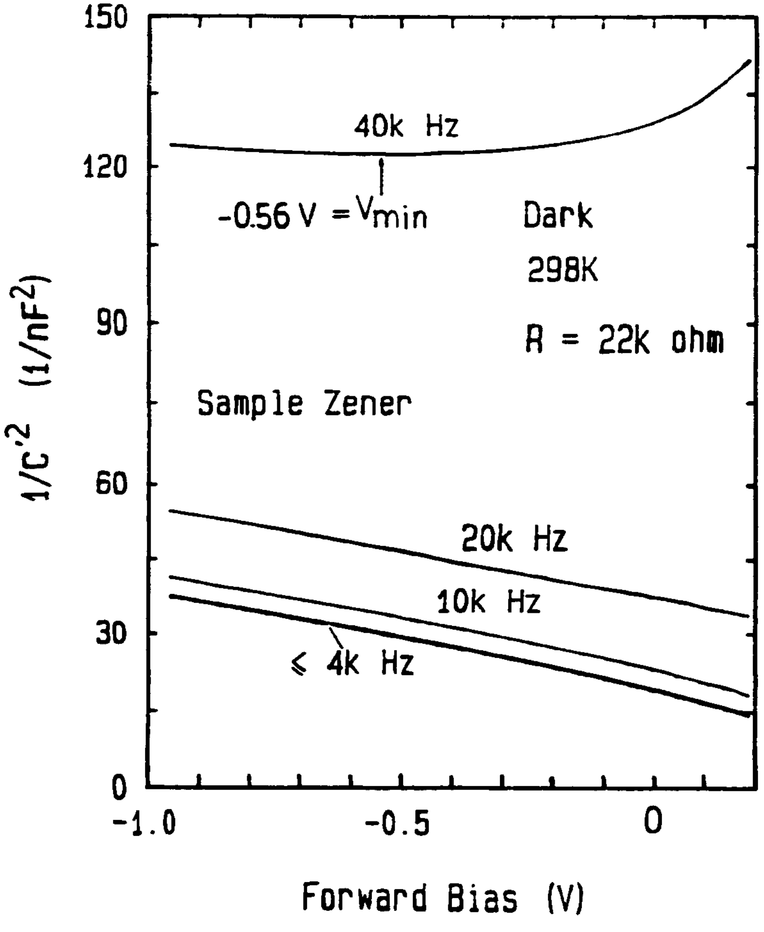

(e)

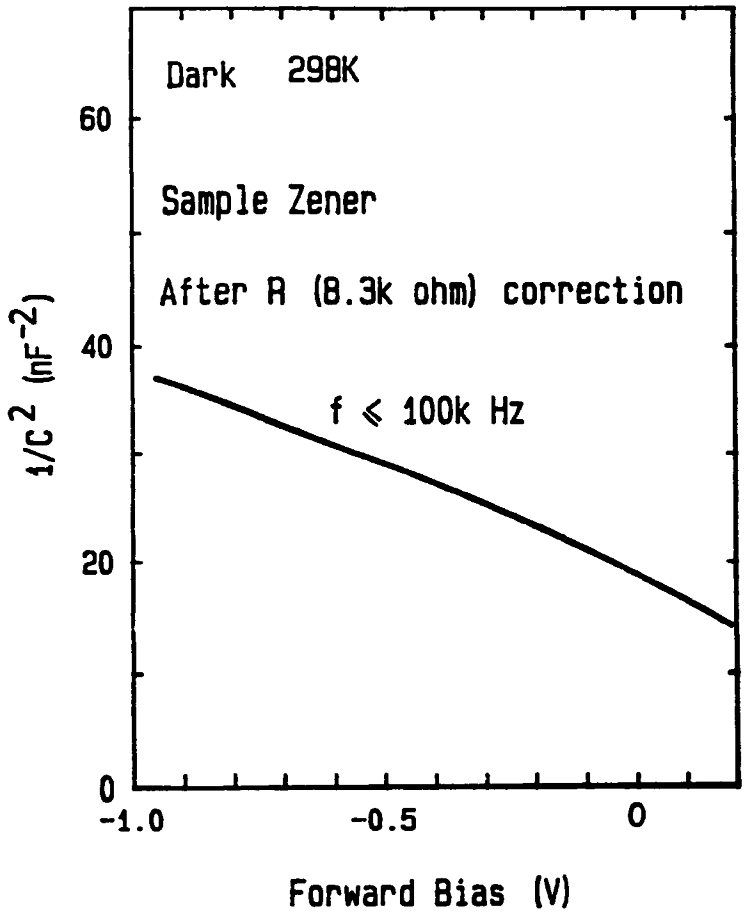

fig.5.24 C'^{-2}/V plots for 1N74 Zener diode with R = (a) 0 (b) 6.9 (c) 8.3 (d) 10 (e) 22 kohm

fig.5.25 C^{-2}/V plots for 1N74 Zener diode corrected from fig.5.24(c) with R = 8.3 kohm by (5.29) of our extended Goodman's model

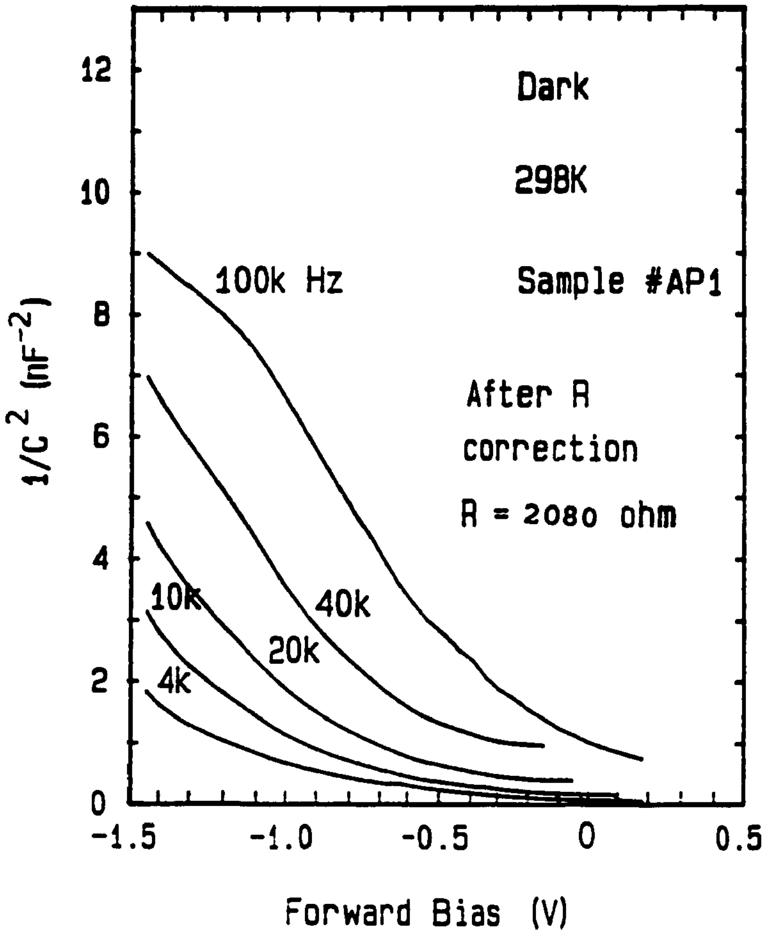

fig.5.26 C^{-2}/V plots for diode AP1 corrected from fig.5.14 with R = 2080 ohm by (5.29). The correction is not very good for V > V_{min}(100 kHz) since the series effect is not purely resistive.

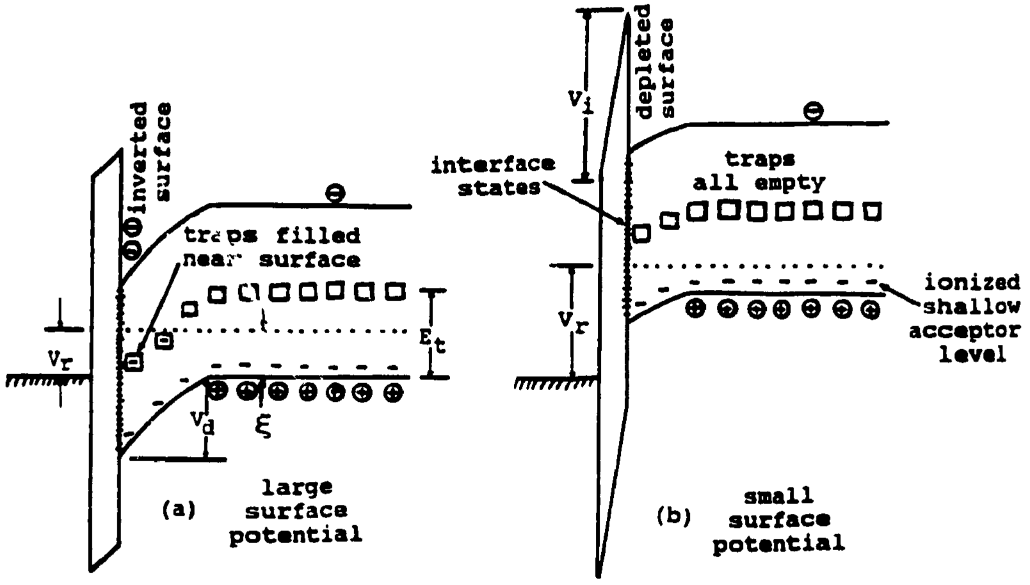

fig.5.27 MIS barriers with surface states and a simple deep level (a) thin δ, $V_d + \xi > E_t$ (b) thick δ, $V_d + \xi < E_t$

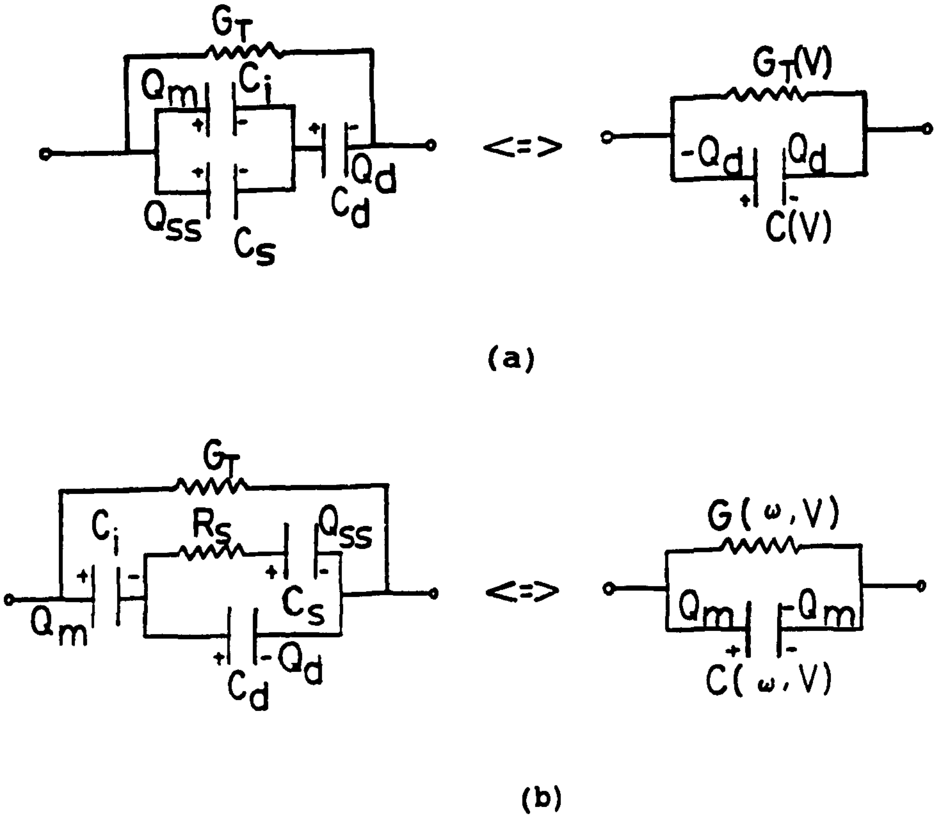

fig.5.28 a.c. circuit models for MIS barriers (a) thin δ (b) thick δ

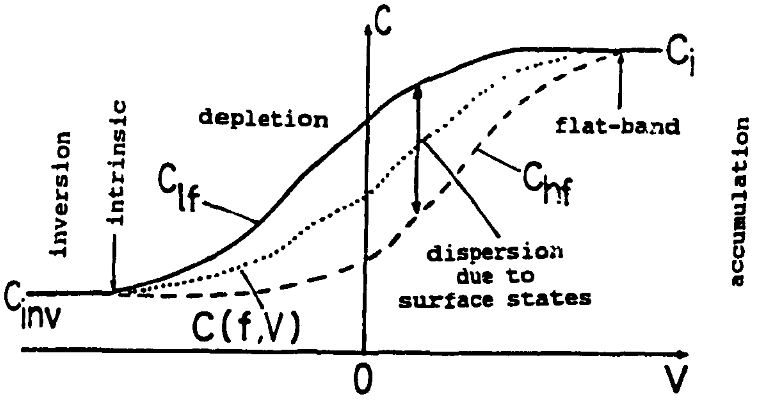

fig.5.29 Typical MIS C/V curves for thick δ where all surface states equilibrate with the semiconductor

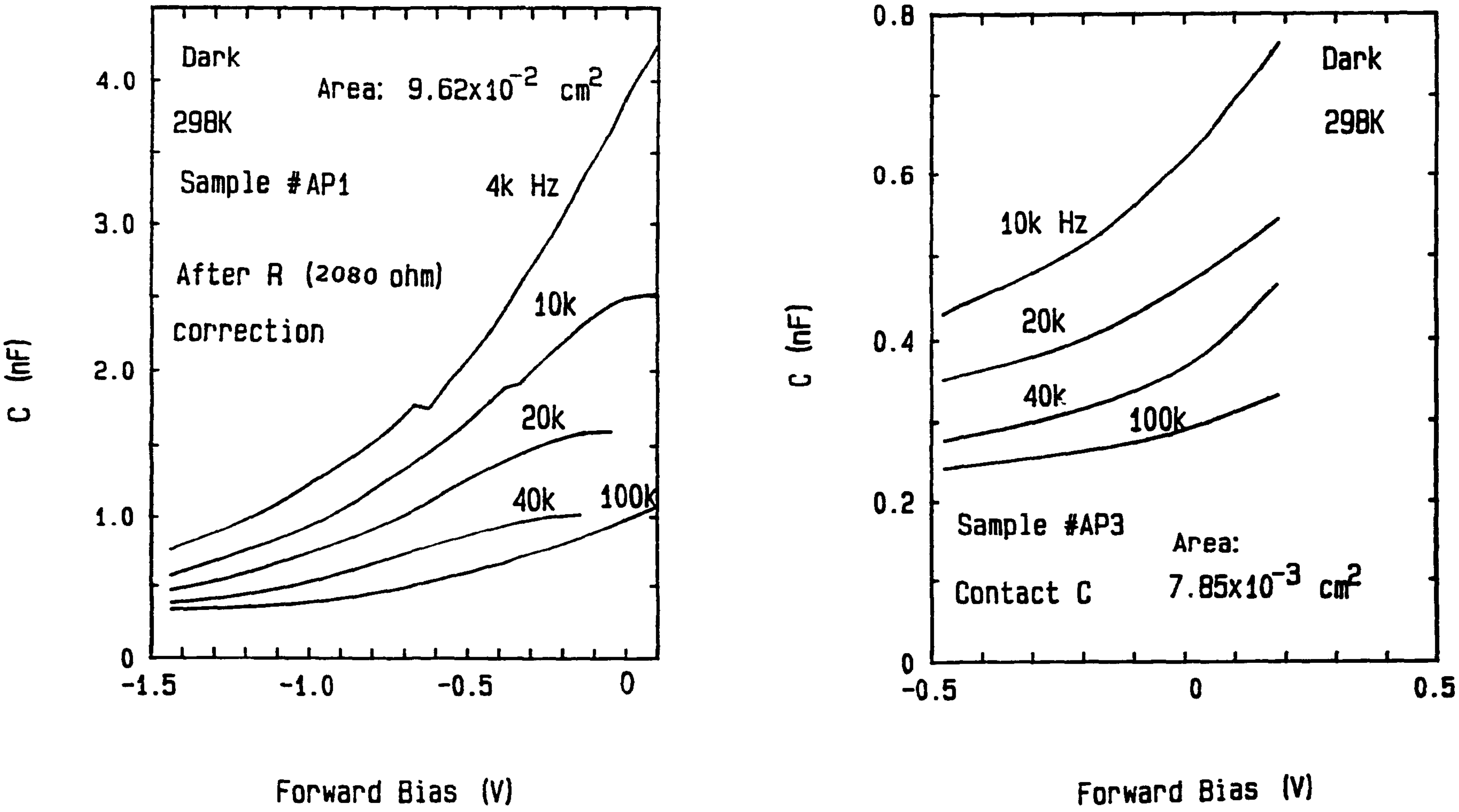

(a)

(b)

fig.5.30 Continued next page

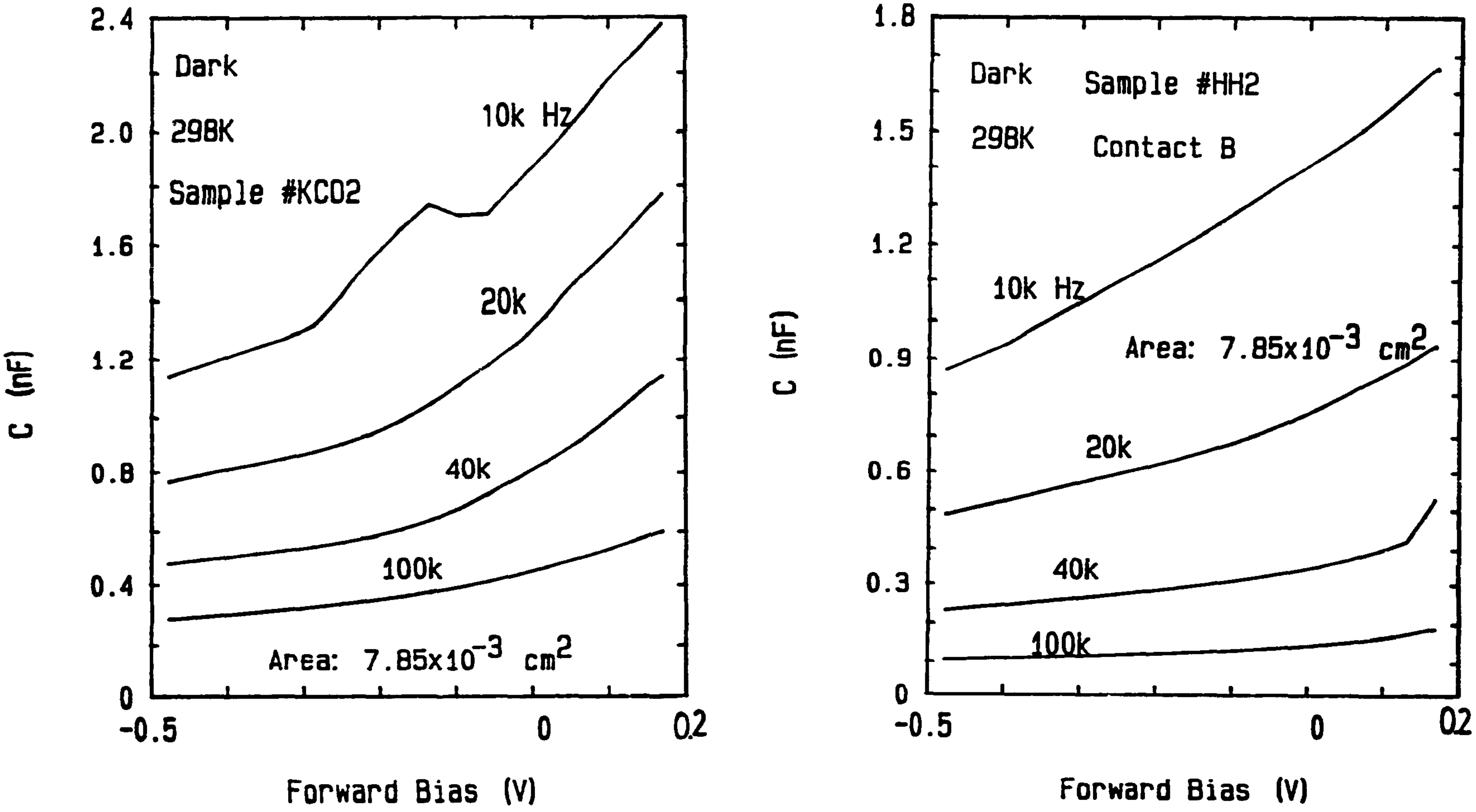

(c)

(d)

fig.5.30 C/V curves for diodes (a) AP1 after R correction
(b) AP3, contact C (c) KCO2 (d) HH2, contact B

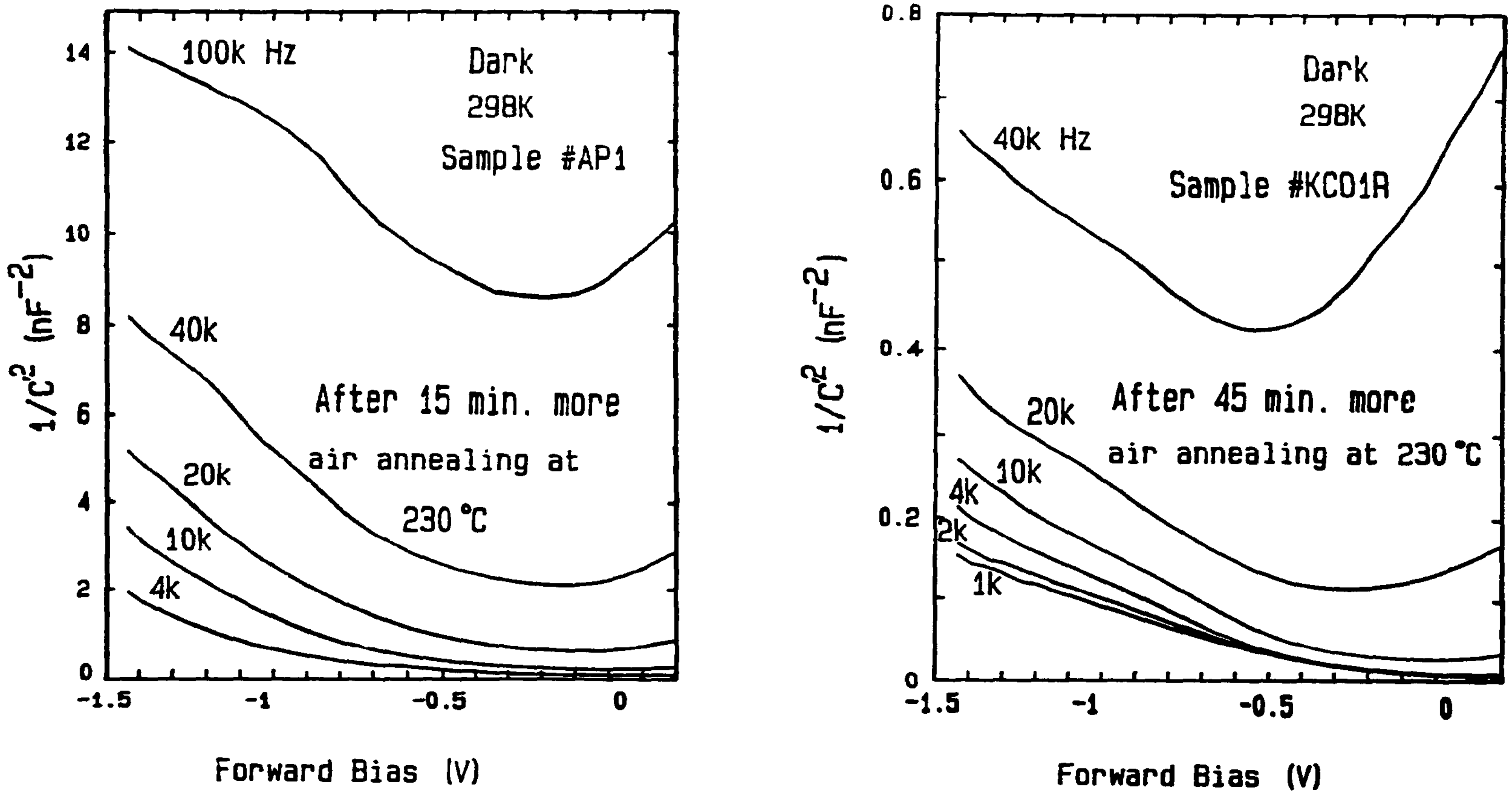

(a)

(b)

fig.5.31 C'$^{-2}$/V plots for diodes (a) AP1 after an extra annealing at 230 °C in air for 15 min. (b) KC01R after an extra annealing at 230 °C in air for 45 min.

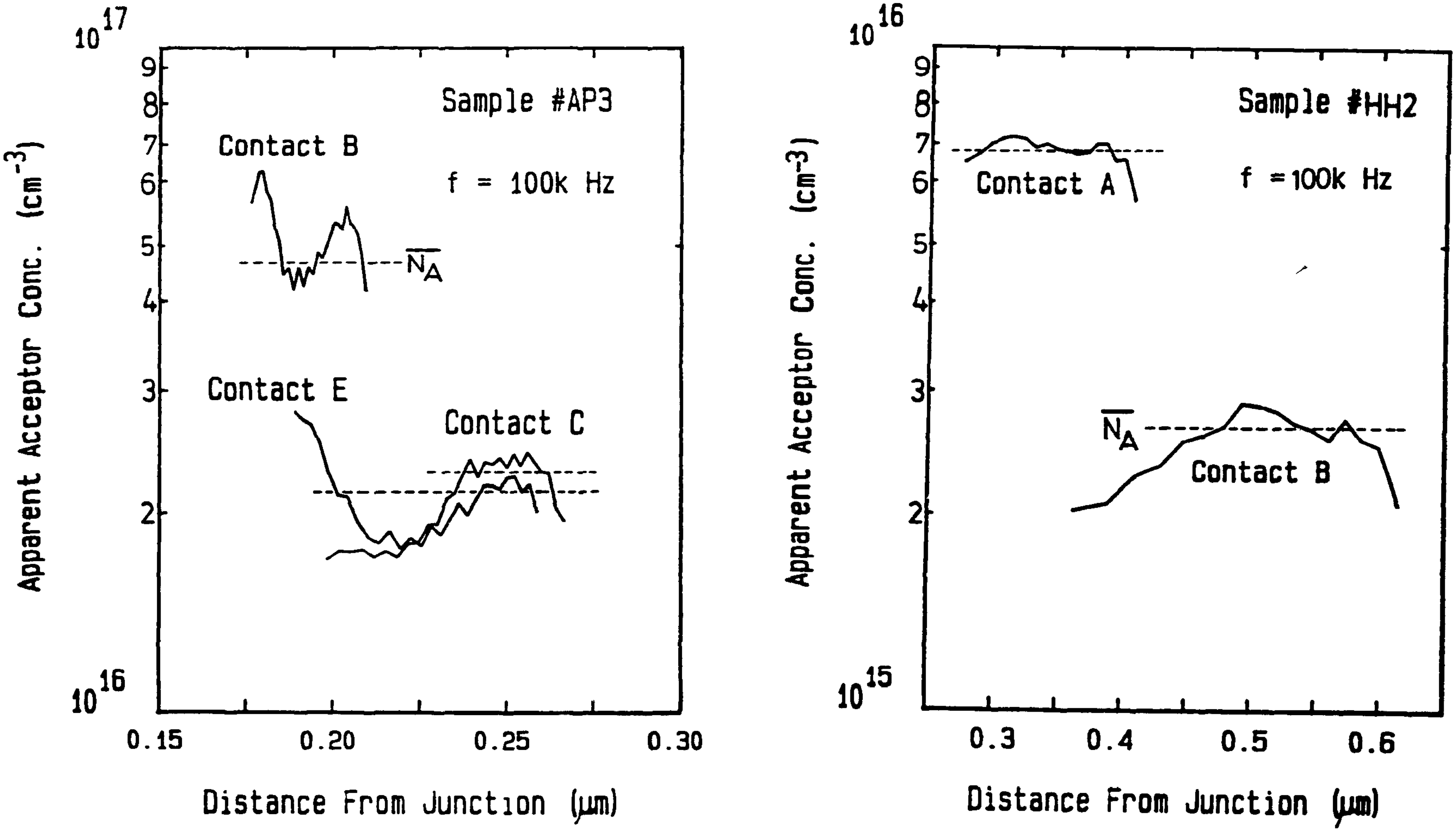

(a) (b)

fig.5.32 Apparent dopant profiles from C^{-2}/V slopes at 100 kHz using (2.33) and the depletion approximation for diodes (a) AP3 (b) HH2. Dotted lines represent the mean doping levels determined from the linear fits.

Chapter 6

Conclusions

Vacuum-deposited Al/p-$CuInSe_2$ (crystalline) Schottky junctions have been studied in order to examine some surface and bulk properties of our p-$CuInSe_2$ crystals prepared by the Bridgman process. Three surface preparation methods were used: 1) abrasive polishing (AP), 2) AP + etching in $K_2Cr_2O_7/H_2SO_4$ and 3) AP + etching in HCl/HNO_3. The dark d.c. currents (218 to 298°K) and steady-state differential capacitances (298°K, 1 kHz to 100 kHz) were measured as functions of bias. The results for the present devices are far more complicated for the classical transport and capacitance models in Chapter 2 to account for. Our devices were finally treated as the MIS tunnel diodes with strong surface state effects based on the following considerations. The formation of the interfacial insulating layers between the p-$CuInSe_2$ and Al is unintentional.

For all surface methods, the n values for the Al/p-$CuInSe_2$ diodes are greater than 2 at 298°K. So we rejected the common method involving log(I)/V intercept for barrier height determination. Recombination in the depletion layer as a dominant flow mechanism is not likely. Initially field emission was suspected due to the temperature-dependence of n. But the E_{oo} values (> 53 meV) from the nT products are not consistent with the hole densities of the as-grown substrates and the estimated $m^* = 0.25m_o$, referring to eqn. (2.18), and it is usually a low temperature process. Since the mean free path of holes $l = \bar{c}\tau_c < W$ (1 micron maximum from the C/V plots) by at least 2 orders of magnitude at forward bias [2.2], where the mean hole thermal velocity $\bar{c} = (3kT/m^*)^{1/2}$, mean free time $\tau_c = \mu_p m^*/q$ and $\mu_p = 60\ cm^2\ V^{-1}\ sec^{-1}$, drift and diffusion effects in the depletion layer may be as important at 298K as the more common series emission counterpart. The abrasively-polished samples have the biggest n among all and some even do not have a linear region for small bias V > 3kT/q. Our results are very similar to those reported by Robinson & Wilson [1.4] and Prasad et al. [1.17, 1.18] as far as the magnitude of n is concerned. The minimum χ_s reported for p-$CuInSe_2$ is 3.68 eV [1.4]. So the minimum $\Phi_s = \chi_s + (E_g - \xi) = 4.578$ eV for our typical N_A of $4x10^{16}cm^{-3}$ by eqn. (2.36). This implies a minimum V_{do} of 0.408 V and a minimum ϕ_b of 0.52 V by eqns. (2.6) and (2.34) respectively, if interfacial layer is absent. But the Richardson plots apparently gave small ϕ_b up to 0.35 V only. Combining with the fact that our n values are large, interface effects on thermionic emission, as first proposed by Card and Rhoderick, likely prevails. The maximum insulator transparent factor $\chi_1^{1/2}\delta$ is 23.7 $eV^{1/2}$Å for a polished sample. If χ_s is independent of the surface method, then its minimum value for our material is 3.51 eV because the unknown V_{1o} has not been added. Portions of surface state distributions $D_{sb}(E)$ were obtained from n(V) for V > 3kT/q after R correction, assuming $\varepsilon_1 = \varepsilon_o$, $\delta = 30$Å and all surface states in equilibrium with the p-$CuInSe_2$. The densities of the order of $10^{12}cm^{-2}eV^{-1}$, are larger near E_v than at higher E. The polished samples, with larger n values, accordingly have more surface damages per unit area than the etched ones do. Perhaps the profiles can be smoothened out with smaller integration steps ΔV, but the shape would definitely maintain. The R values estimated from the log(I)/V or linear I/V plots are often larger than what should be expected from the as-grown resistivities. In general, n, R and I_o for the various Al contacts on the same substrates differ, suggesting that the D_{st}, bulk N_A and band structure are transverse dependent. The effect is more pronounced for the polished samples.

All measured C'^{-2}/V characteristics are frequency- and bias-dependent. The truth for this will never be out of the set {deep trap effect, interface effects, series parasitic admittance} for any practical interface device. Even if the former two occur simultaneously, C(f,V) of the junction should be a monotonic increasing function over moderate bias ranges since they are additive to $C_d(V)$. The existence of minima is believed to be caused by the series admittance effect of the ohmic contacts, specifically the bottom one involving the bulk p-$CuInSe_2$. We began with the case of a simple R and Goodman's model has been expanded here to obtain the minimal conditions eqns. (5.26) and (5.27) at high frequency and for large R. A correction scheme (eqn. (5.29)) was also developed. The new model worked successfully for the test example Si Zener diode and some of our devices where the series admittance was equivalently resistive over the frequency and bias ranges. For those samples where it failed, we focused on the better approximated regions $V \ll V_{min}$(100 kHz). After correction, the C^{-2}/V curves were still frequency-dependent. Because 1) V_{do} are small and n are large from the I/V results and 2) within

E_g, surface states distribute in continuum while deep levels are discrete, interface effects are probably more important to C than deep traps for our small $V_r(V_d)$ values. This assumption is essential for any further quantitative analysis. At this point, we could only blame interfacial layer and surface states which equilibrate with the p-$CuInSe_2$ for the frequency-dependence, in agreement with the I/V conclusion. All of our p-$CuInSe_2$ surfaces were depleted in view of the slow rises of the C(100 kHz) with V. The V-intercepts of those linear C^{-2}/V plots are significantly larger than the ϕ_{bo} from the temperature-dependent I/V method. Using Cowley's model for thick δ, D_{sb} values of the order of $10^{12}cm^{-2}eV^{-1}$ were obtained, assuming $\varepsilon_i = \varepsilon_o$ and δ = 30 Å. For other non-linear graphs, most surface states have a life-time shorter than 1.6 µsec or $D_{sb}(E)$ are non-uniform over the V_r ranges. The extended Goodman's model has not only allowed us to extract the actual MIS junction capacitance, but also allowed us to reach the following conclusions: 1) the origin of R is from the p-$CuInSe_2$ bulk and 2) Se out-diffusion occurs under air annealing even at 230°C. The apparent acceptor profiles for the different Al contacts on the same substrates, obtained by depletion approximation, are less uniform on the transverse planes than along the growth axes.

In this study, a lot of uncertainties have been encountered and so many assumptions had to be made in order to apply the available theory for analysis. For instance, the actual transport mechanism may be an unknown mixture of series and parallel components when n is far from 1. If so, any curve fitting scheme can merely give an average picture of the unique physical system, i.e., 2 or more different sets of mechanisms with optimal parameters may fit equally well into the discrete I/V data since all these methods care about is the deviation in I or V at the end. A better understanding of the subject invokes the preparation of near-ideal material and devices as controlled samples for further issues of complications and comparisons. In this regard, more fundamental efforts should be done to 1) grow material with minimum deep impurity and defect count: this can isolate the effects of traps and surface states which always exist at the free surfaces 2) analyze the chemical compositions and morphologies of the surfaces using the three previous methods 3) passivate our junctions with guard rings so as to simplify the net currents 4) examine the capacitive effect of the epoxy junction (fig.6.1): if its admittance is not significantly large compared to the MIS's over the bias and frequency ranges of interest, the measured one (underestimate) needs correction 5) measure C at higher and lower frequency to see the complete ranges of surface state effects with a better LCR meter 6) anneal our present material in air and make Hall effect measurement after to double-check Se out-diffusion.

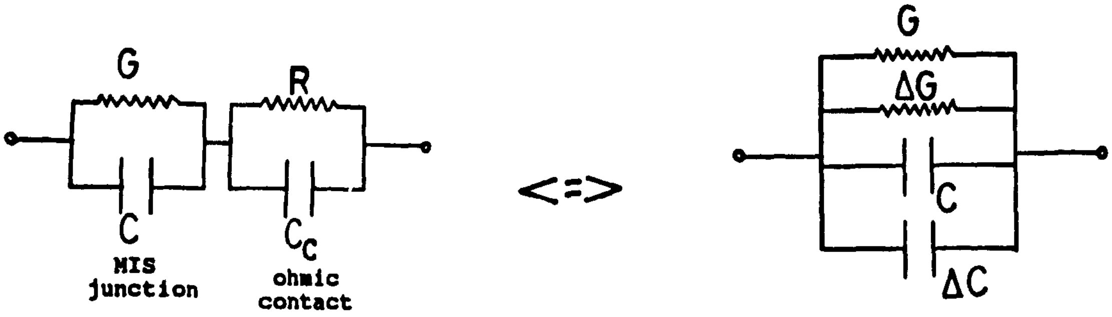

fig.6.1 (a) Net diode admittance is a series combination of the Al/insulator/p-$CuInSe_2$ (depletion region) junction admittance and the admittance due to the p-$CuInSe_2$ (quasi-neutral region)/epoxy/Al base bottom ohmic contact (see fig.3.4). C, G and C_c are generally V- and f-dependent. (b) equivalent circuit as seen by LCR bridge. ΔG and ΔC are the unintentional errors (-) due to the ohmic contact. All 4 elements are V- and f-dependent.

References

[1.1] J.L. Shay, S. Wagner and H.M. Kasper, Appl. Phys. Lett., 27, 89 (1975).

[1.2] K. Mitchell, 4th International Photovoltaic Sci. and Eng. Conf., 146 (1989).

[1.3] H. Hahn, G. Frank, W. Klinger, A.D. Meyer and G. Storger, Z. anorg. allg. Chem., 271, 153 (1953).

[1.4] P. Robinson and J.I.B. Wilson, Inst. Phys. Conf. Ser., 35, 229 (1977).

[1.5] T. Irie, S. Endo and S. Kimura, Japan. J. Appl. Phys., 18, 1303 (1979).

[1.6] J. Parkes, R.D. Tomlinson and M.J. Hampshire, J. Cryst. Growth, 20, 315 (1973).

[1.7] R.A. Mickelsen and W.S. Chen, Proc. 15th Photovoltaic Spec. Conf., 800 (1981).

[1.8] J. Parkes, R.D. Tomlinson and M.J. Hampshire, Solid-State Electron., 16, 773 (1973).

[1.9] H. Neumann, R.D. Tomlinson, E. Nowak and N. Avgerinos, Phys. Stat. Solidi(a), 56, K137 (1979).

[1.10] P.W. Li, R.A. Anderson and R.H. Plonick, J. Phys. Chem. Solids, 40, 333 (1979).

[1.11] H. Neumann and N.V. Nam, Solid-State Commun., 25, 899 (1978).

[1.12] I. Shih, A.V. Shahidi and C.H. Champness, J. Appl. Phys., 56(2), 421 (1984).

[1.13] I. Shih and C.X. Qiu, Electron. Lett., 21(8), 350 (1985).

[1.14] C.X. Qiu and I. Shih, Solar Cells, 16, 391 (1986).

[1.15] N. Yalcin, I.S. Al-Saffar and R.D. Tomlinson, J. Appl. Phys., 52(9), 5857 (1981).

[1.16] F. Leccabue, D. Seuret and O. Vigil, Appl. Phys. Lett., 46(9), 853 (1985).

[1.17] J.J.B. Prasad, D.K. Rao, D. Sridevi, J. Majhi, K.V. Reddy and J. Sobhanadri, Solid-State Electron., 28(12), 1251 (1985).

[1.18] D.K. Rao, J.J.B. Prasad, D. Sridevi, K.V. Reddy and J. Sobhanadri, Phys. Stat. Solidi(a), 94, K153 (1986).

[1.19] A. Thanailakis and A. Rasul, J. Phys. C, Solid-State Phys., 9, 337 (1976).

[2.1] W. Schottky, Naturwissenschaften, 26, 843 (1938).

[2.2] E.H. Rhoderick, Metal-Semiconductor Contacts, Clarendon Press, Oxford (1978).

[2.3] J. Bardeen, Phys. Rev., 71, 717 (1947).

[2.4] A.M. Cowley and S.M. Sze, J. Appl. Phys., 36, 3212 (1965).

[2.5] H.K. Henisch, Rectifying Semiconductor Contacts, Oxford U. Press, Oxford (1957).

[2.6] H.A. Bethe, Theory of the Boundary Layer of Crystal Rectifiers, MIT Radiation Lab. Report, 12 (1942).

[2.7] C.R. Crowell and S.M. Sze, Solid-State Electron. 9, 1035 (1966).

[2.8] F.A. Padovani and R. Stratton, Solid-State Electron., 9, 695 (1966).

[2.9] C.T. Sah, R.N. Noyce and W. Shockley, Proc. IRE, 45, 1228 (1957).

[2.10] R.H. Fowler, Phys. Rev., 38, 45 (1931).

[2.11] S.M. Sze, Phys. of Semiconductor Devices, John Wiley & Sons, N.Y. (1969).

[3.1] I. Shih, A.V. Shahidi and C.H. Champness, J. Crystal Growth, 70, 411 (1984).

[3.2] I. Shih, C.H. Champness and A.V. Shahidi, Canadian J. Phys., 63(6), 811 (1985).

[3.3] A.V. Shahidi, M. Eng Thesis, Dept. of Elect. Eng., McGill U., Montreal, Canada (1984).

[5.1] H.C. Card and E.H. Rhoderick, J. Phys. D: Appl. Phys., 4, 1589 (1971a).

[5.2] L.G. Walker, Solid-State Electron., 17, 763 (1974).

[5.3] H.C. Card and E.H. Rhoderick, J. Phys. D: Appl. Phys., 4, 1602 (1971b).

[5.4] A.M. Goodman, J. Appl. Phys., 34, 329 (1963).

[5.5] A.M. Cowley, J. Appl. Phys., 37, 3024 (1966).